Simulation of Tin Plasmas & Theory of Laser Light Absorption

Stan Johannes Jacobus de Lange

Ph.D. thesis, Vrije Universiteit Amsterdam, 2026
Simulation of Tin Plasmas & Theory of Laser Light Absorption
Stan J. J. de Lange

Printing: Ridderprint
DOI: 10.5463/thesis.1878
ISBN: 978-94-6568-033-0

An electronic version of this dissertation is available at: research.vu.nl

VRIJE UNIVERSITEIT

Simulation of Tin Plasmas & Theory of Laser Light Absorption

ACADEMISCH PROEFSCHRIFT

ter verkrijging van de graad van Doctor of Philosophy
aan de Vrije Universiteit Amsterdam,
op gezag van de rector magnificus
prof.dr. J.J.G. Geurts,
volgens besluit van de decaan
van de Faculteit der Bètawetenschappen
in het openbaar te verdedigen
op maandag 23 november 2026 om 13.45 uur
in de universiteit

door

Stan Johannes Jacobus de Lange

geboren te Drechterland

promotor:	prof.dr. O.O. Versolato
copromotor:	dr. J. Sheil
promotiecommissie:	prof.dr. P. Duffy dr. K.I.E. Olsson prof.dr. H.G. Raven dr. H.J. Teunissen prof.dr. W.M.G. Ubachs



The work described in this thesis was conducted at the Advanced Research Center for Nanolithography (ARCNL), a public–private partnership between the Vrije Universiteit Amsterdam (VU), the University of Amsterdam (UvA), Rijksuniversiteit Groningen (RUG), the Dutch Research Council (NWO), and the semiconductor equipment manufacturer ASML.

Contents

1 Introduction **1**
- 1.1 Calculating the yield of an atomic bomb . . . 1
- 1.2 What is a plasma? . . . 2
  - 1.2.1 Plasma as an ionized gas . . . 3
  - 1.2.2 Coulomb collisions . . . 3
  - 1.2.3 Plasma as a fluid . . . 6
  - 1.2.4 Radiation in plasma . . . 8
  - 1.2.5 Other considerations . . . 10
  - 1.2.6 The Langdon effect . . . 10
- 1.3 EUV nanolithography . . . 11
- 1.4 Research questions and thesis outline . . . 14

2 Modeling the hundreds-of-nanoseconds-long irradiation of tin droplets with a 2 µm-wavelength laser for future EUV lithography **17**
- 2.1 Introduction . . . 18
- 2.2 Radiation-hydrodynamic simulations . . . 19
  - 2.2.1 Code details . . . 19
  - 2.2.2 Target and laser conditions . . . 20
- 2.3 Analysis of simulations and theoretical modeling . . . 21
  - 2.3.1 Time-integrated in-band profiles . . . 21
  - 2.3.2 Instantaneous conversion efficiency, droplet trajectory dynamics, and mass ablation rate . . . 24
  - 2.3.3 Laser refraction and EUV source properties . . . 29
- 2.4 Conclusion . . . 31
- 2.5 Appendix . . . 31
  - 2.5.1 Derivation of the droplet propulsion model . . . 31
  - 2.5.2 Simulation results for 45 µm diameter droplet . . . 33

3 Ion emission properties of tin plasmas generated by 2 µm-wavelength laser pulses **37**
- 3.1 Introduction . . . 38
- 3.2 Simulation parameters . . . 39
- 3.3 Short pulse simulation . . . 40
- 3.4 Long pulse simulation . . . 42
  - 3.4.1 Energy-resolved ion spectrum . . . 42
  - 3.4.2 Angle-resolved ion spectrum . . . 44

3.4.3 Knudsen number . . . 47
3.5 Conclusion . . . 49

4 A refined model for laser absorption in plasmas involving the Langdon effect 51
4.1 Introduction . . . 52
4.2 Theory . . . 53
4.2.1 The Langdon effect and electron distribution functions . . . 53
4.2.2 Impact parameters . . . 55
4.2.3 Laser absorption involving super-Gaussian electron distributions . . . 56
4.3 Wavelength and intensity scans . . . 62
4.4 Conclusion . . . 64
4.5 Appendix . . . 65

5 Super-Gaussian integration for the Langdon effect 67
5.1 Introduction . . . 67
5.2 Absorbed laser power . . . 68
5.3 Rewriting the integral . . . 70
5.4 Small-η expansion . . . 71
5.5 Conclusion . . . 76
5.6 Appendix . . . 77

6 Conclusion & Outlook 81
6.1 Summary . . . 81
6.2 Outlook . . . 83

List of Publications 85

Bibliography 87

Acknowledgments 99

Chapter 1

Introduction

It may be said that the physicist's two jobs are to be surgically precise, and to be barbarically crude. Meticulous effort, for instance, is put into measuring the magnetic moment of the electron. If the observed value of this fundamental quantity deviates from theory, it would be proof of physics unexplained by the Standard Model. But despite recent measurements pinning it down with an accuracy of 0.13 parts per trillion, the Standard Model has refused to yield.[1]

When the laws of nature are firmly established, theoretical physics becomes an exercise in what to leave out. That is: calculate which forces, processes, expansion terms, *etc.*, are dominant in a given system, and ignore the rest. Too much detail makes the theory unwieldy or uninsightful, while too little detail renders it inaccurate. As we will now see, this is elegantly demonstrated in the derivation of the *Taylor–von Neumann–Sedov blast wave*.

1.1 Calculating the yield of an atomic bomb

In 1950, Sir Geoffrey Ingram Taylor published two articles in the *Proceedings of the Royal Society*.[2,3] Based on declassified photographs of the *Trinity* nuclear test, Taylor had managed to disclose a closely-guarded military secret: the energetic yield of the atomic bomb.

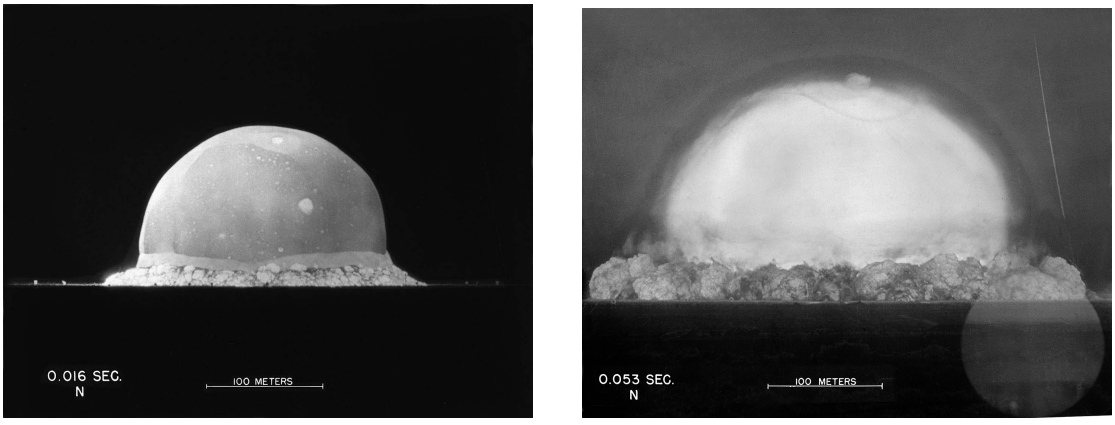


Figure 1.1: Two photos of the *Trinity* test blast wave, with time after detonation and size indicated.[4,5]

Taylor was recruited for the Manhattan Project to study the physics of an atomic bomb blast. In conventional explosives, a chemical reaction produces a hot, pressurized gas which

violently expands. An atomic bomb, on the other hand, releases energy through nuclear fission without forming a gas. He therefore imagined an initial, highly concentrated source of energy E. This point source then expands radially, producing an intense blast wave: a pressure front whose outer radius moves faster than the speed of sound.[6] The radius R of this blast wave grows as a function of time t. Inside the blast wave, at any radial distance r from the center, and any time t, we consider the variables pressure, density, and flow velocity. Outside the blast wave is ambient air of density ρ_0 with a ratio of specific heats γ. Taylor assumed that the pressure outside the blast wave can be neglected. The radius $R(t)$ of the expanding blast wave must, then, be a function of the quantities that make up the problem:

$$R(t) = S(\gamma)\left(\frac{Et^2}{\rho_0}\right)^{1/5}. \tag{1.1}$$

Since this combination of E, t, and ρ_0 is the only way to produce units of distance, the formula is strongly constrained. The only component with any freedom is the prefactor $S(\gamma)$. *A priori*, this S can be any function of the dimensionless γ—large, small, steep, or constant. This procedure of dimensional analysis is mathematically formulated in the Buckingham π theorem.[7]

This is as far as the story is usually told, with the hand-waved assumption that $S(\gamma) \approx 1$. But an exact result can in fact be derived, and while it is not as succinct as a straightforward application of dimensional analysis, it is all the more ingenious. With the expression for the blast radius given above, it is possible to *nondimensionalize* the fluid equations: express radial distance in terms of R, density in terms of ρ_0, *etc.* It turns out that the fluid equations, as considered in this scenario, possess a special symmetry called *self-similarity*: they can be written as a function of $\xi \equiv r/R(t)$, without r or t appearing explicitly in the equations. This means that, at any point in time, the explosion looks like any other point in time, up to a scaling of the blast radius.

After numerically solving an integral expression, Taylor found that indeed $S(\gamma) \approx 1$ for atmospheric gas. Using the timestamped photos of the explosion, he was able to calculate E, the yield of the atomic bomb: he concluded that the *Trinity* explosion had the energetic equivalent of 17–24 kilotons of TNT.* This turned out to be remarkably close to the actual number, 20 kilotons.

By considering simplicity (negligible ambient pressure, constant γ) and symmetry (spherical expansion), Taylor succeeded in giving an elegant and reasonably accurate description of something as massive and as violent as a nuclear explosion. In fact, two other physicists, John von Neumann and Leonid Sedov, described the same process around the same time.†

1.2 What is a plasma?

Plasma physics, the topic of this thesis, is built upon such clever calculations. It is a field that is closely connected to a great variety of disciplines, such as fluid dynamics, quantum

*The given range is due to variability of γ within the blast, as this quantity is in fact temperature-dependent.
†For an insightful review of Taylor's work and comparison with von Neumann's and Sedov's, see Ref. [8].

mechanics, electromagnetism, and thermodynamics. With such complexity, one can only hope to describe (and simulate) plasmas by considering idealized scenarios and identifying which length scales and time scales dominate the behaviour. In this section, I will give an overview of the physics of plasmas relevant for this thesis. I will treat plasmas from several perspectives, for which I provide a conceptual explanation, along with an overview of the basic mathematics.

1.2.1 Plasma as an ionized gas

Plasmas are sometimes considered the fourth state of matter.[9] In terms of temperature, they are the state found when gases are further heated. The transition from gas to plasma is called ionization. It occurs when atomic collisions are sufficiently energetic to rip electrons from their atomic orbits, creating a mix of free electrons and positively charged ions. However, the transitions *solid* $\rightarrow$ *liquid* and *liquid* $\rightarrow$ *gas* are different from *gas* $\rightarrow$ *plasma*. For melting and vaporization, there is a specific temperature at which the phase transition between the two states occurs. This is not the case for ionization; it is a gradual process. The hotter a plasma, the higher the average number of free electrons per atom. This charge separation into ions and free electrons gives the plasma its distinct electromagnetic properties.

The degree of ionization can be calculated by considering a plasma in thermodynamic equilibrium. If the ionization potential for each electron, χ_i—that is, the energy required to strip away consecutive electrons from the ion—is known, and the plasma is in thermodynamic equilibrium, the abundances of each charge state i can be found. This is quantified by the *Saha ionization equation*:[10]

$$\frac{n_{i+1}n_e}{n_i} = 2\left(\frac{2\pi m_e k_B T}{h^2}\right)^{3/2} \frac{g_{i+1}(T_e)}{g_i(T_e)} e^{-\chi_i/k_B T}. \tag{1.2}$$

Here, n_i and n_{i+1} are the total populations of charge states i and $i+1$.* n_e is the free electron density, m_e is the electron mass, h is Planck's constant, k_B is Boltzmann's constant, and T is the temperature. g_i is the statistical weight of the ground state-level for charge state i. In order to have a significantly ionized plasma, we therefore need a gas with a temperature on the order of first ionization energy. For tin, this value is 7.34 eV, corresponding to a temperature of $\sim$85 000 K.

While the Saha equation broadly yields the charge state distribution, most plasmas are not in thermodynamic equilibrium. For instance, there could be an imbalance between radiative recombination and its reverse process (photoionization, see Fig. 1.3) if the plasma is transparent and radiation can escape. In that case, one needs precise knowledge of the atomic structures and the rates of all collisional and radiative processes that act to populate and depopulate each state.[11]

1.2.2 Coulomb collisions

Each charged particle in a plasma exerts a Coulomb force on every other charged particle. This force is long-range, with a $1/r$ potential. Collisions are modelled using the Boltzmann

*In the above equation, i refers to the level index, rather than the charge state.

collision operator C (see also Eq. 1.5), which considers every local pair of particles, their velocities, and their cross sections. By using the statistical randomness of collisions, the collision rate is evaluated by integrating over a range of 'impact parameters', b. For Coulomb scattering, such as that shown in Fig. 1.2, this approach is problematic, because the integral diverges:

$$C \propto \int_0^\infty b^{-1} db \to \infty. \tag{1.3}$$

In other words, there are significant interactions between particles of *any* distance.

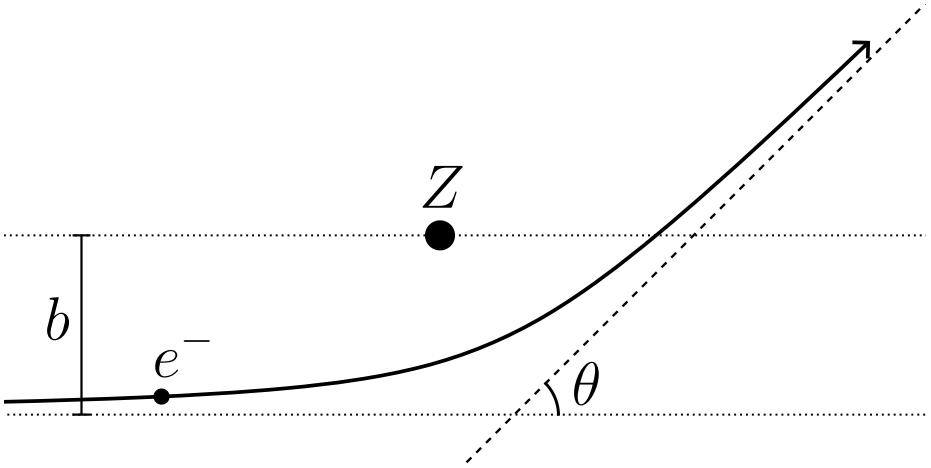


Figure 1.2: Schematic of an electron scattered by an ion.

In order to say anything sensible about a plasma without modelling the entire universe, we need something more. We are helped greatly by the fact that electrons are much lighter than ions: for a simple hydrogen nucleus (a proton), the ion-to-electron mass ratio is 1836 to 1. Tin (Sn) ions are 118.7 times heavier yet. Free electrons will therefore generally be faster than the sluggish ions, and are much more prone to 'bouncing around': from the electron's point of view, the ions are virtually stationary, and the electrons are able to fully thermalize around them. The result is that the ions get 'screened' by the electrons: damped by the surrounding electrons, the effective ionic Coulomb potential decays over a characteristic distance called the *Debye length*. This provides a finite upper cut-off b_{max} for the integral Eq. 1.3. The integral can be given a nonzero lower cut-off b_{min} too, since the above expression is valid only for weak interactions at large b, and interactions of impact parameters smaller than b_{min} are rare. The result is a finite *Coulomb logarithm*, $\ln \Lambda \equiv \ln(b_{max}/b_{min})$.

The Debye length can be obtained by solving the Poisson equation for the combined potential of the ion and surrounding electrons. The result is

$$V(r) = \frac{Z_i e}{4\pi\epsilon_0 r} e^{-r/\lambda_D}, \quad \lambda_D = \sqrt{\frac{\epsilon_0 k_B T}{n_e e^2}}, \tag{1.4}$$

where λ_D is the Debye length, and Z_i is the charge state of the screened ion. For the lower cut-off b_{min}, the impact parameter for perpendicular scattering $b_\perp$ is typically chosen; that

is, an incident electron with impact parameter $b_\perp$ will make a 90° scattering angle with respect to the ion.[12] Interactions with impact parameters on the order of $b_\perp$ strongly affect the projectile particle's momentum, but are also extremely rare if the plasma is weakly coupled (explained below), and can therefore be neglected. An extensive analysis of cut-off values for a laser-produced plasma is given in Chapter 4.

Note that there must be enough electrons in a spherical region of radius λ_D around each ion for the above approach to be statistically valid. This condition can be written as $n_e \lambda_D^3 \gg 1$. It can be cast in a form that will be useful later on: let $b_{\perp t} \equiv Z_i e^2/(4\pi\epsilon_0 k_B T)$ be the impact parameter for the perpendicular scattering of an electron moving at thermal velocity, and define $\Lambda \equiv \lambda_D / b_{\perp t}$, the *plasma parameter*. The above condition is equivalent to $\Lambda Z_i / 4\pi \gg 1$, or more crudely $\Lambda \gg 1$. If this holds, the plasma is said to be *weakly coupled*;[13] it guarantees that the ions are properly screened, that electrons are generally deflected weakly by ions, and thus that the Coulomb logarithm $\ln\Lambda$ can be used in scattering theory. In strongly coupled plasmas, large-angle deflections dominate electron motion, and as such these are much harder to analyze.[14]

Because of Debye screening, plasmas of a size much larger than λ_D are *quasi-neutral*: although the plasma may have small electromagnetic fluctuations that are capable of sustaining waves, there will be no long-range interactions. Seen from far away, the plasma is non-charged.

Collisions in gases and plasmas can be described using kinetic theory. The positions $\mathbf{x}$ and momenta $\mathbf{p}$ (or velocities $\mathbf{v}$) of particles are modelled as a continuous distribution function in phase space, with phase space density $f(\mathbf{x}, \mathbf{p}) \equiv d^6 n_e / dx^3 dp^3$. Motion is described by the *Boltzmann equation*:[15]

$$\frac{\partial f}{\partial t} + \frac{\mathbf{p}}{m} \cdot \nabla f + \mathbf{F} \cdot \frac{\partial f}{\partial \mathbf{p}} = \left(\frac{\partial f}{\partial t} \right)_{\text{coll}} . \tag{1.5}$$

$\mathbf{F}$ denotes forces acting on the particles. The term on the right is the *collision operator*: it encodes interactions between particles which result in scattering. Without it, particles would be flying right through each other. The general form of this operator is quite involved: the scattering angle depends on the type of force the colliding particles exert (or their differential cross section), their velocities, and the impact parameter. For Coulomb collisions, one finds the *Landau collision operator*. The exact form of this operator is beyond the scope of this thesis, but it gives rise to the various collision rates between particles in the plasma. Given an expression for the Coulomb logarithm, collision rates between different plasma species can be derived. We only cite the result here, for a plasma with ionic charge state Z_i, electron density n_e, ion density n_i, electron temperature T_e, and ion temperature T_i:[16*]

*There is some disagreement in the literature on the prefactors. The reader is invited to consult the NRL Plasma Formulary,[17] Braginskii,[18] and Mantas.[19]

$$\nu_{ee} = \frac{4\sqrt{\pi}}{3} \frac{e^4 n_e \ln \Lambda_{ee}}{(4\pi\epsilon_0)^2 m_e^{1/2} (k_B T_e)^{3/2}}, \tag{1.6}$$

$$\nu_{ei} = \frac{4\sqrt{2\pi}}{3} \frac{Z_i^2 e^4 n_i \ln \Lambda_{ei}}{(4\pi\epsilon_0)^2 m_e^{1/2} (k_B T_e)^{3/2}}, \tag{1.7}$$

$$\nu_{ii} = \frac{4\sqrt{\pi}}{3} \frac{Z_i^4 e^4 n_i \ln \Lambda_{ii}}{(4\pi\epsilon_0)^2 m_i^{1/2} (k_B T_i)^{3/2}}, \tag{1.8}$$

$$\nu_{ie} = \frac{4\sqrt{2\pi}}{3} \frac{Z_i^2 e^4 n_e m_e^{1/2} \ln \Lambda_{ie}}{(4\pi\epsilon_0)^2 m_i (k_B T_e)^{3/2}}. \tag{1.9}$$

Here, ν_{ei} is read as, "The number of times an electron collides with an ion of charge state Z_i per unit of time." A collision is here defined as a deflection with an angle $> 90°$. Likewise, ν_{ie} is defined as the number of times an ion collides with an electron per unit of time. Such an event is intuitively much rarer due to the ion's larger inertia. When the two temperatures are approximately equal and $Z_i = 1$, the following hierarchy of collision rates is found:

$$\nu_{ee} \sim \nu_{ei} \gg \nu_{ii} \sim \sqrt{\frac{m_e}{m_i}} \nu_{ei} \gg \nu_{ie} \sim \frac{m_e}{m_i} \nu_{ei}. \tag{1.10}$$

1.2.3 Plasma as a fluid

The quasi-neutrality of the plasma discussed in the previous section is actively maintained: if electrons and ions separate, an electric potential is formed which restores quasi-neutrality.[20] One can describe motion of such a quasi-neutral plasma by considering only the ions. For the ions to move *as a fluid*, they must interact locally. What this means is that the average distance between collisions, the *mean free path length* λ_{mfp}, must be much smaller than the characteristic length scale L of the plasma.

By assuming that the plasma is close to local thermodynamic equilibrium, the phase space density $f(\mathbf{x}, \mathbf{v})$ from Eq. 1.5 can be written as an expansion in terms of the Maxwell–Boltzmann equilibrium distribution,

$$f_{\text{eq}}(\mathbf{v}) = 4\pi v^2 \left(\frac{m_i}{2\pi k_B T} \right)^{3/2} \exp\left(-\frac{m_i v^2}{2 k_B T} \right), \tag{1.11}$$

such that $f(\mathbf{x}, \mathbf{v}) = n_i(\mathbf{x}) f_{\text{eq}}(\mathbf{v})$. Note that $\mathbf{p} = m_i \mathbf{v}$, so $\mathbf{v}$ may replace the momentum coordinates. This is called the Chapman–Enskog expansion.[21] Each term is characterized by a power of Kn, the *Knudsen number*:

$$\text{Kn} \equiv \frac{\lambda_{\text{mfp}}}{n_i / |\nabla n_i|}, \tag{1.12}$$

where the length scale is thus $L \equiv n_i/|\nabla n_i|$. The mean free path length λ_{mfp} is defined as the thermal velocity v_t divided by the collision rate ν.

The Knudsen number is a dimensionless quantity. It compares two length scales of the system: the mean free path length λ_{mfp}, and the local length scale of density fluctuations. If Kn is small, higher-order terms of the expansion of f can be ignored; retaining only the first-order terms, one obtains the *Navier–Stokes equations*:

$$\frac{\partial \rho}{\partial t} + \nabla \cdot (\rho \mathbf{u}) = 0, \tag{1.13}$$

$$\frac{\partial}{\partial t}(\rho \mathbf{u}) + \nabla \cdot (\rho \mathbf{u} \otimes \mathbf{u}) = -\nabla p + \mu \nabla^2 \mathbf{u}, \tag{1.14}$$

$$\frac{\partial}{\partial t}(\rho E) + \nabla \cdot [(\rho E + p)\mathbf{u}] = Q_T + Q_r + Q_{\text{dep}} + Q_{\text{vis}}. \tag{1.15}$$

These are the three equations of conservation in fluid dynamics.[22] Eq. 1.13 encodes conservation of mass: ρ is mass density, and $\mathbf{u}$ is the velocity vector. Eq. 1.14 represents conservation of momentum: p is pressure, and μ is dynamic viscosity. While viscous forces are not modelled in the hydrodynamics code used in this thesis, I include them in the equation for completeness.* Eq. 1.15 is for conservation of energy: $E \equiv e + u^2/2$ is the total mass-specific energy (internal + kinetic), and Q is the volumetric heating rate. We distinguish heating through thermal conduction Q_T, heating (cooling) through absorption (emission) of radiation Q_r, and heating by other external energy sources such as a laser pulse Q_{dep}. Q_{vis} represents heating from viscous friction.

A hydrodynamic system of equations requires closure through an *equation of state*. Specifically, one needs expressions to specify quantities such as pressure p and temperature T as a function of ρ and e. Examples of these are the polytropic ideal gas and the (generalized) van der Waals equation of state. The equation of state used in this thesis is called `FEOS`.[23] In the `FEOS` model, the Helmholtz free energy is computed as a sum of three components: an electronic term, based on Thomas–Fermi theory; an ionic term, based on models such as Einstein, Debye, or Cowan; and a semi-empirical bonding correction. From the Helmholtz free energy, quantities such as p and e can be derived. It also provides values for the average charge state using a simplistic (non-Saha) approach.

Fourier's law dictates the flow of heat due to temperature gradients: $\mathbf{q} = -\kappa \nabla T$; the volumetric heat gain due to thermal conduction is defined $Q_T \equiv \nabla \cdot \mathbf{q}$. The thermal conductivity κ of a plasma is calculated by Spitzer[20] and extended by Brysk *et al.*;[24] see these works, as well as the work of Aggarwal *et al.*[25] for details.

The free plasma electrons can sustain *Langmuir waves*. These are density waves of the electrons due to the electric field of the (stationary) ions. The electrons oscillate with the *plasma frequency*,

*The importance of viscous effects is indicated by the Reynolds number: $\text{Re} \equiv \rho u L/\mu$.

$$\omega_p = \sqrt{\frac{n_e e^2}{\varepsilon_0 m_e}}. \tag{1.16}$$

The plasma frequency is a fundamental characteristic of the plasma. These electron oscillations also affect the propagation of electromagnetic waves (light), as they modify the dispersion relation:

$$\omega^2 = \omega_p^2 + c^2 k^2. \tag{1.17}$$

When a laser beam of angular frequency ω_L is fired into a plasma, the wavelength is determined by the dispersion relation. The beam cannot penetrate beyond the *critical density*

$$n_c \equiv \frac{\varepsilon_0 m_e \omega_L^2}{e^2} = \frac{\varepsilon_0 m_e 4\pi^2 c^2}{\lambda_L^2 e^2}. \tag{1.18}$$

The wavelength of the laser light in the vacuum is written as λ_L. At the critical density, $\omega_p = \omega_L$ and the wavelength tends to infinity ($k \to 0$). The wave will be reflected, while an evanescent electric field extends beyond the critical surface with a skin depth of k^{-1}.

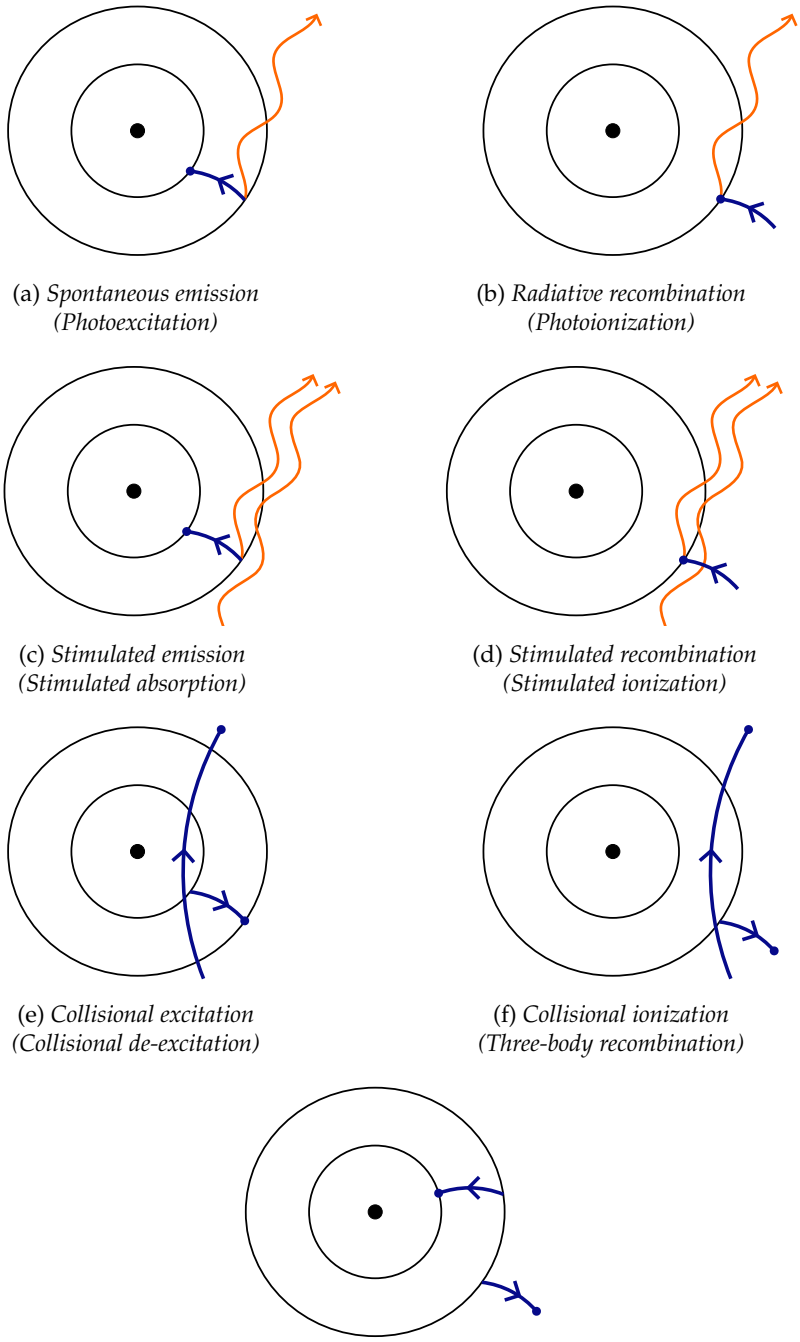
1.2.4 Radiation in plasma

The tin plasmas considered in this thesis contain ions with open $4d$-subshells, and consequently have a large number of radiative channels. For instance, Sn^{12+} has 10^{10} allowed dipole transitions.[26] Radiation therefore plays a prominent and intricate role in these plasmas. Ions and electrons constantly interact, emitting and absorbing photons. The rate of photon absorption and emission is a result of quantum-mechanical processes involving the myriad electronic states and the transitions between them.

Electronic processes can be divided into three categories, defined by what happens to the electron with which it interacts. In *bound–free* transitions, a photon is absorbed by an atom, which ionizes a bound electron; in *bound–bound* transitions, the photon induces an electronic transition from one orbital to another. Fig. 1.3 shows the most notable processes involving a photon and an electron (a–d), and two electrons (e–g). For *free–free* transitions, a free electron interacts with a photon and remains free. Each process is characterized by a certain *cross section* σ: the classically visualized 'area' of the atom the photon should strike for the process to occur.[27]

The frequency (ν)-specific *absorption coefficient* α_ν (also written k_ν) can be obtained by considering photoabsorption processes as well as stimulated emission.* For every transition between two states, σ is multiplied with the number of states per volume. The absorption coefficient is used to calculate the loss of intensity I_ν over distance: $dI_\nu/dx = -\alpha_\nu I_\nu$.

*Stimulated emission is of course an emission process, but since it is intensity-dependent in the same manner as photoabsorption, it can conveniently be included (with a minus sign) in the absorption coefficient.



(a) *Spontaneous emission (Photoexcitation)*

(b) *Radiative recombination (Photoionization)*

(c) *Stimulated emission (Stimulated absorption)*

(d) *Stimulated recombination (Stimulated ionization)*

(e) *Collisional excitation (Collisional de-excitation)*

(f) *Collisional ionization (Three-body recombination)*

(g) *Autoionization (Resonant capture)*

Figure 1.3: Abstract depiction of relevant atomic processes, with the reverse processes given in parentheses.[10] The two black circles represent two different energy levels; blue curves are electronic transitions, and orange curves are photons.

The emission coefficient η_ν, due to photoemission processes, can likewise be calculated: $dI_\nu/dx = \eta_\nu$.[28]

Radiation in plasmas is described with the *radiative transfer equation* (RTE). Light consists

of optical rays of a frequency ν and an intensity I_ν; this is the *specific intensity*, *i.e.* the electromagnetic energy flux, per area, per solid angle, per unit time, per frequency. I_ν is a function of position $\mathbf{x}$ and propagation direction $\hat{\mathbf{\Omega}}$. Using the opacities and emissivities defined above, the RTE assumes the following form:

$$\frac{1}{c}\frac{\partial I_\nu}{\partial t} + \hat{\mathbf{\Omega}} \cdot \nabla I_\nu = -(k_{\nu,s} + k_{\nu,a}) I_\nu + \eta_\nu + \frac{k_{\nu,s}\rho}{4\pi} \int I_\nu d\Omega. \tag{1.19}$$

As a ray of frequency ν propagates through space in direction $\hat{\mathbf{\Omega}}$, it loses intensity through scattering (the leftmost $k_{\nu,s}$ term) and absorption ($k_{\nu,a}$), while gaining intensity from emission (η_ν) and scattering from other directions (the $k_{\nu,s}$ term on the far right).

Absorption due to *free–free* transitions, known as *inverse bremsstrahlung absorption* (IBA), plays a distinguished role in laser absorption in a plasma. Bremsstrahlung is electromagnetic radiation emitted by a de-accelerating charged particle, and exists in both classical and quantum theory. IBA is the inverse process; in a plasma, it refers to the absorption of photons by electrons. For a laser of frequency ω_L, the absorption coefficient in a plasma of charge state Z_i and temperature T is given by Kramers' formula:[29]

$$k_\omega = \frac{16\sqrt{2}\pi^{3/2}}{3} \left(\frac{e^2}{4\pi\epsilon_0}\right)^3 \frac{Z_i^2 n_e n_i}{(m_e k_B T)^{3/2} c \omega_L^2} \ln\Lambda. \tag{1.20}$$

1.2.5 Other considerations

We can make some further assumptions to simplify our notion of plasma. If the collision time between electrons and ions is short compared to the hydrodynamic time scale (which we find to be on the order of nanoseconds), kinetic energy is exchanged between electrons and ions such that the plasma as a whole is in thermodynamic equilibrium, and a *single-temperature* model can be adopted: $T_e = T_i$.

The plasma consists of different charge states, which have different Coulomb forces and therefore contribute differently to quantities like the Debye length, thermal conductivity, and absorption rate. We can therefore simply consider the average charge state $\bar{Z} \equiv n_{tot}^{-1} \sum_i Z_i n_i$, where the i indicates the ionic charge state. This also means $n_e = \bar{Z} n_i$. Since some equations depend on the square of Z_i, a small variance in charge state distribution is required for this approach to be accurate.

1.2.6 The Langdon effect

In thermal equilibrium, the velocities of electrons in a plasma follow a Maxwellian distribution (Eq. 1.21). In the presence of the electric field of a laser, however, the electron velocity distribution is perturbed into a 'super-Gaussian' distribution:

$$f_m(v) = C_m \frac{n_e}{2^{3/2} v_t^3} \exp\left(-\left[\frac{v}{\alpha_e \sqrt{2} v_t}\right]^m\right), \tag{1.21}$$

Various super-Gaussian distribution functions are plotted in Fig. 1.4. The characteristic property of the super-Gaussian distribution is the parameter m: depending on the strength of the laser relative to the strength of thermal collisions, m ranges from 2 (no laser; Maxwellian) to 5 (very strong laser). This phenomenon is called the *Langdon effect*, and it results in a decrease of the laser light absorption coefficient.[30] Details of the super-Gaussian distribution function and the Langdon effect are given in Chapter 4, where laser absorption in plasmas is studied in detail.

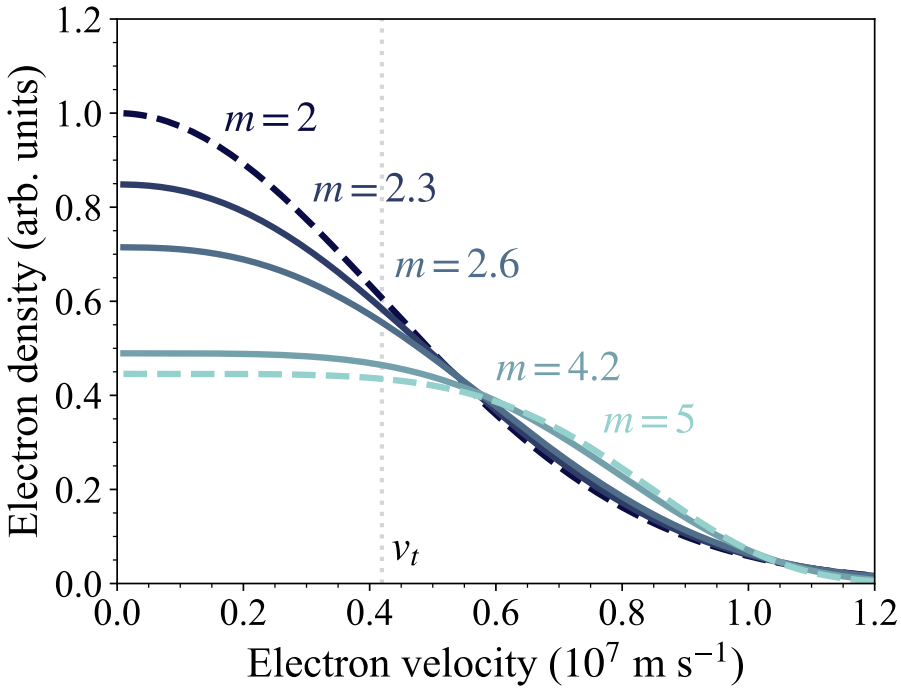


Figure 1.4: Scaled super-Gaussian electron velocity distributions for selected values of m.

1.3 EUV nanolithography

At last, we arrive at the main topic of this thesis: EUV-emitting plasmas. 'Extreme ultraviolet' (EUV) denotes a range of light-wavelengths commonly defined to be 10–121 nm.[31] In particular, tin plasma has a remarkably strong emission peak around 13.5 nm. This narrow emission range is exploited in the process of EUV nanolithography.[32]

Nanolithography is the process of printing nanometer-scale patterns on a material. For our purpose, it concerns the production of computer chips by creating nano-scale integrated circuits on a silicon wafer. Working on such a fine scale, however, is no simple task. One way to reach the necessary level of resolution is through *photo*lithography: lithography with light. When focusing a beam of light of wavelength λ using mirrors or lenses to print patterns, resolution is fundamentally limited by diffraction. This is called the *Rayleigh criterion*:

$$\mathrm{CD} = k_1 \frac{\lambda}{\mathrm{NA}}. \tag{1.22}$$

The critical dimension CD is the smallest feature-size that can be resolved by the beam; NA is the numerical aperture, a measure of how much angular spread of the beam the system can handle (NA $= n \sin\theta$, where n is the refractive index of the medium, and θ is the half-angle of the beam), and the k_1 is the so-called process parameter which represents other practical limitations from the optics, pattern, *etc.*[32]

Thus, to minimize the critical dimension, short-wavelength light is necessary. But not just any wavelength will do; EUV light is reflected very poorly by common optical materials. State-of-the-art nanolithography relies on molybdenum/silicon multilayer mirrors to transport and shape the EUV light beam.[33] These mirrors have a reflectivity of $\sim 70\%$, but only within a narrow wavelength band of 13.5 ± 0.135 nm. This is where tin comes in. It just so happens that tin plasma, at the right temperature, has a relatively high 'spectral purity': simulations have shown[34] that it can emit $\gtrsim 40\%$ of radiative energy in the $13.5 \pm 1\%$ nm* 'in-band' range in highly idealized conditions. This assumes a homogeneous, optically thin plasma at optimal temperature. In practical settings, the efficiency is significantly lower. In any case, this narrow and intense in-band emission originates from transitions between multiply-excited states, all occurring around this wavelength.[26,35]

Nanolithography is a rapid-fire, industrial-scale process, wherein a droplet generator spits a stream of tin microdroplets into a vacuum chamber. The droplets are turned into a plasma using an irradiation recipe of three laser pulses:[36] first, a 'pre-pulse' is fired on the droplet to turn it into a thin, liquid sheet; then a rarefaction pulse hits the sheet, turning it into a tin vapor;[37] finally, the 'main pulse' from a CO_2 laser heats up this vapor, producing an EUV-emitting plasma. A collector mirror focuses the EUV light to a point, and from there it is further shaped as it propagates through the machine; ultimately, it is used to encode patterns on the silicon wafer. With the latest technology, this process can be performed at a rate of about 100 000 times per second, producing 1 kilowatt of in-band EUV power.[38,39]

Besides high power, a high *conversion efficiency* (CE) is also desired. This is the ratio of the useful, in-band EUV light produced, relative to the energy used by the main pulse. Specifically, only the radiation emitted in the 2π sr solid angle around the laser is considered for CE, as this comprises the span of the collector mirror.

The goal of this thesis is to better understand the physics of the tin plasma and its interaction with the laser. Specifically, we consider a novel setup, wherein the CO_2 laser is replaced with a $\sim$2 µm-wavelength, solid state laser. This type of laser has several advantages, namely a higher wall-plug efficiency, a smaller footprint, and a shorter wavelength (1.88 µm,[40] as opposed to 10.6 µm for the CO_2 laser). Crucially, this type of laser can also sustain pulses that are hundreds of nanoseconds long—long enough to burn through the droplet without the aid of a pre-pulse.

Research into laser–droplet interaction in this thesis is conducted using the code `RALEF-2D`.[41] *RALEF* stands for *Radiative Arbitrary Lagrangian–Eulerian Fluid dynamics*. Based on the `CAVEAT` hydrodynamics package developed at the Los Alamos National Laboratory in the 1980s, `RALEF-2D` was created in 2007 to help interpret the results of laser–plasma experiments performed at the GSI Helmholtz Centre for Heavy Ion Research. As its name suggests, the code simulates both fluid dynamics and radiative transport in a 2-dimensional setting. The simulation space is modelled as a numerical mesh built up from rectangular 'blocks', each of which consists of a fixed number of cells. At each time step, cellular

*Equivalent to $91.84 \pm 1\%$ eV.

values—principally density, velocity, and specific internal energy—are updated using the second-order Godunov method.[42] At specified times, spatial quantities can be printed as *VTK* (*Visual ToolKit*) files; see Fig. 1.5.

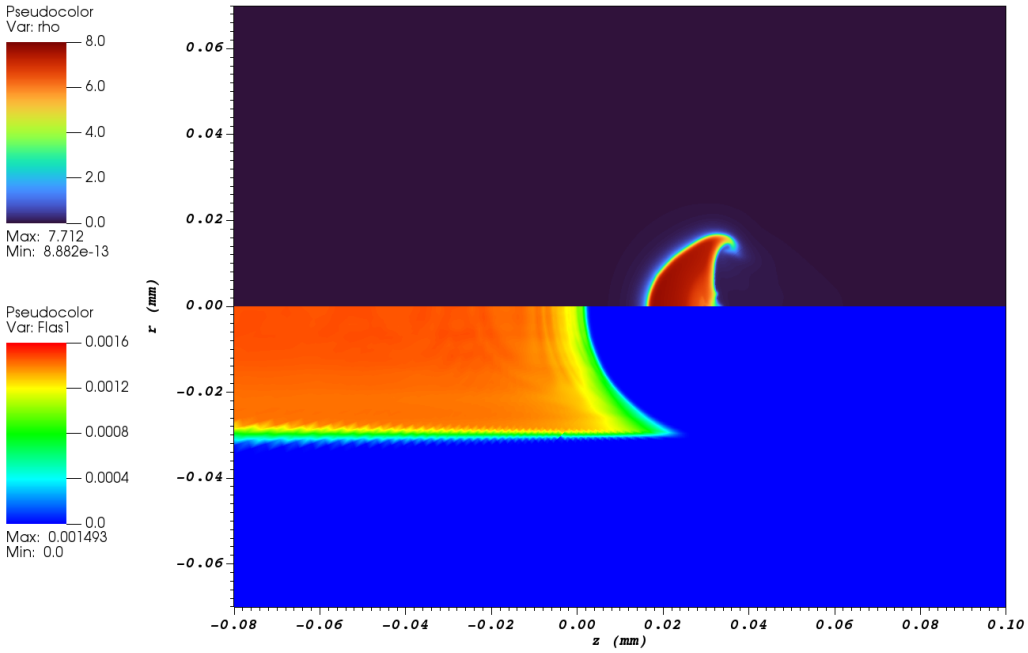


Figure 1.5: A screenshot from the `VisIt` software showing a tin droplet being irradiated by a laser pulse. The top half of the image shows the local density, while the bottom half shows the laser intensity.

Equation-of-state (EOS) variables are computed using `FEOS` (see section 1.2.3). `RALEF-2D` accepts pre-calculated logarithmic tables with quantities as a function of density and temperature. These quantities are: pressure, sound speed, internal energy, average charge state, specific heat capacity at constant volume, and the so-called strong-shock parameter. Note that the tables provide internal energy as a function of temperature, even though internal energy is already calculated by the hydrodynamic equations. The unknown is in fact the temperature, and this is obtained by reverse-searching the `FEOS` table.

Radiation is modelled using the RTE, Eq. 1.19. In full generality, this is a seven-dimensional integro-differential equation; numerical modelling requires significant simplifications. The time derivative is dropped, as I_ν is assumed to vary slowly on the hydrodynamic time scale; this is the quasi-static approximation. The scattering terms are neglected as well. Finally, the plasma is assumed to be in *local thermodynamic equilibrium* (LTE): this implies that photons are thermally distributed according to Planck's law, with the following spectral radiance:

$$B_\nu(T) = \frac{2h\nu^3}{c^2} \frac{1}{e^{\frac{h\nu}{k_B T}} - 1}. \tag{1.23}$$

In LTE, emission is balanced by absorption, so $\eta_\nu = B_\nu \alpha_\nu$. The emission coefficient can be eliminated, such that the RTE is used in the following form:

$$\hat{\mathbf{\Omega}} \cdot \nabla I_\nu = k_\nu (B_\nu - I_\nu). \tag{1.24}$$

The continuous spectrum of light frequencies is simplified to a discrete set of frequency groups, and frequency-specific opacities k_ν are supplied in tabulated form. These are obtained from the THERMOS code.[43] For the simulations in this thesis, there are 28 frequency groups, two of which make up the $13.5 \pm 1\%$ in-band range.

Discretizing the set of radiation propagation directions ($\hat{\mathbf{\Omega}}$) is accomplished with the S_n method. This consists in restricting radiation propagation to a finite set of directions, such that each octant of (x, y, z)-space is given a symmetric triangle of $k(k+1)/2$ beamlets (propagation directions). The RTE is then used to update I_ν. The laser is treated separately: it consists of a number of pre-defined rays whose local intensity falls off according to the absorptivity k_ν from Kramers' formula, Eq. 1.20, or from the Drude model. Geometric optics theory, which underpins Eq. 1.19, is used in underdense plasmas. When this approach is no longer accurate, the code switches to solving the Helmholtz equations for electromagnetic fields.

Finally, 'Arbitrary Lagrangian–Eulerian' refers to how the mesh is updated. In an Eulerian mesh, the mesh is stationary and matter moves through it, from cell to cell; in a Lagrangian mesh, motion is implemented by updating the locations of the cells themselves. RALEF-2D uses a two-step process to combine the two approaches: the *rezoning* phase, in which the mesh is moved (based on local flow speed, for instance), followed by the *remapping* phase, wherein state variables from the old mesh are transferred to the updated one.

1.4 Research questions and thesis outline

The research presented in this thesis is motivated by questions concerning EUV source plasmas. Numerical simulations of the laser–droplet interaction serve to complement experimental data, and can yield insight without (or before) overcoming the challenges associated with experimental technology and diagnostics. A particular laser model may be limited in terms of wavelength, intensity, beam shape, *etc.* Adjusting these may involve ordering new components, installing them, testing, and benchmarking. The development cycle is costly and time-consuming. Computationally, this can be (though certainly not always is) as simple as changing a parameter and re-running the simulation. Simulations are also more 'complete', in the sense that they provide information about any quantity—temperature, density, absorption—at any point in time and space, which helps not just to maximize efficiency, but also to understand the internal physical mechanisms of the plasma.

In this thesis, the role of simulations is forward-looking. A 2 µm-wavelength laser has been identified as a candidate for future EUV nanolithography, and its pulse, with a duration of more than one hundred nanoseconds, permits sustained EUV generation without prior target shaping. In **Chapter 2**, we study the properties of this novel setup. Firing a laser of 2 µm wavelength on a droplet and completely vaporizing it raises a slew of questions: How long does it take for the droplet to be vaporized? How much in-band EUV light is produced? Where in the plasma is laser light absorbed? How much does the droplet move during irradiation, and can this motion be modelled mathematically? In order to identify

optimal irradiation recipes, we investigate a range of laser intensities ($0.7–3.5\times10^{11}$ W cm^{-2}) and droplet sizes (30, 40, and 45 µm diameter).

Chapter 3 is a direct follow-up on the previous chapter. Here, we study ion emission from the EUV source. This emission is a practical concern, as highly-energetic tin ions may damage or coat the collector mirror, and reduce the efficiency of the machine over time. Two cases are considered. Firstly the 'long pulse' case, operating with an intensity of 1.4×10^{11} W cm^{-2}, which fully vaporizes the droplet over 150 ns; this pulse was previously identified to be of practical interest, and represents the 'main pulse only' scheme. Secondly the 'short pulse' case, with intensity 1.0×10^{11} W cm^{-2} and a finite pulse length of 27 ns; this was chosen for comparison with experiments with presently available technology. We ask: what does the ion kinetic energy spectrum look like for these cases? In what way do these spectra differ from the (shorter-pulse) simulations investigated by Hemminga *et al.*,[44] and what explains these differences? How do ion energies vary as a function of detector angle? What is the relation between the peak kinetic energy of the spectrum and laser intensity? And can hydrodynamics simulations in a computational space with a radius of 10 mm be considered representative for larger distances, as in experimental conditions?

In **Chapter 4**, focus is shifted to a theoretical study of laser absorptivity. The electric field of the laser induces a super-Gaussian electron velocity distribution and decreases the absorptivity of laser light in a plasma (the Langdon effect). In a recent work, Sherlock *et al.* proposed a more accurate method for calculating the Coulomb logarithm in a plasma with a super-Gaussian electron velocity distribution. We apply this theory to a range of plasma conditions, relevant not only to (beyond-)EUV sources but also inertial confinement fusion. We consider which maximum and minimum impact parameters are relevant in these plasmas, and re-derive the absorptivity for those values. The resultant 'Coulomb integral' can be solved analytically, and its leading order has a particularly simple form which can be easily implemented in numerical codes. The sensitivity to laser wavelength and intensity is studied, and we provide several criteria for ensuring accuracy.

Chapter 5 provides additional mathematical groundwork for the laser absorption formula presented in the previous chapter. Solving the Coulomb integral is a nontrivial task, which involves lesser-known mathematical techniques. We provide a step-by-step derivation for a broad family of integrals including (but not limited to) the integrals encountered in laser absorption. For rational values of m (the super-Gaussian exponent), the integral can be expressed in terms of Meijer G-functions; whereas irrational values have no closed form. The integral can be written as a series for any value of m by using the Cahen–Mellin transform of the exponential factor in the integrand, solving the Beta-type integral, and summing over residues of poles in the complex plane. If m is rational, poles may overlap, and a naïve expansion would yield diverging terms; these therefore require a separate treatment. The final result is a general formula that is applicable to any value of m, with any degree of accuracy.

Finally, in **Chapter 6**, the conclusion, I reflect on the larger picture. Now that we have investigated source and emission properties of a 2 µm long pulse, how would one proceed to turn this into a reality? And are there other ways that the Langdon effect can affect laser-produced plasmas?

Chapter 2

Modeling the hundreds-of-nanoseconds-long irradiation of tin droplets with a 2 µm-wavelength laser for future EUV lithography

Stan J. J. de Lange,* Diko J. Hemminga, Yahia Mostafa, Randy A. Meijer, Oscar O. Versolato, and John Sheil.
Plasma Sources Science and Technology **33** 105003 (2024).

The properties of an extreme ultraviolet (EUV) source driven by hundreds-of-nanoseconds-long laser pulses of $\lambda_{laser} = 2$ µm wavelength are investigated through radiation-hydrodynamic simulations. We show that single-pulse irradiation of 30 µm-diameter tin droplets can generate in-band energies $\sim$ 30 mJ directed in the 2π sr solid angle subtended by the collector mirror, yielding energies $\sim$ 100 mJ produced from 45 µm-diameter droplets. Time-integrated in-band EUV emission profiles, generated by taking Abel transforms of the local net in-band emissivity, reveal EUV source sizes in the axial (laser) direction $\times$ radial direction of $\sim$ 600 (1000) $\times$ 100 (150) µm^2 for 30 (45) µm-diameter droplets. We find that approximately 74% of the total in-band emission is produced during the first half of the total propulsion distance irrespective of droplet size or laser intensity. Furthermore, we propose a one-dimensional analytical propulsion model to qualitatively explain the simulated droplet trajectory and to predict the time taken for the droplet to vaporize. These findings offer motivation for the development of high-power EUV sources based on single-pulse, hundreds-of-nanoseconds-long irradiation of tin droplets.

*Contributions to this chapter include designing and performing simulations, analyzing and visualizing the results, and writing and editing the manuscript.

2.1 Introduction

2

Laser-produced plasmas (LPPs) are a compact, versatile means of generating intense, tunable, short-wavelength radiation.[45,46] In addition to facilitating fundamental investigations of atomic structures and plasma properties,[47,48] LPP radiation is utilized in applications spanning biological imaging,[49,50] inertial confinement fusion,[51] and the printing of nanometer-scale patterns on silicon wafers in new-generation semiconductor manufacturing.[52,32,53] This latter application, known as extreme ultraviolet lithography (EUVL), serves as the main motivation for the present work.

The light source incorporated in EUVL machines is that of a hot (electron temperature $T_e \sim 30 - 50$ eV) and dense (electron density $n_e \sim 10^{19}$ cm^{-3}) laser-produced tin plasma.[54,55,56] Under optimum conditions, this plasma produces an intense, narrowband emission feature peaked near a wavelength of 13.5 nm.[57,58,59,26] Crucially, this emission feature overlaps with the wavelengths reflected by Mo/Si multilayer mirrors[33] (13.5 $\pm$ 0.135 nm—the 'in-band' region), mirrors whose purpose is to filter, transport, and shape the in-band radiation for the lithographic process. The first of these mirrors is called the collector mirror. Located in the source vessel, it serves to focus the EUV from the source, and subtends a 2π sr solid angle around the plasma. High-power CO_2 lasers ($\lambda_{laser} = 10.6$ µm) create these plasmas from tin targets that are 'conditioned' by a pre-pulse laser.[60,61] This process ensures maximal absorption of CO_2 laser light, which, in turn, underlies the high in-band EUV powers (P_{inband}) and conversion efficiencies[61] (CE—the ratio of in-band energy radiated in the 2π sr hemisphere in the direction of the collector mirror to laser energy[62]) attained in industrial EUV sources. Industrial sources currently operate at $P_{inband} \sim 250$ W, and efforts to scale this power to $P_{inband} \sim 600$ W (demonstrated in a research setting in Ref. [63]) are ongoing to drive increased wafer throughput.

While CO_2 lasers form the basis of current EUV source design, the research community is now questioning whether a more modern, energy-efficient laser architecture, such as solid-state $\lambda_{laser} \sim 2$ µm Tm:YLF lasers,[64,40] could drive EUV sources of the future. In addition to demonstrating high CE values in EUV source simulations,[65] these systems promise excellent pulse shaping capabilities, scalability to high laser powers and repetition rates, as well as high efficiencies in converting electrical power to laser light (up to $\sim$ 20%[66])—an attractive feature in the drive for a greener semiconductor industry. Laser development has advanced rapidly in recent times, with Tamer *et al.* reporting the development of a 1 GW peak power, 100 J Tm:YLF-based 2 µm system.[66] The goal of the current paper is to investigate, using analytical and numerical means, the properties of EUV source plasmas driven by such advanced laser systems.

Here follows a brief overview of 2 µm-driven EUV source research to date. First experiments on 2 µm-driven tin plasmas, utilizing a master-oscillator power amplifier system, reported conversion efficiencies CE $\sim$ 3% for irradiation of tin slab targets[67]—nearly a factor two higher than the Nd:YAG ($\lambda_{laser} = 1.064$ µm) case, under similar conditions. This was soon followed by a characterization of EUV spectra from spherical[68] and disk-shaped[69] targets. Efforts to increase CE further were made by Mostafa *et al.*,[70] who reported CE $\sim$ 5% using quasi-flat-top spatial and temporal laser profiles.[71] As discussed in that study, it is the flat-top nature of these laser profiles that provides uniform heating of the plasma that drives this CE increase. On the theoretical front, radiation-hydrodynamic modeling has enabled the characterization of laser-to-plasma power partitioning,[72] provided an un-

derstanding of high CE performance,[73,74,72] and has led to the proposal of novel irradiation schemes to drive CE increases.[75] The primary challenge now facing the research community is to identify a 2 µm-driven plasma recipe that can generate EUV powers exceeding those of current industrial systems. The current study will investigate one specific embodiment of such a recipe: irradiating tin droplets with a single, high-energy 2 µm laser pulse until complete droplet vaporization.

In this work, we present the results of laser–plasma simulations of hundreds-of-nanoseconds-long 2 µm-wavelength irradiation of tin droplets. We show that this scheme can generate single-shot in-band energies $E_{inband} \sim 30$ mJ directed towards the collector mirror from irradiation of 30 µm-diameter-droplets. We show that even higher in-band energies $E_{inband} \sim 100$ mJ can be produced from 45 µm-diameter droplet irradiation. A strong stability of instantaneous CE is identified over the course of laser irradiation, as well as a small reduction in CE for laser intensities above the CE-generating optimum. This latter aspect is exploited to generate high in-band energies by using laser intensities above the optimum for CE. The EUV source sizes are quantified by taking Abel transforms of the local net in-band emissivity, revealing extensions in the axial (laser) direction $\times$ radial direction of $\sim$ 600 (1000) $\times$ 100 (150) µm^2 for 30 (45) µm diameter droplets. We find that approximately 74% of the total in-band emission is produced during the first half of the total propulsion distance irrespective of droplet size or laser intensity. A one-dimensional analytical propulsion model has been developed, which, upon inclusion of a droplet size-independent scaling factor, reproduces the time taken to vaporize the droplet as predicted by the simulations.

The structure of the paper is as follows: In section 2.2, we provide details of the radiation-hydrodynamic simulations performed in this work. This is followed in section 2.3 by an extensive characterization of EUV source properties: source size, droplet trajectory dynamics, the dependence of E_{inband} and CE on droplet size and laser intensity, as well as a brief study on the impact of laser refraction on EUV source properties. Finally, the work is concluded in section 2.4.

2.2 Radiation-hydrodynamic simulations

Radiation-hydrodynamic simulations of a single-pulse-on-droplet irradiation scheme were performed using the two-dimensional Radiative Arbitrary Lagrangian–Eulerian Fluid dynamics (`RALEF-2D`) code.[76] Its strength lies in modeling high-temperature, strongly radiating laser-plasmas, finding application in radiation-driven implosion studies,[77] ion-stopping in warm dense matter,[78,79] and EUV source plasma research.[29,34,80,68] A detailed description of the physical models and numerical methods implemented in the code can be found in Refs. [41, 34], and only a brief overview follows.

2.2.1 Code details

`RALEF-2D` solves the equations of single-fluid, single-temperature hydrodynamics including the processes of thermal conduction, radiation transport, and energy deposition through 'external' sources, such as laser heating. The hydrodynamic component of `RALEF-2D` is based on an upgraded version of the `CAVEAT` code,[42] with thermal conduction and radiation transport modules implemented via the symmetric semi-implicit method.[81,82]

The equation of quasi-static, local thermodynamic equilibrium (LTE) radiation transfer, written

$$\hat{\mathbf{\Omega}} \cdot \nabla I_\lambda = \alpha_\lambda (B_\lambda - I_\lambda), \tag{2.1}$$

is solved using the method of short characteristics.[83] Here $\hat{\mathbf{\Omega}}$ is a unit vector representing the photon propagation direction, I_λ is the wavelength (λ)-dependent specific intensity, α_λ is the absorption coefficient and B_λ is Planck's law for blackbody spectral radiance. Absorption coefficients are derived from steady-state non-LTE calculations performed with the `THERMOS` code.[84,29,43] As per the nomenclature of Ref. [85], we will refer to the right-hand-side of Eq. (2.1) as the net emissivity ϵ_λ. The angular dependence of I_λ was modeled using the S_n method[86] with $n = 6$.

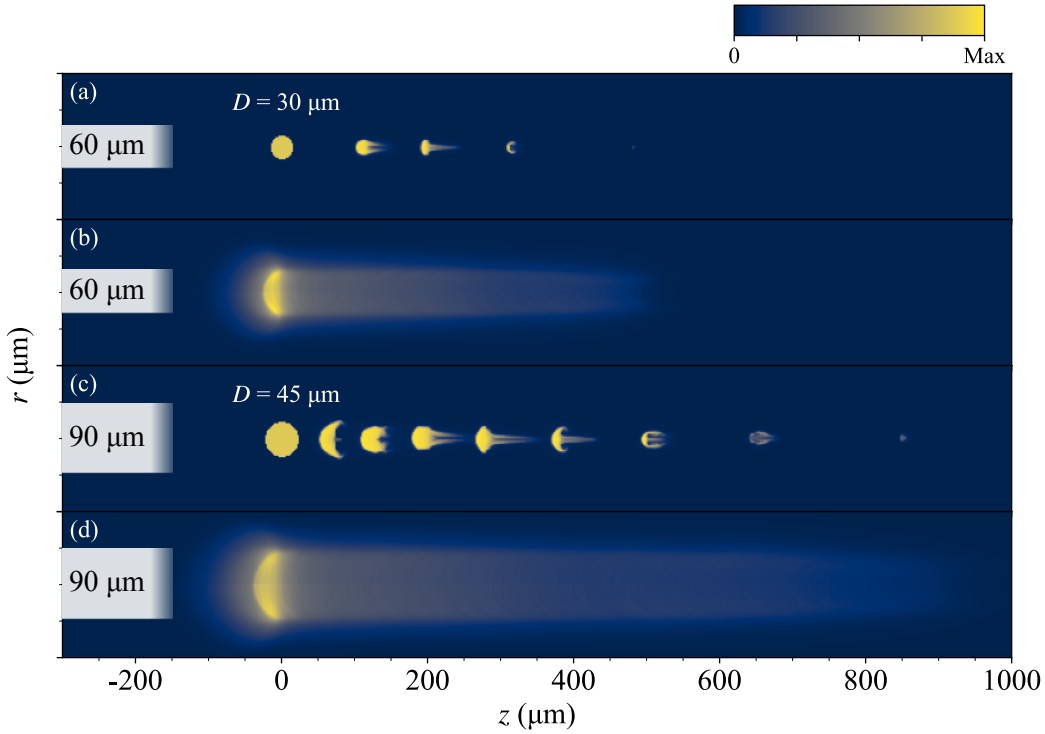


Figure 2.1: (a) Simulated density profile of a $D = 30$ µm-diameter droplet irradiated by a 2 µm-wavelength laser pulse of intensity $I_{laser} = 1.4 \times 10^{11}$ W cm^{-2} at times $t = 0, 75, 100, 125...$ ns after the pulse is switched on. The pulse is incident from $z = -\infty$, and its spatial extent is indicated by the gray-shaded region. (b) Time-integrated in-band image obtained by Abel-transforming positive values of the local net in-band emissivity ϵ_{inband}. Sub-panels (c) and (d) are the same as (a) and (b) but for a 45 µm diameter droplet, and are plotted on a common intensity scale, with $\rho_{max} = 7.7$ g cm^{-3}, and a maximum in-band fluence of 3.2×10^{-3} mJ µm^{-2}.

2.2.2 Target and laser conditions

In the following, we perform two-dimensional axially symmetric simulations of 2 µm irradiation of tin droplets with initial diameters $D = 30$, 40, and 45 µm. The structure of the computational mesh is similar to our previous work;[87] we progressively refine the mesh thickness to a value of ~ 30 nm at the droplet surface. The adaptive Lagrangian–Eulerian

mesh maintains a thickness of $\sim$ 500 nm at the critical electron density surface (similar to that found in Ref. [88]). To ensure homogeneous heating of the plasma over the course of laser irradiation, box-shaped temporal and spatial laser profiles are employed. The temporal duration is chosen to ensure complete vaporization of the droplet target, and the spatial width (following Ref. [72]) is taken to be twice that of the initial droplet diameter over the full course of laser irradiation. As evidenced from Fig. 2.1(b) of Ref. [72], this spatial profile ensures high laser absorptivity due to its significant overlap with the critical electron density surface, *i.e.*, only a very small fraction of incident laser light passes around the target. These choices are further motivated by the recent experiments of Mostafa *et al.*,[70] who demonstrated high CE performance arising from box-shaped laser illumination of tin sheets.

What differentiates the current work from previous theoretical studies on the subject[73,74,72,75] is the present goal of producing industrial-grade, in-band EUV energies (tens of mJ) from a 2 µm-driven plasma. Maximizing in-band production from a main pulse-only scheme requires converting as much of the initial liquid target into in-band emitting ions as possible, which requires full vaporization of the target. Inspired by the findings of Hemminga *et al.*,[72] we investigate the feasibility of using laser intensities above the CE-maximal value ($I_{laser} \sim 0.7 \times 10^{11}$ W cm^{-2} for 2 µm-driven plasmas[62]) to generate high E_{inband} values with minimal impact on CE.

2.3 Analysis of simulations and theoretical modeling

In the following, we characterize the properties of the EUV source: source size, in-band energy E_{inband} production as a function of propulsion distance, instantaneous CE, and mass ablation rate. We also provide a brief study on the impact of laser refraction (in the plasma) on EUV source properties.

2.3.1 Time-integrated in-band profiles

A key parameter in lithography is the étendue of the EUV source. Defined as the area of the EUV-emitting plasma times the solid angle subtended by the collector optics, it characterizes the ability of the collector mirror to focus in-band radiation, and is therefore an important aspect of EUV source design. Its exact value depends on the system's optical specifics, as noted by Fomenkov *et al.*[61]

In Fig. 2.1 we present images of the droplet morphology for laser illumination of tin droplets having diameters (a) $D = 30$ µm and (c) $D = 45$ µm. A laser intensity $I_{laser} = 1.4 \times 10^{11}$ W cm^{-2} is employed in both cases, and the droplet images correspond to times $t = 0, 75, 100, 125, ...$ ns after the pulse is switched on. By conservation of momentum, the droplet is propelled in the $+\hat{z}$-direction as ablated material is ejected primarily in the collector-mirror-directed half-space.[89] The droplet undergoes significant morphological changes throughout laser irradiation. A quantitative study of the droplet trajectory follows in section 2.3.2 below, and we leave the investigation of late-time droplet morphology to future work.

Despite the droplet deformation, the radial size of the EUV source is remarkably constant over time. In Figs. 2.1(b) and (d) we present time-integrated in-band images for the $D = 30$ and 45 µm droplet diameters, respectively. This is done by taking Abel transforms[90] of pos-

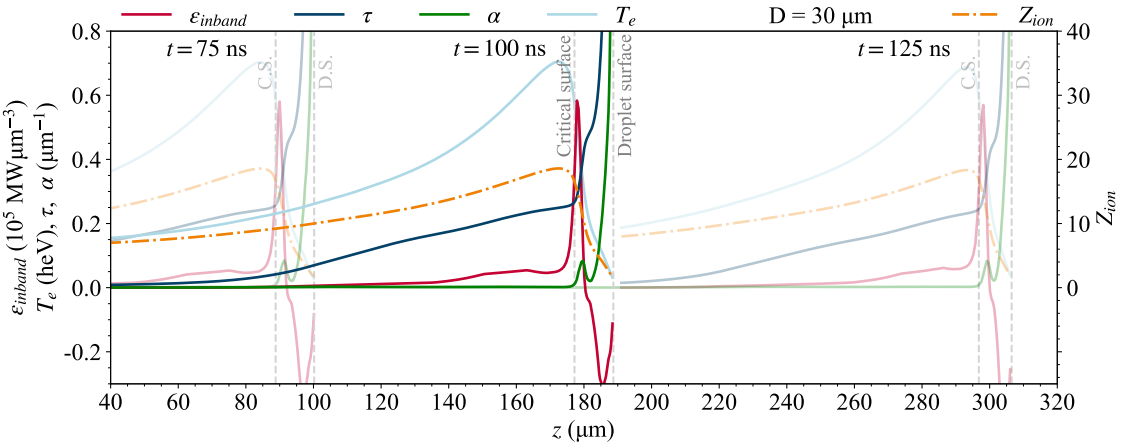


Figure 2.2: One-dimensional profiles taken along the laser axis for $I = 1.4 \times 10^{11}$ W cm^{-2} irradiation of a $D = 30$ µm tin droplet taken at 75, 100, and 125 ns. ϵ_{inband} is the net in-band power per unit of volume, shown in red. The optical thickness $\tau(z)$ (blue), is defined as $\int_z^{-\infty} \alpha(z')dz'$ and α is the absorption coefficient (green). T_e is the electron temperature (light blue), and Z_{ion} is the average charge state (orange dash-dotted curve).

itive values of the local net in-band emissivity ϵ_{inband} at each time, and then summing them up. The quantity shown is therefore an in-band *fluence* (units: mJ µm^{-2}).[72] This transform maps the 2D axially-symmetric in-band emission onto a 2D plane as would be visualized in experiments. It is seen that the radial extent of the source size does not shrink substantially over the course of laser irradiation. The accumulation of high ϵ_{inband} values close to the initial position of the droplet ($z = r = 0$ µm), visible as the bright yellow region, is due to the droplet's inertia: the droplet remains near the origin for a relatively long time, radiating EUV continuously. This bright 'core' of EUV is then followed by a vanishing 'tail' to the right as the target accelerates and decreases in mass. We also observe that very little in-band radiation is produced at distances $z > 600$ (1000) µm for the $D = 30$ (45) µm cases: these positions coincide with the position at which the droplet is fully vaporized, *i.e.*, the position where the maximum density in the target falls below a density of $\rho_{vap} = 1.0$ g cm^{-3}. We will refer to the time at which this occurs as the 'vaporization time' t_{vap}, and the corresponding position as the 'vaporization position' z_{vap}.

These images give a first impression of an EUV source size that could be expected from such an irradiation scheme. The radial extent of the $D = 30$ µm case, $r \sim 100$ µm, is approximately four times smaller than that observed in the experiments of Tomita *et al.* (see Fig. 2.1 (g) of Ref. [54]), who employ a pre-pulse–CO_2 main pulse irradiation scheme starting with a 26 µm-diameter droplet. The z-extent of in-band emission in the 2 µm-driven scheme is on the order of 600 (900) µm for the $D = 30$ (45) µm cases. Tomita *et al.* report a z-extent of ~ 400 µm, comparable to a value of 600 µm value recorded from direct irradiation of 30 µm-diameter droplets. We thus see that our single-pulse irradiation scheme has a smaller EUV emitting area than the multi-pulse industrial scheme characterized in Ref. [54].

The current approach of Abel-transforming ϵ_{inband} neglects the effects of radiation transport and thus assumes an optically thin medium. To study the importance of self-absorption, we plot in Fig. 2.2 the optical thickness τ (blue curves) along the z (laser) axis at times $t = 75, 100$ and 125 ns. This quantity is defined as the line integral of the absorption coefficient

α (green) along the $-z$-axis: $\tau(z) = \int_z^{-\infty} \alpha(z')dz'$. In general, large $\tau(z)$ means that most in-band radiation emitted at z is reabsorbed in the medium, and the plasma is opaque at this depth. You see from Fig. 2.2 that the optical depth rises sharply just behind the critical surface: this is because of the sharp rise in α due to the presence of EUV-absorbing charge states $Z \in [11^+, 15^+]$. A lineout of T_e is shown in light blue, and the orange dash-dotted curve represents the average charge state Z_{ion}; this is a useful heuristic for understanding the emission and absorptive properties of the plasma. In the Thomas–Fermi model,[9,29] Z_{ion} is related to the electron temperature T_e by a power law $Z_{ion} = 1.4T_e^{0.6}$. The maximum T_e at $t = 100$ ns, for example, is $T_e = 71$ eV, giving a maximum average charge state $Z_{ion} \sim 19$: this is above the optimal charge state range for in-band production. (For the $I_{laser} = 0.7 \times 10^{11}$ W cm^{-2} case, the maximum values are $T_e = 49$ eV and $Z_{ion} = 15$.)

We also present in Fig. 2.2 the net in-band emissivity ϵ_{inband} profile (red curve). A few µm behind the critical surface, this quantity peaks. This is due to a coincidental decrease of Z_{ion} to optimal values: here the plasma contains large populations of in-band-emitting charge states, and thus a relatively large fraction of in-band radiation is produced. As one moves closer to the droplet surface, absorption dominates ($\epsilon_{inband} < 0$), and τ rises steeply. If the radiation field is sufficiently intense, this can lead to the formation of a 'radiation-soaked' ablation front,[29] known also as a multiablation structure.[91] We note the local ϵ_{inband} minimum at $z = 168$ µm. This is due to local overheating by the laser, leading to super-optimal Z_{ion} and low in-band EUV emission.[72] For the $I_{laser} = 0.7 \times 10^{11}$ W cm^{-2} case at $t = 50$ ns (not shown), we find that ϵ_{inband} peaks just in front of the critical surface and is more 'extended' in the $-z$ direction compared to the higher-intensity case. This is because the optimal EUV-emitting charge states are bred in a comparatively wider zone. The optical depth at the critical surface in this case is $\tau \sim 0.8$, substantially higher than the higher-intensity case. Lastly, the invariance of the quantities in Fig. 2.2 demonstrates the steady-state nature of the system. A similar figure for the $D = 45$ µm-diameter droplet case is presented in Fig. 2.7 in the Appendix.

At this point it is worth commenting on the optical depth values presented in Fig. 2.2. In the intense EUV-emitting region behind the critical surface, $\tau \sim 0.4$: a rather small value. Use of an Abel transform at late times may therefore be appropriate. However, we should note that the experiments of Schupp *et al.*[68] have, through spectroscopic means, reported a higher value of $\tau \sim 2$. We have a few hypotheses for this difference. Values of τ inferred from experimental spectra were time integrated over short-pulse irradiation ($\sim$ 5 ns) of droplets with $D > 20$ µm. Moreover, the spectra were recorded at an angle of 60° with respect to the laser axis. Values for τ calculated in the present work are (i) instantaneous, (ii) recorded at late times when the plasma size is (most probably) smaller than in the experiments and (iii) taken along the z-axis. In essence, the integral defining the optical depth, $\int_z^{-\infty} \alpha(z')dz'$, is different for experiments and simulation, hence the differences in τ.

As noted above, Fig. 2.1 reveals that the spatial in-band emission is characterized by a core and a tail. In light of the aforementioned discussion on the étendue of the source, we present in Fig. 2.3 a quantitative picture of in-band production as a function of center-of-mass position z for laser intensities $I_{laser} = 0.7, 1.4, 2.1, 2.8$ and 3.5×10^{11} W cm^{-2} (ordered from light to dark blue). The curves reveal how much useful in-band energy E_{inband} is directed into the 2π sr solid angle subtended by the collector mirror within a certain distance from the droplet origin. The curves end where the maximum density in the target falls below ρ_{vap}. The precise value chosen for ρ_{vap} is of little consequence to the results: near

vaporization, the maximum density drops rapidly, and doubling or halving the definition of ρ_{vap} would incur an error of a few ns at most; furthermore, as can be seen from Fig. 2.4(a) below, EUV production ceases shortly after t_{vap}.

Two important observations from Fig. 2.3 are (i) the increase in total E_{inband} yield, *i.e.*, the value at t_{vap}, with increasing laser intensity, and (ii) the clear plateauing of E_{inband} for high laser intensities. Both trends will be further substantiated in the next subsection, where we quantify the instantaneous CE for all cases. Curiously, when center-of-mass position is plotted against E_{inband} relative to their values at t_{vap}, shown in the inset of Fig. 2.3, significant overlap of the curves exists, though there is variation in z_{vap}. Moreover, from the inset one sees that approximately 74% of the total in-band radiation for all laser intensities is generated in the first half of the total propulsion distance. This also extends to the 45 µm-diameter case–see Fig. 2.8 in the Appendix. This finding is important to consider when quantifying the source size and its coupling to the étendue of the system.

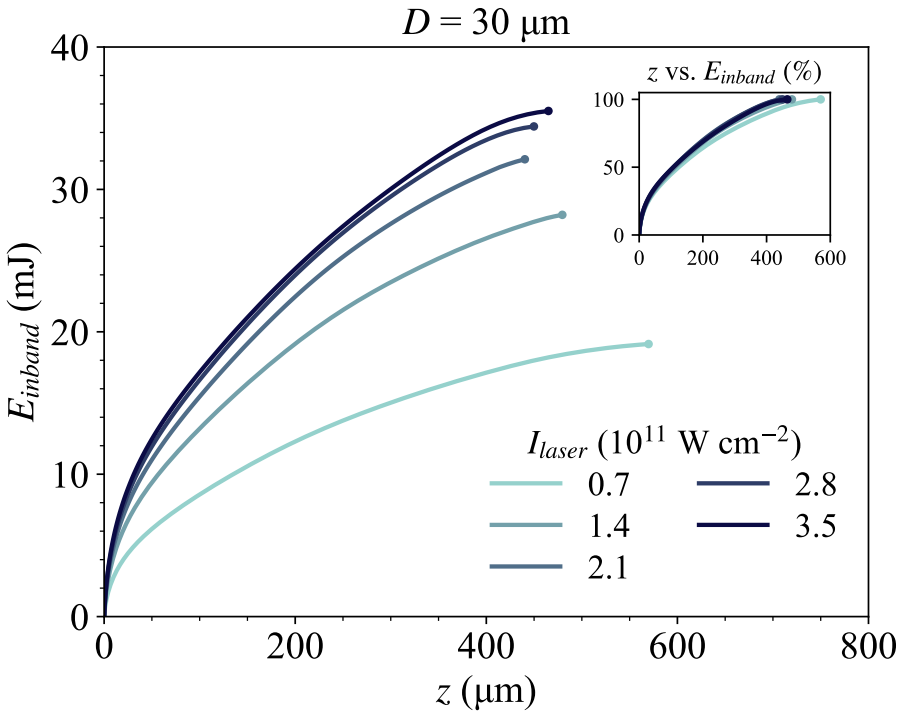


Figure 2.3: Cumulative in-band radiation E_{inband} directed into the 2π sr solid angle subtended by the collector mirror as a function of droplet center-of-mass position z for $D = 30$ µm-diameter droplet irradiation. The curves correspond to laser intensities $I_{laser} = 0.7, 1.4, 2.1, 2.8$, and 3.5×10^{11} W cm^{-2} (ordered from light to dark blue). The inset shows the same curves plotted relative to their respective final E_{inband} values.

2.3.2 Instantaneous conversion efficiency, droplet trajectory dynamics, and mass ablation rate

From the above analysis, three questions arise: How does CE change over time? How does CE depend on laser intensity? How do the droplet trajectory and mass ablation rate depend on time and laser intensity?

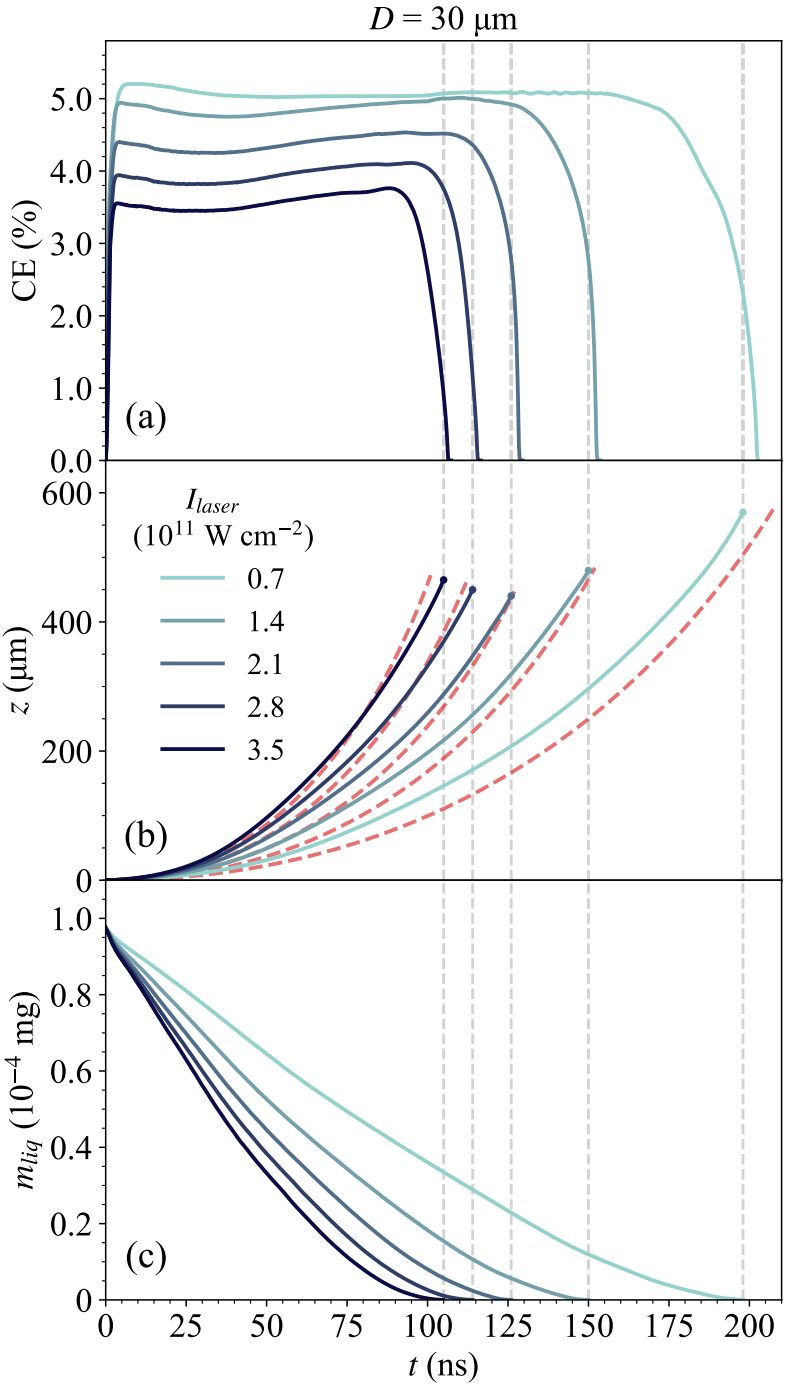


Figure 2.4: (a) Instantaneous conversion efficiency (CE) for $I_{laser} = 0.7, 1.4, 2.1, 2.8$, and 3.5×10^{11} W cm^{-2} irradiation (ordered from light to dark blue) of $D = 30$ μm-diameter droplets. The vaporization time t_{vap} for each case is indicated by the dashed gray vertical line. (b) The center-of-mass position z of the droplet over time. The dashed red curves are the trajectories of the droplet predicted by the theory proposed in this paper. Simulated values for z_{vap} were used as input. (c) The amount of liquid mass (material having density $\rho > 1$ g cm^{-3}) remaining in the target as a function of time.

Addressing the first two questions, we plot in Fig. 2.4(a) the instantaneous CE obtained by irradiating a 30 µm-diameter droplet with laser intensities $I_{laser} = 0.7, 1.4, 2.1, 2.8$, and 3.5×10^{11} W cm^{-2} (ordered from light to dark blue). The dashed gray vertical lines indicate the vaporization time t_{vap}. Values of E_{laser} (laser energy emitted up until t_{vap}), t_{vap}, time-integrated conversion efficiency CE_{int}, and in-band energy E_{inband} emitted in the direction of the collector mirror are provided in Table 2.1 alongside the corresponding laser intensity I_{laser}.

I_{laser} (10^{11} W cm^{-2})	E_{laser} (J)	t_{vap} (ns)	CE_{int} (%)	E_{inband} (mJ)
$D = 30$ µm				
0.7	0.4	198	4.9	19.1
1.4	0.6	150	4.7	28.3
2.1	0.8	126	4.3	32.2
2.8	0.9	114	3.8	34.5
3.5	1.0	105	3.4	35.5
$D = 40$ µm				
0.7	1.1	303	4.6	49.5
1.4	1.5	216	4.4	69.9
2.1	2.0	185	4.0	79.4
2.8	2.4	167	3.5	84.3
3.5	2.7	154	3.1	86.3
$D = 45$ µm				
0.7	1.6	348	4.6	72.1
1.4	2.3	255	4.6	101.2
2.1	2.8	210	4.1	112.0
2.8	3.4	190	3.6	118.9
3.5	3.8	169	3.2	118.7

Table 2.1: Laser parameters and EUV source properties for laser irradiation of 30, 40 and 45 µm-diameter droplets. E_{laser} is the laser energy used up until the vaporization time t_{vap}. CE_{int} is the integrated CE at $t = t_{vap}$. E_{inband} is the total amount of in-band energy directed into the 2π sr solid angle subtended by the collector mirror.

For the lowest, CE-maximizing intensity ($I_{laser} = 0.7 \times 10^{11}$ W cm^{-2}), it takes approximately 10 ns for the plasma to reach a steady-state flow regime, wherein the different energy channels are approximately constant.[72] While the droplet is losing mass, a near-constant instantaneous CE of 5.0% is maintained up until $t = 155$ ns; at this time, the critical surface has retracted to the point that laser light in the periphery of the beam is no longer absorbed. The near-constancy in CE observed in Fig. 2.4(a) is perhaps surprising given the significant morphological changes of the droplet over the course of vaporization, c.f. Fig. 2.1(a). At $t \approx 175$ ns, the droplet contains only 10% of its initial mass and CE begins decreasing rapidly. At $t = 198$ ns, a total of 19.1 mJ of in-band radiation has been emitted in the direction of the collector mirror, with an integrated conversion efficiency of $\mathrm{CE}_{int} \sim 4.9\%$. This is in good agreement with the value $\mathrm{CE}_{int} \sim 4.5\%$ measured in the experiments of Mostafa *et al.*[70]

In Table,2.1, we provide values for the integrated CE at $t = t_{vap}$, CE_{int}, and the cumulative in-band energy E_{inband}. In line with the findings of Hemminga *et al.*,[72] we see that increas-

ing the laser intensity above the CE-maximizing value leads to a substantial gain in E_{inband} and only a minor reduction in CE_{int}. Doubling the intensity to $I_{laser} = 1.4 \times 10^{11}$ W cm^{-2}, for instance, increases E_{inband} by 48% while CE_{int} diminishes by just 0.13%. The difference in in-band production between the two lowest intensity cases (0.7 and 1.4 $\times 10^{11}$ W cm^{-2}) can be understood as the result of a trade-off between laser intensity, t_{vap}, and (to a lesser extent) CE: higher intensities deposit more energy onto the target, but this process occurs for a shorter time (mass ablation rate increases with increasing laser intensity) and causes the CE to depreciate (as the target is heated above CE-optimal temperatures). Increasing the laser intensity further leads to marginal increases in E_{inband} (see Fig. 2.3). That said, the instantaneous CE in all laser intensity cases is remarkably stable for most of the vaporization process. Also provided in Table 2.1 are results from laser irradiation of 40 and 45 µm-diameter droplets. The 2.4-fold and 3.4-fold increase in target mass (compared to the 30 µm diameter case) increase the number of tin ions that contribute to in-band emission.

In Fig. 2.4(b) we show the center-of-mass position z of the target over time and in Fig. 2.4(c) the amount of liquid mass associated with a density $\rho > \rho_{vap}$ remaining in the target over time, which we denote by m_{liq}. Naturally, these curves end at $t = t_{vap}$. While laser-induced droplet propulsion is a complex process, we investigate the observed displacement of the droplet through a simple one-dimensional model akin to rocket propulsion: one starts off with a droplet of tin of mass M, at rest at the origin. The laser ablates the target at a constant rate of $\bar{\mu}$ mg ns^{-1}, with all the ablated material flying off in the negative $\hat{z}$-direction at a laser intensity-dependent rate of $v(I_{laser}, t)$ mm ns^{-1} with respect to the droplet. Imposing momentum and energy conservation, we find the following relation for droplet position (see the Appendix for the derivation):

$$z(t) = v\left(\frac{M - \bar{\mu}t}{\bar{\mu}} \ln\left(\frac{M - \bar{\mu}t}{M}\right) + t\right). \tag{2.2}$$

It is our task to determine $\bar{\mu}$ and v. First consider the mass loss rate $\bar{\mu}$. From Fig. 2.4(c), we see that the mass loss rate $-\mathrm{d}m_{liq}/\mathrm{d}t$ is nearly constant up to $t_{vap}/2$. As such, we can obtain an *empirical* mass loss rate μ by obtaining the (negative) slope of the line from a linear least-squares fit for $m_{liq}(t)$ from 0 up to $t_{vap}/2$. Values for μ for all laser intensity cases are shown by the blue dots in Fig. 2.5. Since trivially μ should tend to 0 for vanishing intensity, a power law appears appropriate to describe its intensity dependence:

$$\mu = A I_{laser}^{B}, \tag{2.3}$$

for some A and B, and with μ in mg ns^{-1} and I_{laser} in W cm^{-2}. A least-squares fit of the data points yields $A = 8.44 \times 10^{-12}$ and $B = 0.45$ in units consistent with μ and I_{laser}, and the result is shown in Fig. 2.5 as the blue dashed curve. Previous studies of tin mass ablation rate also reveal a power-law dependence on intensity; see for example the experimental work of Burdt *et al.*,[92] who, by irradiating planar tin targets with short laser pulses (6.5 ns full width at half maximum) and inferring the crater depth, report an exponent of 0.56, in agreement with the theoretical work of Dahmani and Kerdja.[93] Furthermore, a smaller exponent of 0.29 is predicted in the theoretical study of Basko *et al.*.[29] The value we obtain during the initial phases of droplet evaporation is thus intermediate between these two.

The vaporization time in this model, t_{vap}, is defined as the time at which a mass of $\rho_{vap}V$ remains:

$$t^*_{vap} = \left(1 - \rho_{vap}/\rho\right)\frac{M}{\bar{\mu}} \approx 0.86\frac{M}{\bar{\mu}}. \tag{2.4}$$

Using the values for μ obtained from Eq. (2.3), one obtains the vaporization time t^*_{vap} represented by the dashed green line in Fig. 2.5. This line deviates from the simulated values, represented by the green circles in Fig. 2.5, by a proportionality factor (as the notational difference between μ and $\bar{\mu}$ suggests). This deviation arises because $-dm_{liq}/dt$ abandons constancy and diminishes from $t_{vap}/2$ onwards. Using the above values for μ in the model will therefore under-predict t_{vap}. The correct value for t_{vap} is obtained by using the mean mass loss rate $\bar{\mu}$, defined as $0.86M/t_{vap}$, instead. We find that the mean mass loss rate $\bar{\mu}$ and the 'initial' mass loss rate μ are related by the factor $c = \mu/\bar{\mu}$. With this, the vaporization time can be estimated from the mass loss rate:

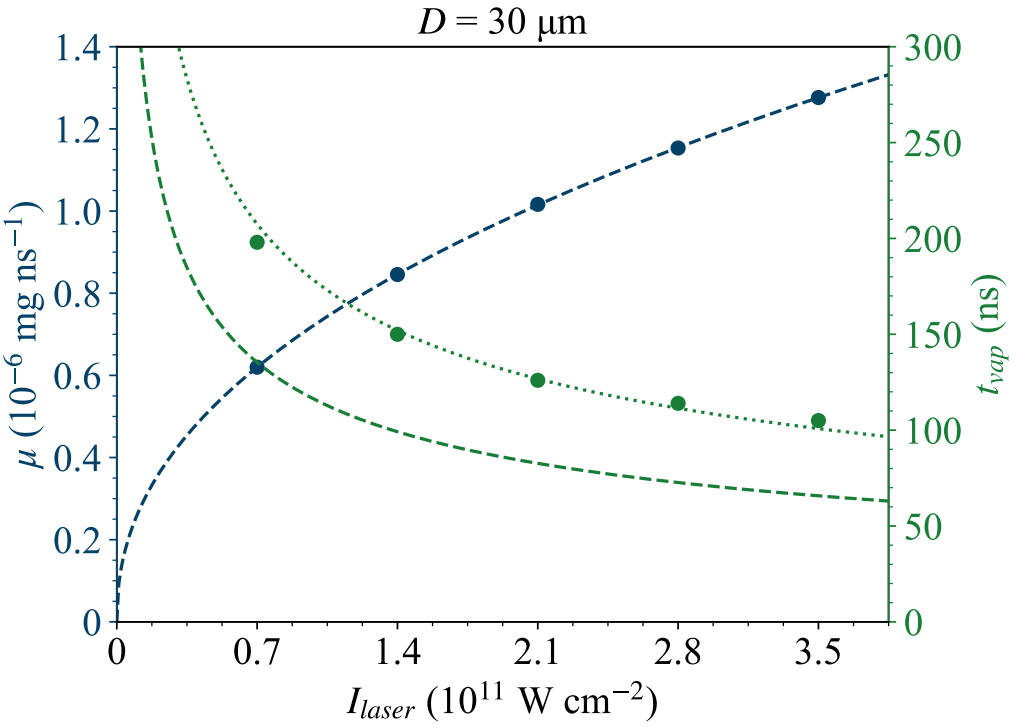


Figure 2.5: The relation between 'initial' mass loss rate μ (blue) and vaporization time (green) with laser intensity. The blue dots correspond to the mass loss rate μ (measured from $t = 0$ to $t_{vap}/2$, see main text) as a function of laser intensity, and the dashed line is Eq. (2.3). The green dashed line is the uncorrected vaporization time t^*_{vap} obtained from Eq. (2.4). By including the correction factor $c = \mu/\bar{\mu} = 1.53$, one finds good agreement between the simulated values for t_{vap} (green dots) and the derived intensity-dependent law for t_{vap}, Eq. (2.5) (dotted line).

$$t_{vap} = 0.86\frac{M}{\bar{\mu}} = 0.86c\frac{M}{AI^B}. \tag{2.5}$$

Taking the average of c over the five data points, we find that $c = 1.53$. This approach has errors no greater than 5% in estimating t_{vap}; for the specific case of $I = 1.4 \times 10^{11}$ W cm^{-2}, the error is less than 2%. The green dotted line in Fig. 2.5 represents Eq. (2.5).

Having found values for $\bar{\mu}$ as a function of laser intensity, we next determine the ablation velocity v. Eq. (2.13) in the Appendix suggests that v is a power law in I_{laser} (since $\bar{\mu}$ is also a power law of I_{laser}). This implies $v \propto I^{(1-B)/2} \approx I^{0.28}$, a rather weak dependence on I_{laser}. However, this does not provide an adequate prediction of the vaporization position z_{vap}: the simulated value does not follow a power law in I_{laser} as would be predicted by Eq. (2.2) and the above-theorized behavior of v. In fact, from Fig. 2.4(b), one sees that the simulated z_{vap} values initially decrease with increasing I_{laser} until $I_{laser} = 2.1 \times 10^{11}$ W cm^{-2}, beyond which z_{vap} increases. Whatever the trend in z_{vap} with increasing laser intensity, its values are highly sensitive to variations in t_{vap} due to the droplet's high velocity near vaporization.

To circumvent these difficulties, we determine v in the following way: We first substitute the expression for t_{vap} into Eq. (2.2) to derive the position z_{vap} at which t_{vap} occurs:

$$\begin{aligned} z_{vap} \equiv z(t_{vap}) &= \frac{Mv}{\bar{\mu}} \left[\frac{\rho_{vap}}{\rho} \ln\left(\frac{\rho_{vap}}{\rho}\right) + \left(1 - \frac{\rho_{vap}}{\rho}\right) \right] \\ &\approx 0.58 \frac{Mv}{\bar{\mu}}. \end{aligned}$$

Second, using values of z_{vap} predicted by the simulations, we solve Eq. (2.6) for v. We now have everything necessary to plot Eq. (2.2), which is shown by the red dashed lines in Fig. 2.4(b) for the various laser intensity cases. For $I_{laser} < 1.4 \times 10^{11}$ W cm^{-2}, the model under-predicts t_{vap}, and for $I_{laser} > 1.4 \times 10^{11}$ W cm^{-2} it over-predicts t_{vap}; this arises from deviations between simulated t_{vap} values (green data points in Fig. 2.5) and the analytic t_{vap} (green dashed line in Fig. 2.5). These things notwithstanding, our relatively simple one-dimensional model is adept at qualitatively explaining the shape of the trajectory curve.

Simulation results for the irradiation of $D = 45$ µm diameter droplets are shown in Figs. 2.8, 2.10 and 2.9 in the Appendix. The shapes are qualitatively similar to that of the $D = 30$ µm case, although z_{vap} and t_{vap} are substantially larger than the $D = 30$ µm case given the 1.5^3-fold increase in mass of the target. The power law Eq. (2.3) is also found to hold true with nearly the same exponent: $B = 0.46$. The laser and EUV source parameters associated with this droplet diameter, as well as an intermediate value of $D = 40$ µm, are also provided in Table,2.1. Importantly, we see that laser irradiation of $D = 45$ µm droplets with $I_{laser} \geq 1.4 \times 10^{11}$ W cm^{-2} can generate $E_{inband} > 100$ mJ.

2.3.3 Laser refraction and EUV source properties

In the simulations presented thus far, only laser absorption and reflection in the plasma were modelled; the effects of laser refraction were ignored. As discussed in Ref. [88], refraction of the laser beam in underdense plasma regions can induce unstable plasma outflows. This can result in the focusing of laser light into regions with a depression in the electron density; this is called hydrodynamic self-focusing instability. Localized regions of high temperatures emerge ('hot spots'—see Fig. 2.6 of Ref. [80]), which, alongside the plasma outflow, fluctuate significantly in both space and time. We now investigate the effect of including laser refraction in our model on EUV source properties.

In Fig. 2.6, we compare the instantaneous CE values for two cases: one that does not consider laser refraction in the plasma ('no refraction'—red curve, seen previously in Fig. 2.4) and one that models laser refraction in the plasma ('refraction'—blue curve). The two cases are initially similar in CE, where the 'refraction' case is seen to oscillate about the 'no refraction' CE value. However, around 75 ns, the CE in the 'refraction' case suddenly drops by approximately 20% before stabilizing; at 125 ns, the CE starts dropping to zero, and the droplet vaporizes at 136 ns. All in all, 23.2 mJ of in-band radiation is emitted in the 2π sr solid angle of the collector mirror, approximately 82% of the 'no refraction' case.

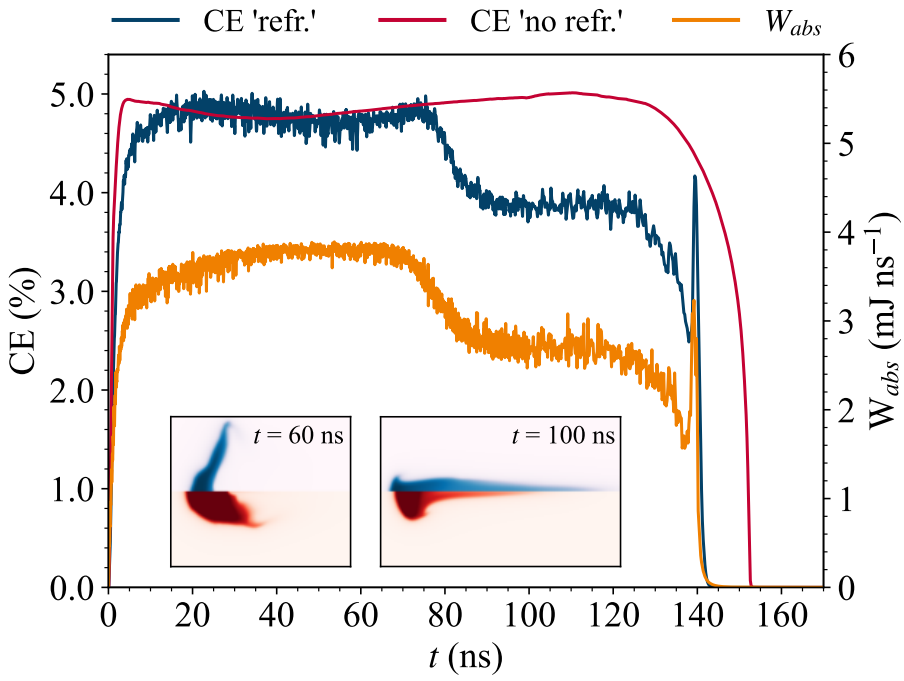


Figure 2.6: A comparison of time-resolved CE of simulations for the 'refraction' case (blue curve) and the 'no refraction' case (red curve). Both cases represent laser irradiation of a 30 µm diameter droplet with $I_{laser} = 1.4 \times 10^{11}$ W cm^{-2}. Absorbed laser energy in the 'refraction' case is shown by the orange curve. The two insets show the density distributions at 60 ns (total image size 60 × 50 µm) and 100 ns (80 × 50 µm). The 'refraction' case is shown in the upper half, the 'no refraction' case in the lower. Note that the upper and lower halves of the insets are aligned for comparison and do not actually match in z-position.

To understand the drop in CE in the 'refraction' case, we present in Fig. 2.6 two insets showing the density profiles of the targets before and after the drop in CE, at 60 and 100 ns respectively. The upper half shows the 'refraction' case (blue) and the bottom half shows the 'no refraction' case (red). Within this interval, the target in the 'refraction' case changes shape from flat to elongated along the z-axis; this reduces its cross section, and consequently, a fraction of the laser light will fail to be absorbed. This is evident from the absorbed laser power curve shown in orange in Fig. 2.6, which closely follows the shape of the CE curve including the drop at 75 ns and the spike at 139 ns. Despite the simulation's inherent stochasticity, the oscillatory trend and subsequent drop in CE are reproduced for repeated simulations using identical laser and target parameters. Therefore, we attribute the discrepancy in CE (between the 'refraction' and 'no-refraction' cases) to the morphological difference of the droplet target between the two cases, and draw attention to the importance of droplet

morphology for long-pulse irradiation schemes.

2.4 Conclusion

In this paper, we have elucidated various aspects of long-pulse, 2 µm-wavelength laser irradiation of tin droplets in the context of EUV sources for nanolithography. The main point is that the usage of large droplets and long pulses is, in theory, able to produce tens of millijoules of in-band radiation. While a laser intensity of 0.7×10^{11} W cm^{-2} has previously been identified as CE-optimal, we find that even greater amounts of in-band-energy-per-shot can be produced by increasing the intensity at minimal loss in CE. Moreover, we have quantified the EUV source size and have shown that $\sim 74\%$ of the in-band energy is emitted within half the total propulsion distance regardless of droplet size or laser intensity.

We presented a simple one-dimensional model to predict the droplet trajectory and vaporization time. By calculating the ablation rate and deriving a scaling law, this model gives accurate and consistent estimations of the vaporization time for the range of laser intensities considered. These findings, coupled with those mentioned above, provide impetus for further development of EUV sources based on single-pulse, 2 µm-wavelength irradiation of tin droplets.

Acknowledgments

We would like to thank Wim van der Zande, Jorge Gonzalez, Elio Champenois, Haining Wang, Adam Higginson, and Michael Purvis for useful discussions. This work has been carried out at the Advanced Research Center for Nanolithography (ARCNL). ARCNL is public–private partnership with founding partners UvA, VU, NWO-I and ASML, and associate partner RUG. This work made use of the Dutch national e-infrastructure with the support of the SURF Cooperative using Grants No. EINF-3119 and EINF-6930.

2.5 Appendix

2.5.1 Derivation of the droplet propulsion model

In the following, we derive a simple model, akin to rocket propulsion, to predict the droplet trajectory dynamics. Consider a droplet of tin of mass M initially at rest at the origin. The laser ablates the target at a constant rate of $\bar{\mu}$ mg ns^{-1}, and all the ablated material moves in the negative $\hat{z}$-direction at a laser intensity and (*a priori*) time-dependent rate of $v(I,t)$ mm ns^{-1} with respect to the droplet. For initial conditions we assume $z(0) = 0$, $V(0) \equiv \dot{z}(0) = 0$. Finally, we require that momentum and energy be conserved. We therefore have two functions with two unknowns. Conservation of momentum (droplet momentum plus the momentum of the debris ablated at every interval in time) can be written as

$$(M - \bar{\mu}t)V(t) = \int_0^t \bar{\mu}(v(I,\tau) - V(\tau))d\tau. \tag{2.6}$$

Taking the derivative on both sides with respect to t,

$$-\bar{\mu}V(t) + (M - \bar{\mu}t)\dot{V}(t) = \bar{\mu}v(I,t) - \bar{\mu}V(t), \tag{2.7}$$
$$(M - \bar{\mu}t)\dot{V}(t) = \bar{\mu}v(I,t). \tag{2.8}$$

Conservation of energy is implemented by positing that the total kinetic energy in the system increases due to the energy supply by the laser:

$$\frac{1}{2}\bar{\mu}(v(I,t) - V(t))^2 + \frac{dE_{k,droplet}}{dt} = \eta_k \sigma I, \tag{2.9}$$

where η_k is the fraction of laser power that is converted into kinetic energy (which is taken as constant) and σ is the cross-section of the (fully absorbed) laser beam. It is assumed that all laser light is absorbed (thus with no light escaping, the laser power is proportional to the intensity). The droplet's kinetic energy is given by

$$E_{k,droplet} = \frac{1}{2}(M - \bar{\mu}t)V(t)^2. \tag{2.10}$$

Substituting this into Eq. (2.9) and reordering terms we obtain:

$$\frac{1}{2}\bar{\mu}v(I,t)^2 - \bar{\mu}v(I,t)V(t) + (M - \bar{\mu}t)V(t)\dot{V}(t) = \eta_k \sigma I. \tag{2.11}$$

From Eq. (2.8) we find that the second and third terms cancel:

$$\frac{1}{2}\bar{\mu}v(I,t)^2 = \eta_k \sigma I. \tag{2.12}$$

And thus we find our expression for v:

$$v(I,t) = \sqrt{2\sigma\eta_k I/\bar{\mu}}. \tag{2.13}$$

Note that this function is constant in time: $v(I,t) = v(I)$. To derive $V(t)$, we go back to Eq. (2.8):

$$\dot{V}(t) = \frac{\bar{\mu}v}{M - \bar{\mu}t}. \tag{2.14}$$

Since v is constant, this integral is straightforward:

$$V(t) = \int_0^t \frac{\bar{\mu}v}{M - \bar{\mu}\tau} d\tau = v \ln\left(\frac{M}{M - \bar{\mu}t}\right). \tag{2.15}$$

Finally, the droplet position $z(t)$ is computed by integrating again:

$$z(t) = \int_0^t V(\tau) d\tau = v\left(\frac{M - \bar{\mu}t}{\bar{\mu}} \ln\left(\frac{M - \bar{\mu}t}{M}\right) + t\right). \tag{2.16}$$

2.5.2 Simulation results for 45 µm diameter droplet

The following four plots, Figs. 2.7, 2.8, 2.9, and 2.10, are identical to Fig. 2.2, 2.3, 2.5, and 2.4 in the main text, but correspond to laser irradiation of a $D = 45$ µm-diameter droplet. The trends shown in these plots are qualitatively very similar to the $D = 30$ µm case, albeit that the values for E_{inband} and z_{vap} and t_{vap} are significantly higher here, given the increased target mass.

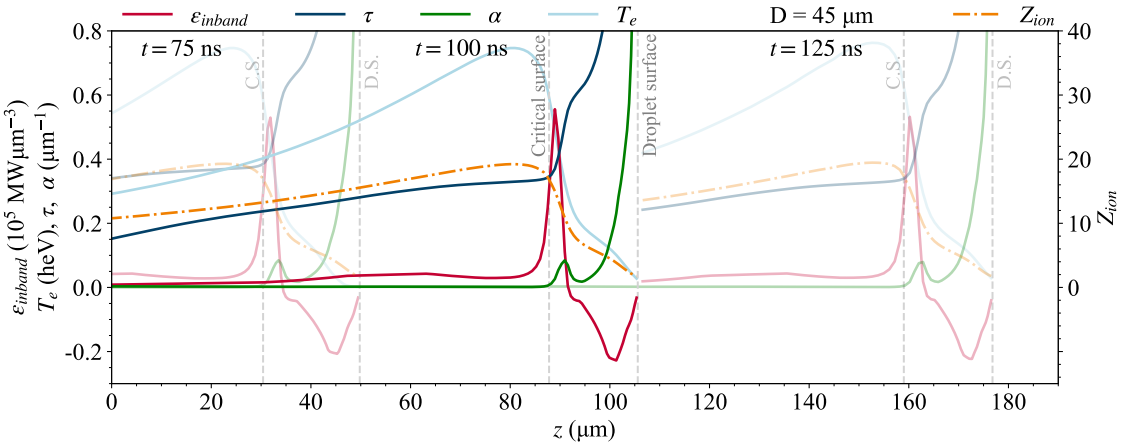


Figure 2.7: Same as Fig. 2.2 for a $D = 45$ µm-diameter droplet.

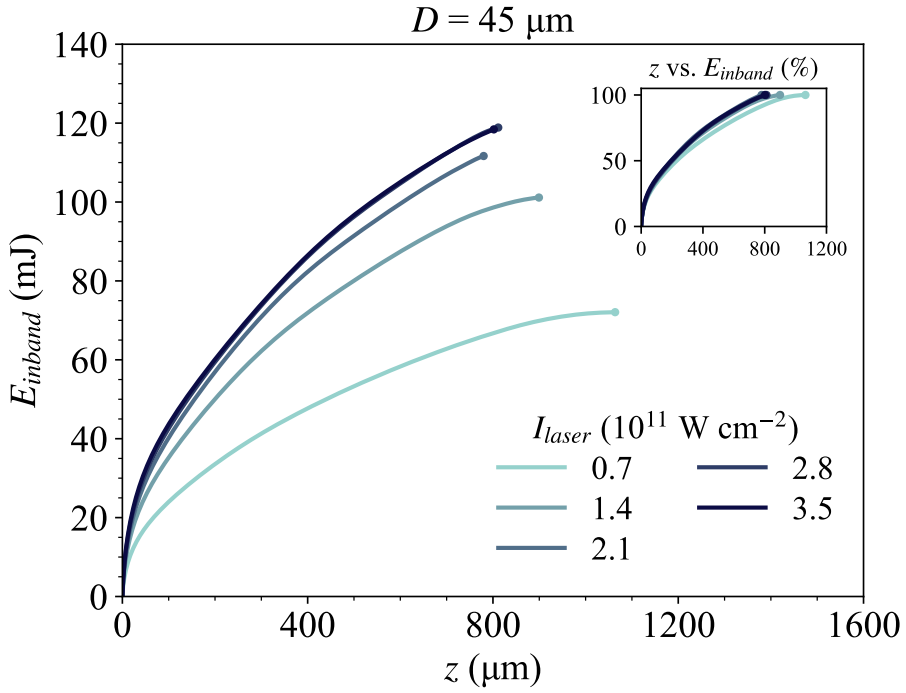


Figure 2.8: Same as Fig. 2.3 for a $D = 45$ µm-diameter droplet.

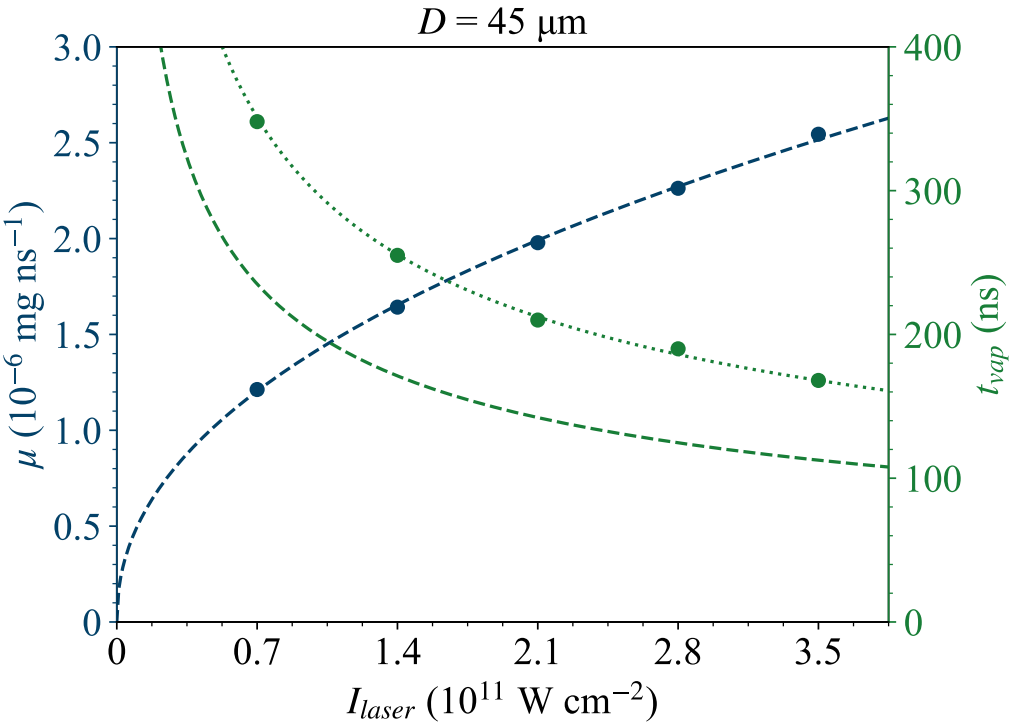


Figure 2.9: Same as Fig. 2.5 for a $D = 45$ µm-diameter droplet. The blue dashed line, Eq. (2.3), has parameter values $A = 1.31 \times 10^{-11}$ and $B = 0.46$, and the dashed green line, Eq. (2.5), uses $c = 1.49$.

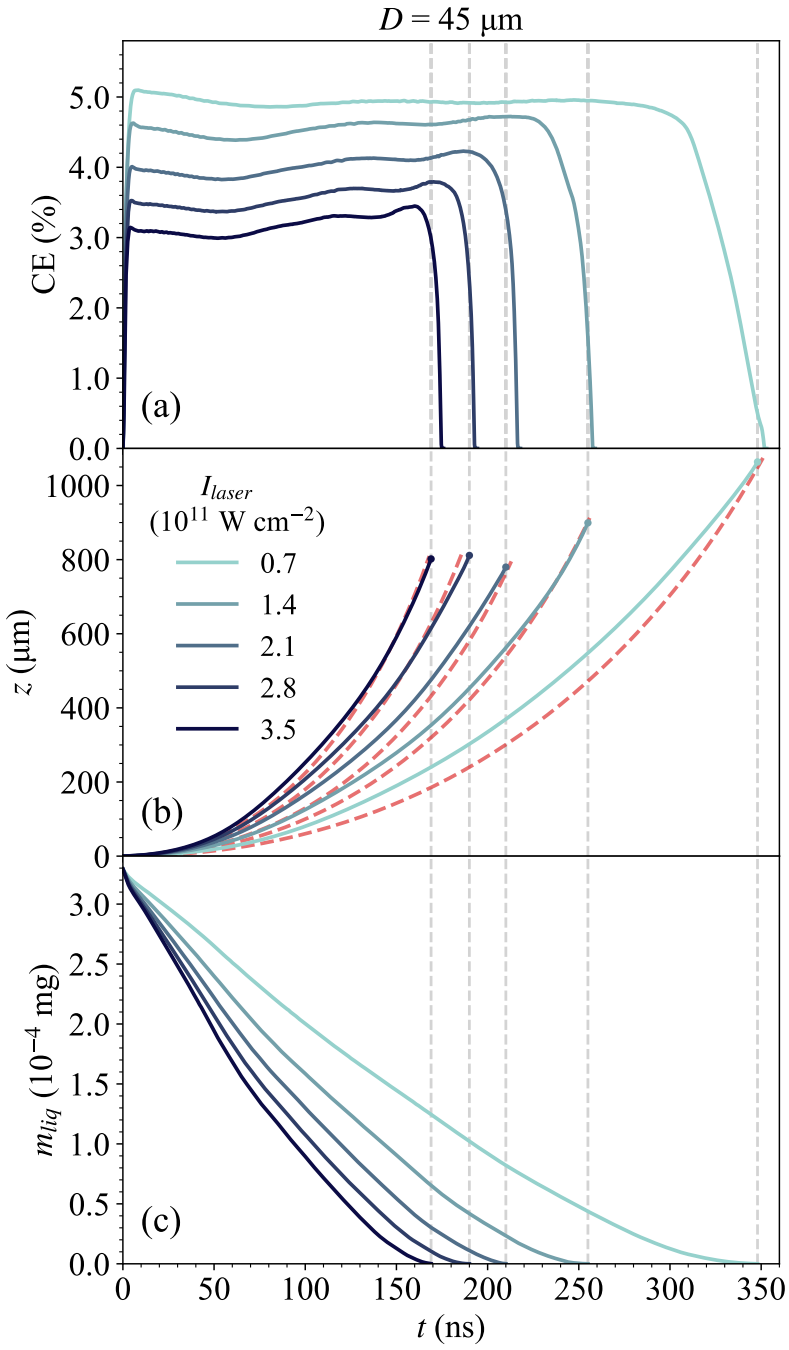


Figure 2.10: Same as Fig. 2.4 for a $D = 45$ µm-diameter droplet.

Chapter 3

Ion emission properties of tin plasmas generated by 2 µm-wavelength laser pulses

Stan J. J. de Lange,* Jorge Gonzalez, Dion J. Engels, Felix M. Kohlmeier, and John Sheil.
Plasma Sources Science and Technology **34** 125013 (2025).

Using radiation-hydrodynamic simulations, we investigate the properties of ion emission from a plasma generated by irradiating tin droplets with $\lambda_{\text{laser}} = 2$ µm-wavelength laser light. Two cases are considered: first a 'short pulse' (27 ns-long) case with laser intensity $I_{\text{laser}} \sim 10^{11}$ W cm^{-2} that can be readily benchmarked with present experimental systems. Then, a 'long pulse' case is studied, in which the droplet is irradiated until it is fully vaporized, which takes $\sim$ 150 ns. The kinetic energy-resolved ion spectra in both cases feature a high-energy peak on the order of keVs. At lower kinetic energies the spectra are substantially different: the short pulse spectrum exhibits much higher ion numbers due to plasma cooling at the end of the pulse, which is not present in the long pulse case. The following quantities of interest are analyzed: angle-dependence of the peak kinetic energy, total kinetic energy, and total ion number, as well as intensity-dependence of the kinetic energy peak. To provide a measure of non-fluid behaviour of the expanding plasma, we calculate the local Knudsen number; though the obtained values are significant, the kinetic energy data are found to be reliable, and can be extrapolated to larger distances.

*Contributions to this chapter include designing and performing simulations, analyzing and visualizing the results, and writing and editing the manuscript.

3.1 Introduction

High-volume industrial manufacturing of integrated circuits relies on extreme ultraviolet (EUV) photolithography.[32] In this process, EUV light is used to print nanometer-scale patterns on silicon wafers. This light is generated by firing laser pulses on tin targets made from microdroplets; the resulting laser-produced plasma (LPP) radiates intensely in the EUV, specifically in a narrow wavelength band peaked near 13.5 nm.[59,53,26] This peak crucially coincides with the $13.5 \pm 1\%$ nm 'in-band' optimal reflectance window of Mo/Si multilayer mirrors,[33] which are used in the nanolithography process to shape and transport the EUV light.

Chosen for its high power, the CO_2 gas laser (laser wavelength $\lambda_{\text{laser}} = 10.6$ µm) has set the current industrial standard for EUV generation.[61] However, recently the use of $\lambda_{\text{laser}} = 2$ µm laser light, such as from Tm:YLF solid-state laser systems, has drawn interest as a potential contender:[64,66] It promises advantages such as higher wall-plug efficiency,**?** improved pulse-shaping capabilities, and scalability to high powers and repetition rates.[65] Both simulations and experiments show that 2 µm-driven plasmas are capable of achieving conversion efficiencies (CEs—the in-band EUV energy, radiated in the laser-facing 2π hemisphere, relative to the laser energy) comparable to CO_2-driven plasmas.[73,74,72,70,94]

Additionally, 2 µm-wavelength solid-state systems have been designed that can generate pulses with near-1 J energy for pulse lengths exceeding 100 ns.[95] Such pulses would enable continuous EUV generation until complete vaporization of the droplet. The use of long pulses circumvents the need to first shape the droplet into a flat disk using a 'prepulse',[87] thus improving per-shot energy, avoiding tin waste from target shaping, and the general challenges associated with tin target shaping. In our previous paper,[94] (Chapter 2) this $\lambda_{\text{laser}} = 2$ µm long pulse irradiation scheme was explored for the first time through radiation-hydrodynamic modeling using the `RALEF-2D` code.[76] In light of practical limits on source étendue,[61] we imaged the shape of the source, quantified EUV output, and studied droplet motion over the course of the ablation process. Whereas a laser intensity $I_{\text{laser}} = 0.7 \times 10^{11}$ W cm^{-2} was previously identified as CE-optimal,[72] a higher intensity $I_{\text{laser}} = 1.4 \times 10^{11}$ W cm^{-2} proved to significantly enhance in-band energy yield with little loss in CE: we found per-shot in-band energies of 28 mJ in the 2π sr solid angle spanned by the collector mirror for long pulse irradiation of 30 µm diameter droplets.

Fast ions leaving the plasma are one of the limiting factors in EUV source design as they can damage or coat EUV optical instruments, thereby irreversibly decreasing efficiency over time.[61] Ion emission has therefore been the subject of numerous studies using both solid and liquid tin targets (see Poirier *et al.*,[89] Brandstätter *et al.*,[96] and references therein). These studies used $\lambda_{\text{laser}} = 1.064$ µm Nd:YAG laser light (with Gaussian pulse lengths $\tau_{\text{laser}} < 24$ ns) to create the plasmas. In addition, debris mitigation schemes have been proposed and implemented with the goal of slowing down and removing ions from the source vessel. Buffer gases[97,98] and/or magnetic fields[99] are often used for this purpose.

As a direct follow-up to the De Lange *et al.*[94] study (Chapter 2), we now investigate the emission of highly energetic ions from a $\lambda_{\text{laser}} = 2$ µm LPP using `RALEF-2D` simulations. Knowledge of the ion kinetic energy distribution is essential for determining the feasibility of a long pulse EUV source, and currently only simulations can provide this. We will first explore a 'short pulse' case ($\tau_{\text{laser}} = 27$ ns) that can be realized, for instance, with an optical parametric oscillator system.[71] We then study a 'long pulse' case ($\tau_{\text{laser}} \sim 150$ ns) which

serves to guide future experiments involving Ho:YAG or Tm:YLF lasers.

The paper is structured as follows: in section 3.2, we describe the setup of the simulations (the parameters used, and how the ion emission is measured). Section 3.3 covers the short pulse simulation. Then, in section 3.4, we consider a long pulse case, where the droplet is irradiated up to complete vaporization. We recount the laser-heating dynamics observed for a temporally Gaussian-shaped pulse,[44] and extend this to long, temporally flat pulses. We present the energy-resolved ion spectrum, the angular variation of ion emission, the total kinetic energy per solid angle, as well as the intensity and angle-dependence of the peak energy. Lastly, we present lineouts of the Knudsen number, and argue that ion data measured at the edge of the mesh ($r_{\text{mesh}} = 10$ mm) can be compared to experimental data recorded at larger radii ~ 1 m.

3.2 Simulation parameters

Simulations are performed using the two-dimensional radiation-hydrodynamics code `RALEF-2D`.[76] Details of the code and its application to $\lambda_{\text{laser}} = 2$ µm-driven plasmas are given in our previous papers.[72,94] The 'short pulse' case consists of the following parameters: the spatial profile is an idealized flat top with 85 µm diameter, while the temporal profile is constant, with $\tau_{\text{laser}} = 27$ ns (full width at half maximum (FWHM) pulse duration) and a 2 ns ramp-up and ramp-down time (black curve in Fig. 3.1). The total energy in the pulse is 155 mJ, or an average intensity of $I_{\text{laser}} = 1.0 \times 10^{11}$ W cm^{-2}. We also employ experimentally relevant temporal profiles[70] in our simulations (orange curves in Fig. 3.1). The bright orange curve represents a 'mean' profile obtained by averaging many experimental laser profiles. The pulse energy is also 155 mJ. The two lighter curves correspond to intensity profiles one standard deviation below and above the mean profile, with pulse energies of 144.5 and 165.5 mJ respectively. This establishes a margin of error on shot intensity that may arise due to experimental beam instabilities. The droplet diameter in all short pulse cases is 40 µm.

The 'long pulse' case is nearly identical to the simulations performed in De Lange *et al.* (2024)[94] (Chapter 2): a tin droplet with diameter 30 µm is irradiated by a laser pulse with intensity $I_{\text{laser}} = 1.4 \times 10^{11}$ W cm^{-2} and diameter 60 µm. This beam is flat in both space and time, and is active for the duration of the simulation ($\tau_{\text{laser}} = 1000$ ns). It is given a 5 ns ramp-up time, as it was found that the discontinuity of an instantaneous flat top profile causes numerical artifacts in the ion energy distribution. To avoid stochastic effects and reduce computational complexity, refraction of laser light is neglected, except for the test case shown in Fig. 3.2(b).

Ion data are collected at the edge of the spherical simulation domain ($r_{\text{mesh}} = 10$ mm). The 'detector' records cumulative energy- and angle-resolved ion numbers in 1° increments at fixed times. In Figs. 3.2 and 3.3, angle-specific data are recorded at 30° and averaged over a range of ±5°.

As the simulation progresses and material is being ablated, the droplet accelerates. The computational mesh is set to slide along with the center of mass, so that the droplet and the high-temperature, EUV-emitting plasma zone at the critical surface remain in the highly resolved mesh region. For the $I_{\text{laser}} = 1.4 \times 10^{11}$ W cm^{-2} case, the droplet vaporizes at $t = t_{\text{vap}} = 157$ ns (we define the vaporization time t_{vap} as the time that the local density

everywhere is below 1 g cm^{-3}).[94] Mesh sliding is disabled at $t = t_{vap}$; in this time, the droplet moves 0.52 mm, which incurs an angular error of no more than 3° with respect to the original detector position.

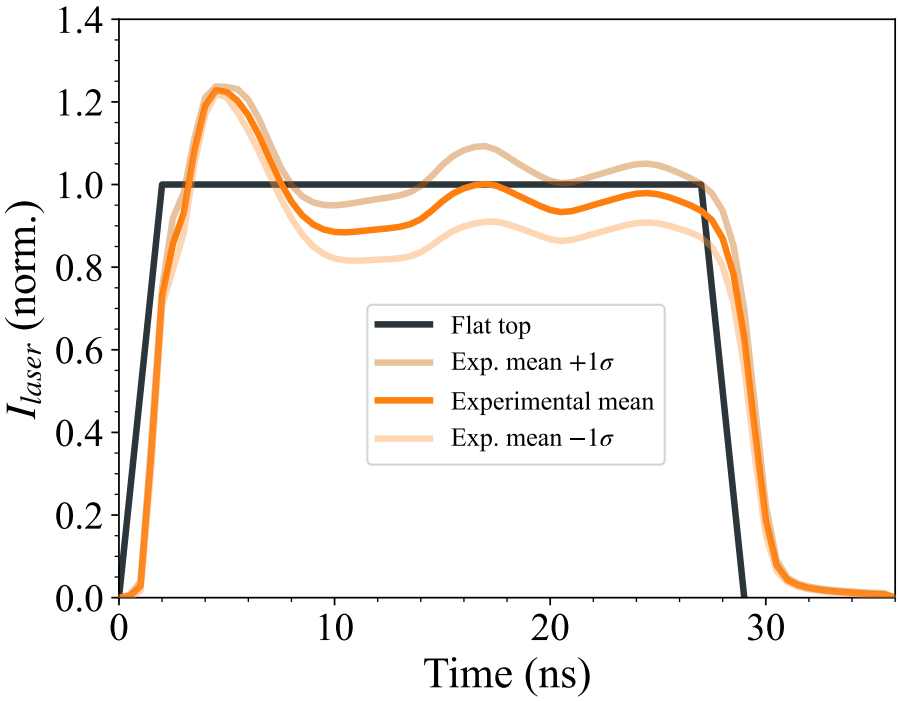


Figure 3.1: Beam profiles used in the simulations. All curves are normalized by the intensity of the flat top profile (black curve). Both the flat top and the mean experimental pulse (orange) have an energy of 155 mJ. The shaded experimental profiles have energies of 165.5 and 144.5 mJ, respectively one standard deviation above and below the mean experimental profile.

3.3 Short pulse simulation

The works of Hemminga *et al.*[44] and Poirier *et al.*[89] have elucidated characteristics of laser-driven ion emission through simulations and experiments. These concerned the irradiation of tin droplets by an Nd:YAG laser ($\lambda_{laser} = 1.064$ µm), with a temporally Gaussian-shaped pulse ($\tau_{FWHM} = 10$ ns), and intensities on the order of 10^{10}–10^{11} W cm^{-2}. They reported absolute ion numbers per kinetic energy per solid angle, $d^2NdE^{-1}d\Omega^{-1}$, as a function of kinetic energy. In their data, they identified a strongly anisotropic ion emission, as well as an energy-resolved peak at ~ 2 keV for a 60 mJ pulse energy case.

With our short pulse case, we aim to provide a benchmark for the long pulse case suitable for comparison with future experiments. The results, shown in Fig. 3.2, represent a normalized (denoted by an asterisk $*$) kinetic energy distribution $d^2N^*dE^{-1}d\Omega^{-1}$. The spectrum generated by the flat top profile is shown in black. Generally, this spectrum resembles the results of Hemminga *et al.*: a peak at 4.1 keV, a sharp drop-off at higher energies, and a tail of low ion numbers at lower energies (< 3 keV).

To understand the features of this spectrum, as well as the long pulse spectrum presented in Fig. 3.3 below, one must consider the ablation dynamics that give rise to it. Hemminga *et*

al. explain that the peak in their ion energy spectrum is formed by two 'bursts' that emerge during the ablation process and interact at late times. Rather, we will argue that this should be thought of as a continuous process.

The Gaussian-shaped pulse employed by Hemminga *et al.* has a temporal profile with $\tau_{\mathrm{FWHM}} = 10$ ns, such that peak intensity is reached at 15 ns. Between 0 and 15 ns, the laser intensity is rising, which gradually increases the plasma temperature, the pressure gradient, and thus the velocity of the emitted ions. Later, higher-energy ions collide with the earlier, lower-energy ions, causing the ions to accumulate. Over time, this accumulation reaches an asymptotic kinetic energy of 2 keV per particle, which forms the peak of the spectrum.

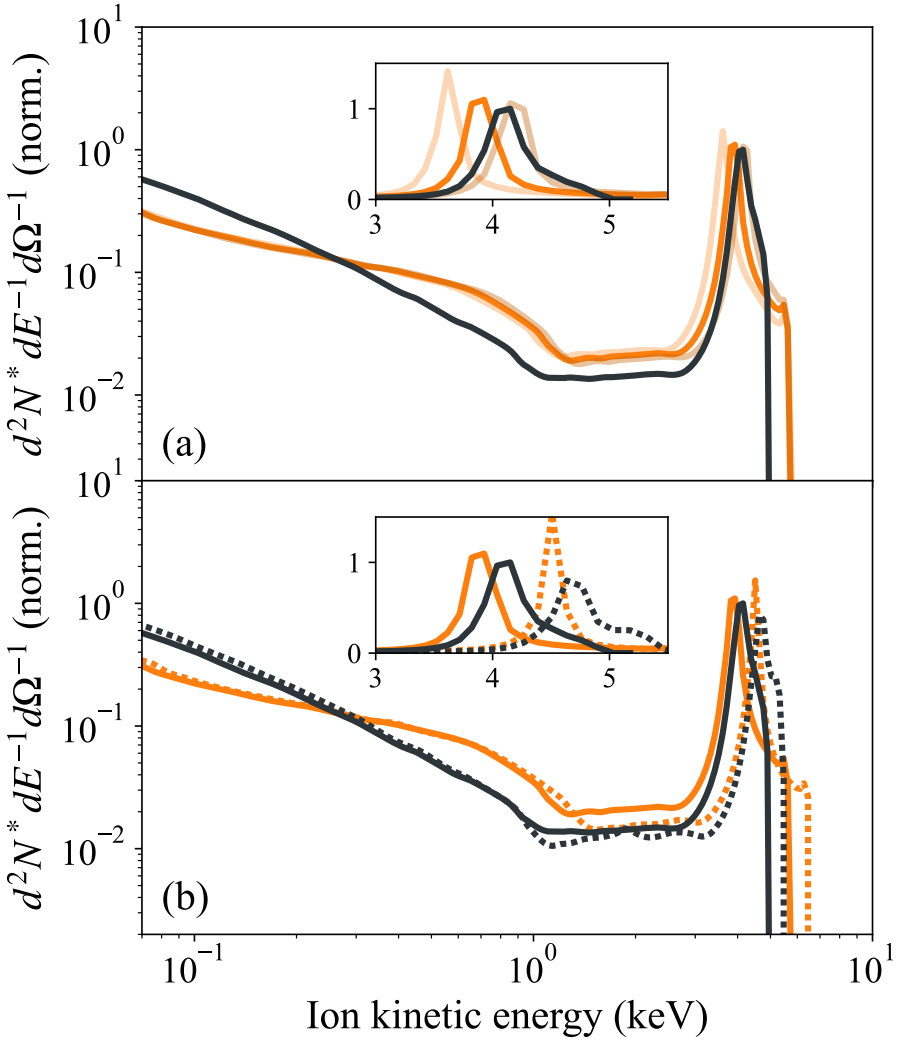


Figure 3.2: The ion kinetic energy spectrum for the short pulse case with $I_{\mathrm{laser}} = 1.0 \times 10^{11}$ W cm^{-2}, measured at an angle of 30°, averaged over ±5°. Black curves represent data using the flat top profile; the peak value of the black curve in (a) is used for normalization of the spectra. Orange curves represent the experimental profiles presented in Fig. 3.1. (a) The two orange transparent curves represent data for the pulse profiles ±1 standard deviation. (b) The dotted curves represent the results for simulations that include the effects of laser light refraction. The insets show the same data with linear–linear axes.

The low-energy tail seen in Fig. 3.2 is produced at the end of the irradiation process: when the laser is turned off, the plasma rapidly cools, and the ions that have not yet reached the critical surface are ablated without being propelled to a high kinetic energy. The subsequent radial expansion leads to an asymptotic $v = d/t$ speed profile.[6,44] Slower ions (kinetic energy < 1 keV) emerge from inner, denser regions of the plasma, and are therefore detected in larger numbers.

We tested the sensitivity of the spectra to variations of a typical temporal beam profile: see Fig. 3.1 and Fig. 3.2(a). The spectrum from the average experimental profile is similar in shape to the flat top case, but the peak is shifted to lower energies by about 0.2 eV; this is due to the lower steady-state intensity at $t > 6$ ns. The two lighter curves, representing intensity data one standard deviation above and below the mean, have a shape similar to the mean experimental profile, with the peak kinetic energy increasing with laser energy.

Furthermore, we considered the effect of refraction for the flat top and the experimental mean profile (dotted curves in Fig. 3.2(b)). Refraction effects cause highly localized, rapidly fluctuating hot spots, and create hydrodynamic self-focusing instabilities.[88] As seen in our previous paper (Chapter 2), the inclusion of refraction leads to notable changes in droplet morphology and in-band EUV production.[94] Fig. 3.2(b) shows that both 'refraction' cases predict the peak to be 0.5 keV higher than the respective 'no refraction' cases. This is because the self-focusing instabilities increase the plasma hot spot temperature.[80]

3.4 Long pulse simulation

3.4.1 Energy-resolved ion spectrum

Fig. 3.3 shows the energy-resolved ion numbers for the long pulse case. Virtually all ions are detected in a peak around 5.3 keV. The evolution of the peak over time is shown in the inset. The lowest curve, shown in green, represents the spectrum at $t = 110$ ns after the activation of the laser: this is approximately the time of flight for the ions to reach the detector. The other curves (orange, cyan, purple, red, and black) represent spectra at 140, 170, 200, 230, and lastly 260 ns: the arrival time of the last high-energy ions. The width of the peak is caused by emission anisotropy over the 10° width of the detector and non-steady state effects. That is, ion flow varies over time and ions of different velocities are sweeping over the detector, resulting in a widening of the peak.

The inset also provides a visual comparison between ion numbers of the long pulse (black) and short pulse (gray) case. The total ion emissions per solid angle $dNd\Omega^{-1}$ is given by the area under the curve. In this plot it becomes clear that, despite the large discrepancy between the two curves at $E < 3$ keV, these low-energy ions are in fact a negligible contribution to the total $dNd\Omega^{-1}$. Virtually all ions are found in the peaks, and the long pulse has produced more ions, as expected.

We will now compare the spectra of the two cases and discuss their physical origin. For both the short and long pulse case, the size of the peak depends on the amount of ablated tin. Longer pulses are able to ablate more material and therefore produce a larger ion peak. Intensity differences notwithstanding, one can think of these spectra as lying on a continuum of laser pulse durations: Hemminga's case is located on the low end (10 ns), the long pulse case on the high extreme ($t_{\mathrm{vap}} = 157$ ns), and the short pulse case is located in-between (27 ns). The pulses considered in this study are longer and have a constant intensity, sustaining

a hot plasma for a longer time than the Gaussian case. This leads to a steady-state outflux of constant kinetic energy by which a narrow peak grows over time, until either the laser pulse stops, or the droplet is vaporized.

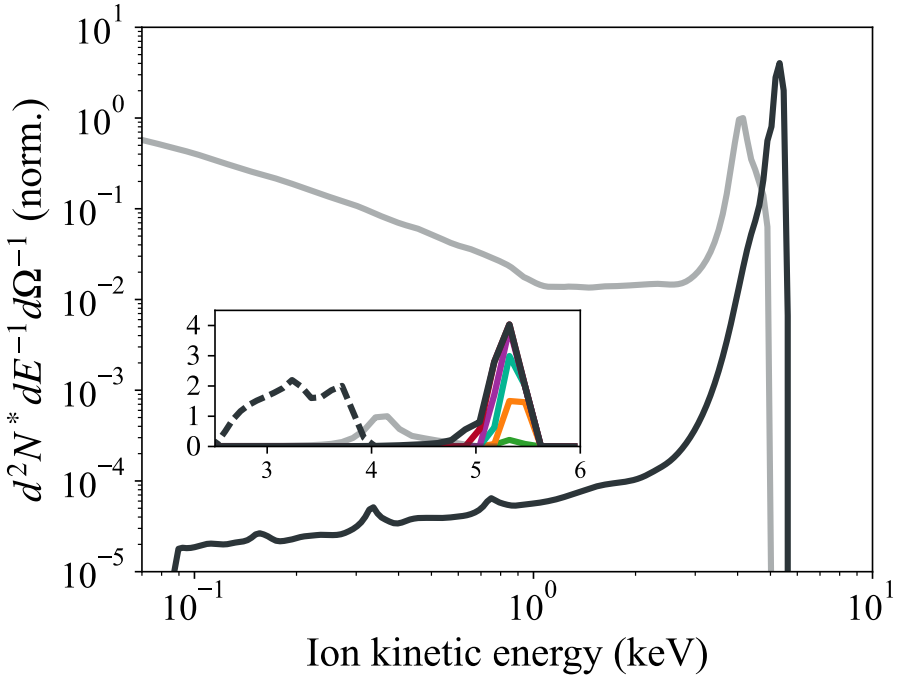


Figure 3.3: The ion kinetic energy spectrum for a long pulse with $I_{\text{laser}} = 1.4 \times 10^{11}$ W cm^{-2} recorded at an angle of $30 \pm 5°$. The inset shows the ion peak with linear axes; the coloured curves represent the spectrum recorded at different times: the green curve is the cumulative spectrum recorded at 110 ns, followed by increments of 30 ns, up to 260 ns (black). The dashed curve (only in the inset) is the ion kinetic energy spectrum measured at 78°. The light gray curve is the flat top case shown in Fig. 3.2, and is used to normalize all data in this plot.

Once the droplet has been fully vaporized, lower-energy (< 4.8 keV) ions are detected in relatively small numbers. This is quantitatively different from the short pulse cases discussed in the previous section: $100\times$ fewer ions are emitted at 2 keV for the long pulse case, and this ratio only increases for lower kinetic energies. This difference arises because, in the long pulse case, the droplet is fully vaporized: the low-pressure expansion seen in the short pulse case (which is made up of the sub-peak energy ions) is thus absent.

To visualize the hydrodynamic transition from ablation to post-ablation, we have plotted in Fig. 3.4 the ion velocity and ion number density for the short pulse and long pulse cases at 23 ns and 33 ns post-ablation, respectively. In the short pulse case, ions are emitted at a high density for as long as the laser is on. When the laser is turned off, the ion density falls; due to the temperature drop, this is paired with a decrease in ion speed, and thus in kinetic energy. As such, the ions contributing to the peak can be distinguished from those in the low-energy tail. Furthermore, since the droplet is not fully vaporized, a liquid remnant is left behind.

In the long pulse case, the laser has fully vaporized the droplet, forming a very low-density region. A decrease in velocity in this region (compared to earlier times) is also observed. During ablation, the velocity is remarkably constant along radial lineouts, which forms the

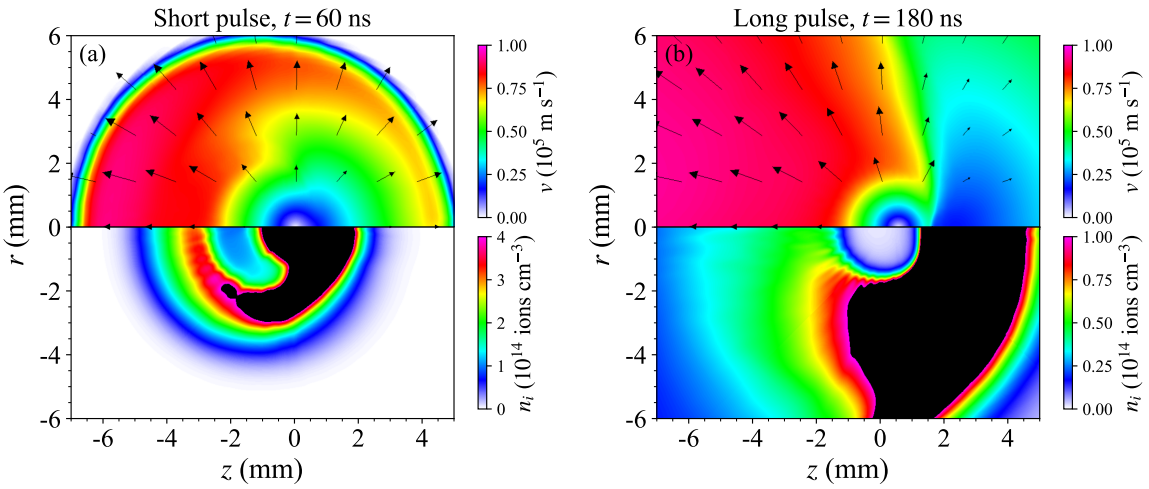


Figure 3.4: 2D colour plots of the tin plasma for (a) short pulse case at $t = 60$ ns; 33 ns after the laser has been turned off, and (b) long pulse case at $t = 180$ ns; 23 ns after the droplet has been vaporized. The top half shows particle velocity, with the arrows indicating the magnitude and direction of the flow velocity. The bottom half shows ion number density. Densities in black exceed the scale maximum.

well-defined ion peak. We note that the densities appear low relative to the short pulse case, for two reasons: i) the long pulse case uses a smaller droplet, leading to less ablated mass per unit of time, and ii) ablation causes the droplet to shrink over time, leading to diminished ablation at late times.

Lastly, we briefly comment on the effect of changing the laser wavelength. Restricting the discussion to laser-on-droplet scenarios, Basko, Novikov, and Grushin have shown that for short wavelength lasers (*e.g.* $\lambda_{\text{laser}} = 1$, 2 µm), absorption occurs over an extended region in the underdense corona.[29] Conversely, for long wavelength lasers (such as 10.6 µm CO_2 lasers), laser absorption is confined to a narrow region in front of the critical surface. This is because the Kramers absorptivity of laser light scales with the wavelength squared; *i.e.*, large wavelengths have a large absorptivity, and therefore a short absorption distance. This results in a higher hot spot temperature for long-wavelength lasers compared to short-wavelength lasers (for the same intensity), and therefore a higher ion kinetic energy. Additional `RALEF-2D` simulations that we have performed confirm this hypothesis.

3.4.2 Angle-resolved ion spectrum

Having presented the ion spectrum for the long pulse case at one specific angle, we now consider general angular behaviour. Three relevant quantities are shown in Fig. 3.5 for angles α in the range 0–90°, comprising the angular span of a collector mirror. Firstly, the solid black curve shows $E_{\text{peak}}(\alpha)$, the energy corresponding to the peak of the ion spectrum, which is given as a discrete set of values due to the code's energy binning method. It is maximal for $\alpha < 20°$ ($E_{\text{peak}} = 5.7$ keV) and gradually decreases for larger angles. For angles up to 60°, the ion spectrum has a single peak. Spectra taken at angles larger than 60° exhibit the formation of a second, lower-energy peak; this slower-moving secondary tin outflux arises due to expansion from a highly-deformed droplet at late times.[94] For angles $\alpha > 70°$, the lower-energy peak grows taller than the higher-energy peak, resulting

in the discrete drop in E_{peak} seen in Fig. 3.5. This double peak can be seen in the inset of Fig. 3.3: the dashed curve represents the spectrum taken at $\alpha = 78°$, where this effect is most pronounced. Beyond 70°, E_{peak} values decrease monotonically.

The red curve in Fig. 3.5 represents the normalized ion number per solid angle, $dN^* d\Omega^{-1}$, which is obtained from the particle flux $j = m_{\text{Sn}}^{-1} \rho v$, where m_{Sn} is the average mass of a tin atom (118.7 atomic mass units), ρ is the mass density of the plasma and v is its speed. The mesh edge is a spherical surface dA that can be expressed as a solid angle: $dA = r_{\text{mesh}}^2 d\Omega$. The angular ion distribution is then obtained by integrating over 1 ns intervals:

$$\frac{dN}{d\Omega} = \int m_{\text{Sn}}^{-1} \rho v r_{\text{mesh}}^2 dt. \tag{3.1}$$

This quantity is nearly constant up to 65°, indicating near-isotropic ion emission. The secondary tin outflux can be observed for angles $\alpha > 65°$, at which point ion numbers start to increase, breaking the nearly-isotropic trend. We show in blue the normalized total ion kinetic energy per solid angle $dE^* d\Omega^{-1}$, likewise defined:

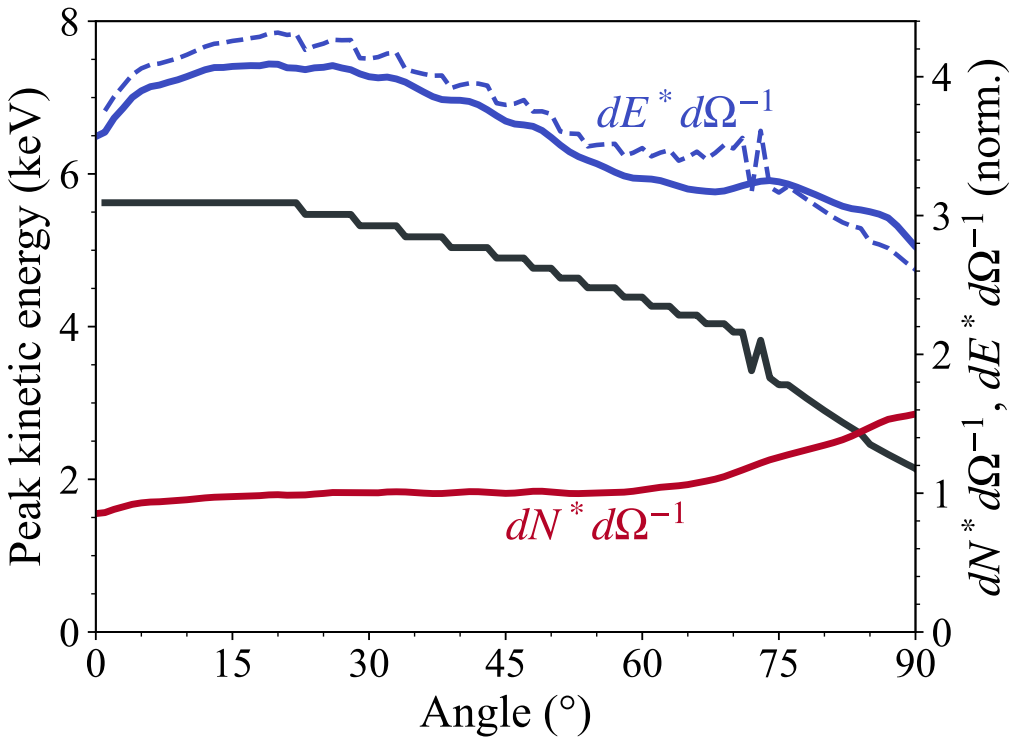


Figure 3.5: Angular data for a long pulse with $I_{\text{laser}} = 1.4 \times 10^{11}$ W cm^{-2}: The peak kinetic energy E_{peak} (black, left axis), the angular ion number emission $dN^* d\Omega^{-1}$ (red, right axis), and the angular kinetic energy emission $dE^* d\Omega^{-1}$ (blue, right axis). The latter quantities are normalized with respect to the values at 30°, and for legibility are normalized to 1 and 4, respectively. The dashed blue curve is the product of E_{peak} and $dN d\Omega^{-1}$.

$$\frac{dE}{d\Omega} = \int \frac{1}{2} \rho v^3 r_{\text{mesh}}^2 dt, \tag{3.2}$$

with the asterisk again indicating normalization. $dE^*d\Omega^{-1}$ is largest for angles $\alpha \sim 25°$, which is also observed in the work of Poirier *et al.*[89] Due to the sharply peaked nature of the ion spectrum, the total energy per solid angle can be estimated from $dNd\Omega^{-1}$ and E_{peak}:

$$\frac{dE}{d\Omega}(\alpha) \approx E_{\text{peak}}(\alpha)\frac{dN}{d\Omega}(\alpha). \tag{3.3}$$

This yields the dashed blue curve. It follows $dE^*d\Omega^{-1}$ with an overestimation of a few percent, and a notable divergence at 60°. As explained above, this is the angle whereat a second peak in the spectrum emerges, invalidating the assumption of a sharply peaked spectrum in this range. The features of the $dE^*d\Omega^{-1}$ curve can thus be explained as the combined effects of increases in $dN^*d\Omega^{-1}$ and decreases in E_{peak} with increasing angle.

Next, we consider the effect of laser intensity on the ion energy spectrum. Laser intensity has a strong influence on the position of the energy peak, as demonstrated by Poirier *et al.* in an experimental setting ($\lambda_{\text{laser}} = 1.064$ µm, $\tau_{\text{FWHM}} = 10$ ns).[100] Fig. 3.6 shows the peak energy as a function of laser intensity for angles 15°–75°. The relationship between these two quantities can be fit to a power law, whose prefactors and exponents are given in the plot legend.

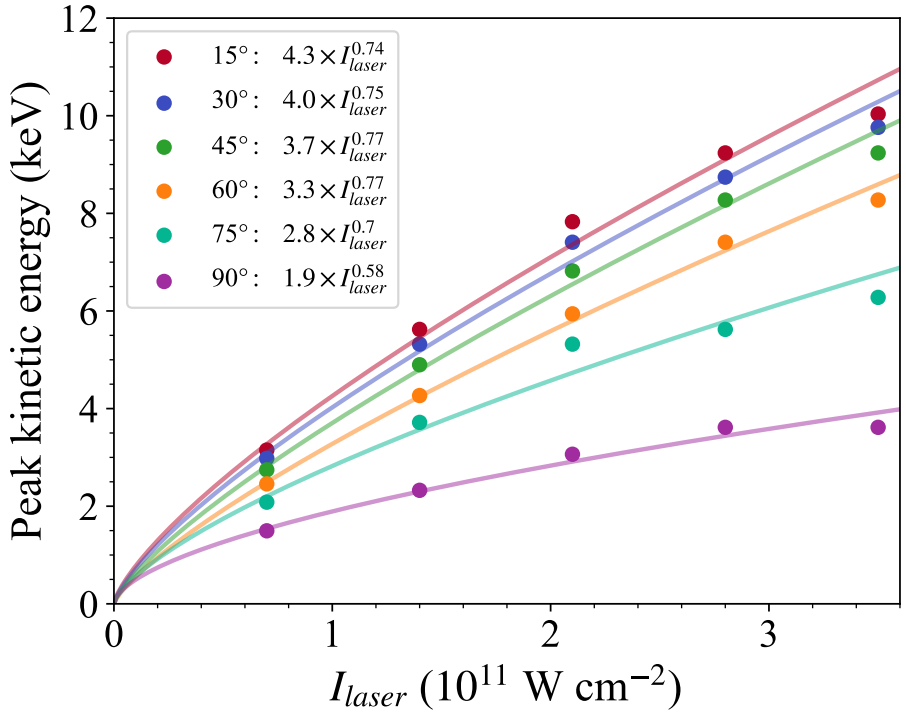


Figure 3.6: Peak kinetic energy as a function of laser intensity ($I_{\text{laser}} = 0.7, 1.4, 2.1, 2.8, 3.5\times10^{11}$ W cm^{-2} for 6 different detector angles. A power law fit to the data is obtained through the least-squares method, with the formula for each curve given in the legend.

For angles 15°–60°, the power law exponent lies between 0.74 and 0.77. Angles 75° and 90° are given for completeness, but it must be noted that these data feature the aforementioned

peak shift due to the slower-moving secondary tin outflux. For the 75° case, the lower-energy peak is dominant for $I_{\text{laser}} = 2.8\text{–}3.5 \times 10^{11}$ W cm^{-2}, but not for $0.7\text{–}2.1 \times 10^{11}$ W cm^{-2}. For the 90° case, the lower-energy peak dominates at all energies. This peak shift is the reason why the exponent for this angle is significantly smaller than the 15°–60° cases.

The obtained exponents can be understood from power law relations, as was shown in Poirier *et al.* Their derivation is repeated here. The bulk kinetic energy of an ablated plasma scales with the plasma temperature T and average charge state $\bar{z}$ according to:[101]

$$E_{\text{kin}} \propto \bar{z}T. \tag{3.4}$$

The average charge state can be approximated by a power law in temperature based on the Thomas–Fermi model;[9] for tin specifically,[29] $\bar{z} \propto T^{0.6}$. Using the scaling relation for electron temperature $T_e \propto I_{\text{laser}}^{0.44}$ (Basko *et al.*[29]), or $T_e \propto I_{\text{laser}}^{0.5}$ (Kawasaki *et al.*[102,103]), one obtains a power law dependence of kinetic energy on laser intensity as

$$E_{\text{kin}} \propto I_{\text{laser}}^{0.70(0.80)}, \tag{3.5}$$

according to Basko (Kawasaki), which agrees with our numerically derived results.

3.4.3 Knudsen number

Lastly we investigate the validity of the fluid dynamics framework in our simulation, and whether the ion kinetic energies at distances beyond $r_{\text{mesh}} = 10$ mm can be inferred. The 10 mm mesh radius was chosen to minimize angular error in the detection of ions over the course of the droplet's 0.5 mm displacement. However, at such distances from the origin, the ion density n_i may become too low to properly treat the plasma as a fluid. The fluid dynamics approach requires that the mean free path length λ_{mfp} be small compared to the characteristic hydrodynamic length scale:

$$\frac{\lambda_{\text{mfp}}}{n_i/|\nabla n_i|} \equiv \text{Kn}. \tag{3.6}$$

This ratio is known as the Knudsen number, Kn; it quantifies whether a gas behaves as a continuum ($\text{Kn} < 0.01$) or as free molecules ($\text{Kn} > 1$).[104] We obtain the mean free path length from the electron–ion interaction time, as electron–ion collisions are the main mechanism of plasma interaction:[105]

$$\tau_{ei} = \frac{6\sqrt{2}\pi^{3/2}\epsilon_0^2\sqrt{m_e}(k_B T_e)^{3/2}}{\ln\Lambda e^4 \bar{z}^2 n_i}. \tag{3.7}$$

Here ϵ_0 is the vacuum permittivity, m_e is the electron mass, T_e is the electron temperature, e is the elementary charge, and $\bar{z}$ is the average ion charge state. $\ln\Lambda$ is the Coulomb logarithm as used in `RALEF-2D`, whose definition follows Spitzer:[20]

$$\Lambda = 3.369\frac{k_B T_e}{e^2}\lambda_D \left(\frac{\bar{z}^2}{(4\pi\epsilon_0)^2} + 0.945847\frac{\hbar^2 k_B T_e}{m_e e^4} \right)^{-1/2}. \tag{3.8}$$

In this equation, $\hbar$ is the reduced Planck constant and λ_D is the combined Debye length for electrons and ions, assuming the ion temperature and the electron temperature are equal ($T_i = T_e$):

$$\lambda_D = \sqrt{\frac{\epsilon_0 k_B T_e}{\bar{z}(\bar{z}+1) n_i e^2}}. \tag{3.9}$$

It follows that $\lambda_{\text{mfp}} = v_{\text{th}}\tau_{ei}$, where v_{th} is the local thermal electron velocity given by $v_{\text{th}} = (3k_B T_e/m_e)^{1/2}$. With these relations, the Knudsen number can be calculated from local `RALEF-2D` data. Fig. 3.7 shows lineouts of the Knudsen number taken at $t = 140$ ns, for $\alpha = 0°$, 30°, and 60°. At this time, ions have reached the mesh edge and the droplet is still being ablated. As the plasma expands into the vacuum, it reaches values for Kn on the order of 0.1 within $r = 0.5$ mm. This lies between the two Knudsen number regimes mentioned above (continuum and free molecules). The Knudsen number generally increases with increasing radial distance.

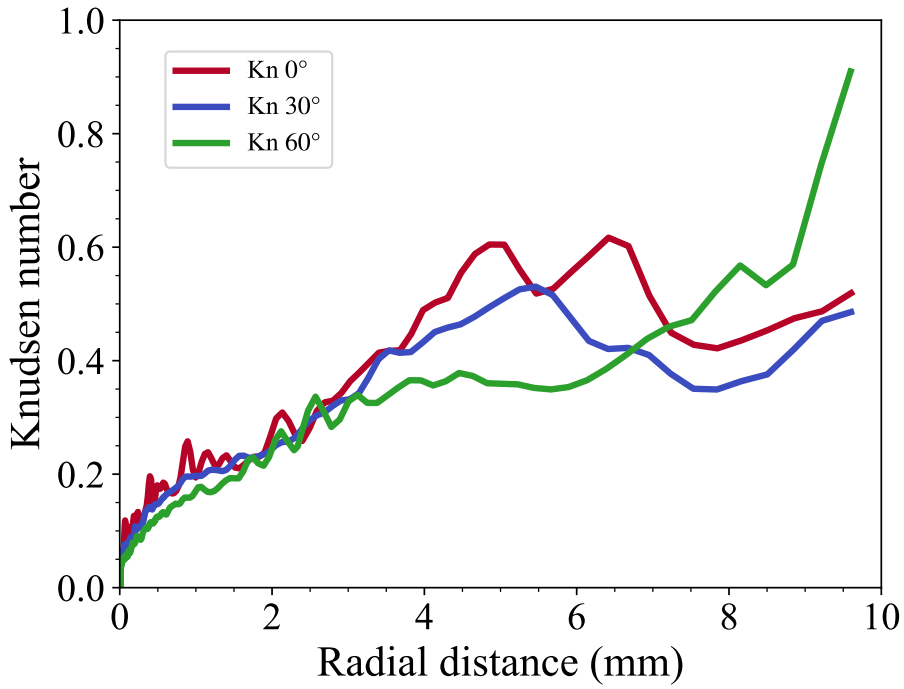


Figure 3.7: Lineouts of the Knudsen number (Eq. 3.6) at $t = 140$ ns. The lineouts begin at the droplet center of mass ($z = 0.329$ mm) and emanate radially at angles $\alpha = 0°$, 30°, and 60° (red, blue, and green curves, respectively).

The rather large values obtained for Kn call into question the treatment of the plasma as a fluid at distances beyond the millimeter scale. Fortunately, the increase in ion velocity

mid-flight is weak. For instance, an ion at $t = 30$ ns, $r = 0.5$ mm on the 0° lineout experiences a velocity gain of 2% by the time it reaches $r = 10$ mm. This means that pressure gradients in the 0.5–10 mm range have little effect on the ion kinetic energy. Because of the weak pressure gradients and high Knudsen number (which implies free expansion), the ion spectra presented in this work are representative of spectra measured at distances ~ 1 m, typical for experiments.[44]

3.5 Conclusion

We have quantified ion emission from $\lambda_{\text{laser}} = 2$ µm-driven tin plasmas using radiation-hydrodynamic simulations. Two cases have been studied: a 27 ns-long 'short pulse' case and a 'long pulse' case which involves full vaporization of the droplet ($t_{\text{vap}} \sim 150$ ns). The ion kinetic energy spectra in both cases exhibit two features: first, the peak, which is the result of steady-state laser ablation. Its intensity scales with the duration of the laser pulse. Second, the low-energy ion tail, which features low ion numbers. In the short pulse case, these ions are ablated at the end of the laser pulse while the plasma cools rapidly. In the long pulse case, the lower-energy range is suppressed as virtually all tin ions originate from a high-temperature plasma zone and thus attain high kinetic energies.

The angular dependence of spectrum-derived quantities is studied: the peak ion kinetic energy is maximal along the laser axis, and decreases as a function of the detector angle α. The emergence of a second, lower-energy peak causes a discrete fall in peak kinetic energy at $\alpha \sim 70°$. This second peak is caused by a slower-moving secondary tin outflux originating at late times. The angular ion emission $dN^* d\Omega^{-1}$ is approximately isotropic but increases for $\alpha > 70°$. The angular energy emission $dE^* d\Omega^{-1}$ is maximal at $\alpha \sim 25°$ and slightly decreases for larger angles.

An angle-resolved scan of the peak kinetic energy for different intensities displays a power law relationship in agreement with scaling relations found in the literature. Laser intensity is thus a practical way of changing the peak kinetic energy.

Calculations of the local Knudsen number reveal large values on the mm scale (Kn ~ 0.1 at $r = 0.5$ mm). While this suggests that hydrodynamic modeling beyond the mm scale is not physically meaningful, the near-free expansion at large distances validates directly comparing simulated spectra with experimental ones.

Acknowledgments

We would like to thank Hugo França for his assistance with data processing and Oscar Versolato for his comments on the manuscript. This publication is part of the project ARIES with file number 20152 of the research programme VENI which is (partly) financed by the Dutch Research Council (NWO) under an NWO grant. This project has received funding from the European Research Council (ERC) Consolidator Grant Agreement ID 101086839. This publication is also part of the project 'Plasma driven by a variable-wavelength laser for next-generation EUV sources for nanolithography' (with project number 19458) of the Open Technology Programme which is financed by NWO. This work was conducted at the Advanced Research Center for Nanolithography, a public–private partnership between the University of Amsterdam, Vrije Universiteit Amsterdam, University of Groningen, the

Netherlands Organization for Scientific Research (NWO), and the semiconductor equipment manufacturer ASML, and was (partly) financed by 'Toeslag voor Topconsortia voor Kennis en Innovatie (TKI)' from the Dutch Ministry of Economic Affairs.

Chapter 4

A refined model for laser absorption in plasmas involving the Langdon effect

Stan J. J. de Lange,* Bowie Brewster, and John Sheil.
Submitted for publication.

Recently, Sherlock *et al.*[106] have proposed corrections to the inverse bremsstrahlung laser absorptivity formula, accounting for the electron velocity-dependence of the Coulomb logarithm and for a super-Gaussian electron velocity distribution, as predicted by the Langdon effect. We develop this theory further, particularly in the context of a gadolinium plasma with a temperature $T_e = 100$ eV and a charge state $Z = 20$. Considering the particular upper and lower scattering bounds relevant to this case, we present an integral expression for the absorptivity. This integral has a series expansion, derived in a separate work,[107] which, to first order, yields a simple formula: the standard thermal Coulomb logarithm plus an additional term. This formula is numerically light, accurate, and significant for a wide range of laser wavelengths and intensities, and is therefore suitable for usage in numerical codes.

*Contributions to this chapter include performing theoretical derivations, analyzing and visualizing the numerical data, and writing and editing the manuscript.

4.1 Introduction

In 1980, A. B. Langdon predicted that laser-heated plasmas will develop non-equilibrium electron velocity distributions.[30] This phenomenon, now known as the *Langdon effect*, arises because the electric field of the laser imparts momentum to the electrons via inverse bremsstrahlung (IBA). As a result, the electrons are driven out of the equilibrium (Maxwellian) distribution that is set by electron–electron collisions, and the resulting electron distributions resemble super-Gaussian functions[108] of the form $f_m(v) \propto \exp(-[v/v_m]^m)$. Here, v is the electron velocity, v_m is a rescaled velocity proportional to the electron thermal velocity v_t and m is the order of the super-Gaussian. The Maxwellian distribution has $m = 2$, and strong electric fields can distort the distribution up to $m = 5$. The Langdon effect has since been observed in plasmas covering a range of densities and temperatures.[109,110,111,112]

The Langdon effect has important consequences for many plasma processes; atomic kinetics and radiative properties,[113,114,115,116,117,118] thermal conduction,[119,116,120] and of course laser absorption. It results in a *lower* laser absorptivity than in an equilibrium distribution. This reduction was quantified in the recent experiments of Turnbull *et al.*[121,122,123] in direct-driven fusion conditions. In Ref. [121], they reported the first experimental measurement of IBA in a laser-driven plasma. They conclude that (i) Langdon's absorption reduction is necessary to explain their data, (ii) the quantity $b_\omega = v/\omega$ must be used for the maximum impact parameter (b_{max}) in the Coulomb logarithm ($\ln\Lambda$) for IBA (where ω is the angular frequency of the laser), rather than the Debye length λ_D, and (iii) ion screening reduces the absorption further. Concerning the second point, it was found that choosing $b_{max} = \lambda_D$ (standard procedure in electron transport theories) significantly overestimated laser absorption. These experiments probed an underdense plasma where $\lambda_D > b_\omega(v_t)$, thus rendering λ_D an inappropriate maximum impact parameter for electrons with $v \gg v_t$.

The first goal of our paper is to identify appropriate impact parameters for plasmas driven by longer-wavelength laser pulses, in particular lasers of wavelengths $\lambda_{las} = 2$ µm and 10 µm relevant for EUV lithography.[61,71,65] The second goal of our study is to make accurate calculations of laser absorption in plasmas by explicitly accounting for (i) the super-Gaussian nature of the electron distribution, and (ii) the velocity dependence of $\ln\Lambda$. Both of these aspects were studied in the recent works of Turnbull *et al.*[122] and Sherlock *et al.*[106] in the context of direct-driven fusion, where they led to a reduction in absorption by as much as 30%. Sherlock *et al.* derived formulas for laser absorptivity, specifically for $b_{max} = b_\omega$, which are valid in both the classical and quantum regime. They found analytic solutions for $m = 2, 4, 6$ in terms of Meijer-G functions; intermediate values were then inferred from a quadratic spline fit. In our work, we present perturbative formulas valid for *any* m using techniques of contour integration; this derivation is presented in detail in Chapter 5. Here, we use these formulas to quantify laser absorption in a variety of plasma environments, where both λ_D and b_ω can be treated as maximum impact parameters. This builds on our group's recent work on the Langdon effect in short-wavelength source plasmas.[124] The simple form of our formulas makes their implementation in radiation-hydrodynamics codes very straightforward.

We consider a scenario where a laser of wavelength λ_{las} and intensity I_{las} heats a plasma to an electron temperature T_e[*] having an effective charge state $Z_{eff} \equiv \langle Z^2\rangle/\langle Z\rangle$ where Z denotes the charge state of an ion. The ion and electron temperatures are assumed to be

[*] We suppress all instances of Boltzmann's constant k_B in equations in this work.

equal. We will quantify laser absorption at free electron densities n_e in the vicinity of the critical electron density $n_{e,c} = m_e\omega^2\epsilon_0/e^2$ (where ϵ_0 is the vacuum permittivity and e is the elementary charge). We will adopt laser intensities and wavelengths in the ranges $I_{las} = 1$–5×10^{12} W cm^{-2} and $\lambda_{las} = 1$–10 µm. As will be detailed in section 4.2 below, the ratio Z_{eff}/T_e determines the magnitude of the Langdon effect. Much of the analysis presented in this paper will be done for a fixed value $Z_{eff}/T_e = 0.2$ given its relevance for both EUV and beyond-EUV plasma radiation sources.[125,126] In particular, plasmas containing multiply charged gadolinium and terbium ions with $Z_{eff} \sim 20$ and $T_e \sim 100$ eV radiate intensely near a wavelength of 6.7 nm. The set of four quantities $(T_e, Z_{eff}, \lambda_{las}, I_{las})$ defines the parameter space; the atomic mass and structure of the particular ions play no role here besides defining the (*a priori* assumed) Z_{eff} of interest and its relation to T_e.

The paper is structured as follows. In section 4.2 we provide a detailed overview of the theory of laser absorption, including a discussion of velocity-dependent impact parameters relevant to short-wavelength radiation sources. We then proceed to calculate laser absorption in a plasma with super-Gaussian electron distribution functions (EDFs), taking into account the velocity dependence of the Coulomb logarithm. We present a simple perturbative formula for calculating laser absorption for arbitrary super-Gaussian exponent m. The formula pertaining to the first-order approximation is compared to exact, numerical values. This formula is then applied in section 4.3, where its value relative to the conventional, thermal Coulomb logarithm $\ln\Lambda_t$ is evaluated for a range of laser wavelengths and intensities. We briefly consider indirect-driven fusion conditions, where we calculate the absorption reduction for plasma parameters reported by Blancard *et al.*[118]. In the conclusion, we recall the most important results, and offer criteria for accurate implementation of the formulas in numerical codes.

4.2 Theory

4.2.1 The Langdon effect and electron distribution functions

In this work, we consider super-Gaussian functions of the form

$$f_m(v) = C_m \frac{n_e}{2^{3/2}v_t^3} \exp\left(-\left[\frac{v}{\alpha_e\sqrt{2}v_t}\right]^m\right), \tag{4.1}$$

where $v_t \equiv \sqrt{T_e/m_e}$, $\alpha_e^2 \equiv (3/2)\Gamma(3/m)/\Gamma(5/m)$, $\Gamma(s) \equiv \int_0^\infty t^{s-1}e^{-t}dt$ is the gamma function, and $C_m \equiv m/(4\pi\alpha_e^3\Gamma(3/m))$ is a normalization factor. For $m = 2$, $\alpha_e = 1$ and $C_2 = \pi^{-3/2}$; this retrieves the Maxwellian distribution. With the distribution defined in this way, $\int f_m(v)d^3v = n_e$.

The exponent m depends on the ratio of the electron–ion diffusion coefficient (which controls IBA-induced deformation) to the electron–electron diffusion coefficient (which drives relaxation towards equilibrium).[120] This ratio—a dimensionless parameter—is given by $\alpha = Z_{eff}v_{osc}^2/v_t^2$, where $v_{osc} \equiv eE_0/m_e\omega$ is the electron oscillation velocity in the laser field, and $E_0 = \sqrt{2I_{las}/c\epsilon_0}$ is the electric field amplitude. Using the definitions of v_{osc} and v_t, one has

$$\alpha = 3.74 \times 10^{-13} I_{las} \lambda_{las}^2 Z_{eff} / T_e, \tag{4.2}$$

where I_{las}, λ_{las} and T_e have units of W cm^{-2}, µm, and eV, respectively. Fokker–Planck simulations of Matte *et al.*[108] found that m depends on α in the following way:

$$m(\alpha) = 2 + \frac{3}{1 + 1.66/\alpha^{0.724}}. \tag{4.3}$$

In the limit of small α, when electron–electron collisions dominate, $m \to 2$; the Maxwellian value. In the opposite limit where IBA heating dominates, $m \to 5$. In Fig. 4.1 we present super-Gaussian EDFs for different values of m. The vertical dotted line (grey) indicates the thermal velocity v_t. We show the extreme values $m = 2$ and 5 (dashed lines) and three intermediate cases $m = 2.3$, 2.6, and 4.2 which correspond to plasmas with $Z_{eff} = 20$, $T_e = 100$ eV, $I_{las} = 1 \times 10^{12}$ W cm^{-2} and $\lambda_{las} = 1$, 2, 10 µm (solid lines).

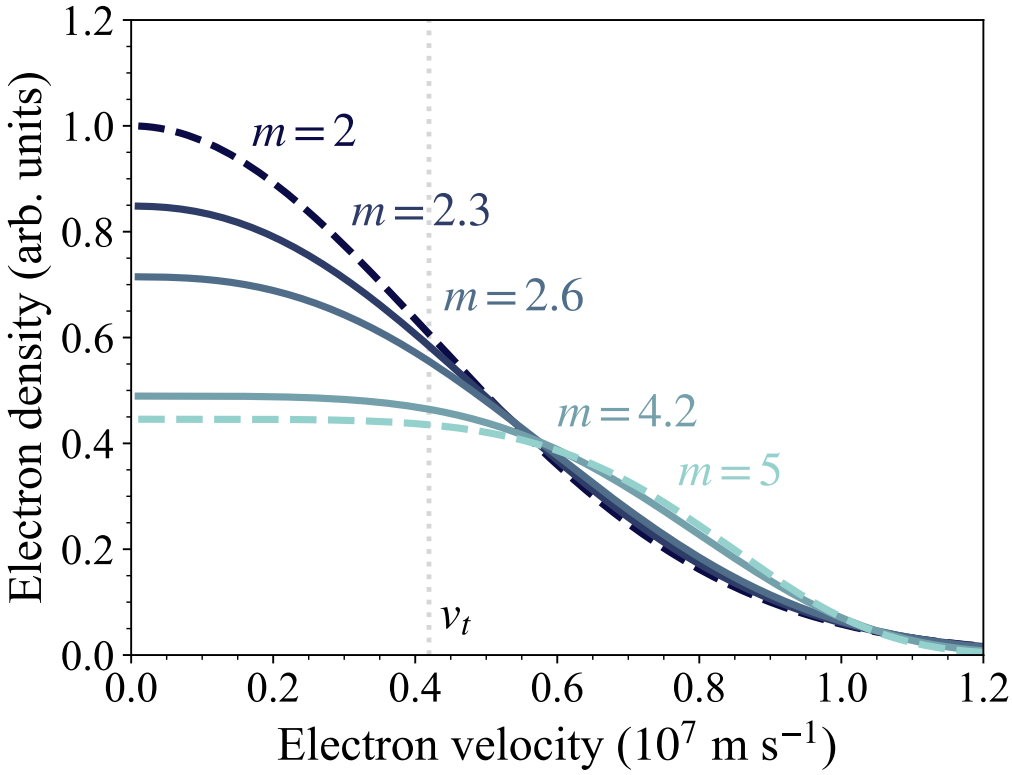


Figure 4.1: Scaled super-Gaussian electron distributions $f_m(v)/f_2(0)$ for selected values of m. The dashed curves are the extreme values $m = 2$ and 5, and the vertical dotted line (grey) indicates the thermal velocity v_t. Solid curves correspond to plasmas with $T_e = 100$ eV, $Z_{eff} = 20$, $I_{las} = 1 \times 10^{12}$ W cm^{-2} and laser wavelengths $\lambda_{las} = 1$, 2, and 10 µm, producing the values $m = 2.3$, 2.6, and 4.2, respectively.

The reduction in laser absorptivity is attributed to the reduction in the number of low-velocity electrons.[30,108,122] This reduction is typically incorporated in rad-hydro codes by mul-

tiplying the IBA coefficient k_ω (units: m^{-1}) by a factor f_L known as the Langdon factor.[122] The IBA absorption coefficient reads[29]

$$k_\omega = \frac{16\sqrt{2}\pi^{3/2}}{3}\left(\frac{e^2}{4\pi\epsilon_0}\right)^3 \frac{Zn_e^2}{(m_e T)^{3/2} c\omega^2} \ln\Lambda. \tag{4.4}$$

where c is the speed of light, Z is the charge state of the ion, and $\ln\Lambda$ is the Coulomb logarithm. The Langdon factor takes the form

$$f_L = 1 - \frac{0.553}{1 + (0.27/\alpha)^{0.75}}. \tag{4.5}$$

Langdon arrived at this formula by making fits of the laser absorptivity to α from particle-in-cell simulations.[30] Crucially, the Coulomb logarithm used in that work (as well as the later work of Matte *et al.*[108]) is independent of velocity. This has the (mathematical) consequence that Eq. (4.5) is an approximation of $C_m/C_2 = C_m\pi^{3/2}$: the ratio of the super-Gaussian normalization factor of order m, to one with $m = 2$. Our group recently computed f_L for a range of conditions encountered in laser-driven EUV sources,[124] where we found that $f_L \sim 0.8$ for CO_2-driven plasma conditions; that is, the absorption is 20% lower than expected than when assuming a Maxwellian distribution.

4.2.2 Impact parameters

As seen earlier in Eq. (4.4), the laser absorptivity depends on the Coulomb logarithm, $\ln\Lambda$. It takes the form $\ln\Lambda = \int b^{-1} db$, where b is the impact parameter of the electron relative to the target ion. Imposing physically informed bounds on this integral gives rise to minimum (b_{min}) and maximum (b_{max}) impact parameters, whose values depend on the plasma conditions. This gives

$$\ln\Lambda = \ln\left(\frac{b_{max}}{b_{min}}\right). \tag{4.6}$$

To ensure that this quantity is well-behaved at small electron velocities (where b_{max} may fall below b_{min}) and is asymptotically equal to Eq. (4.6), a hyperbolic form is often adopted:[127]

$$\ln\Lambda = \ln\left(\sqrt{1 + \left(\frac{b_{max}}{b_{min}}\right)^2}\right). \tag{4.7}$$

It is common to take as b_{max} the (electron) Debye screening length λ_D. This is the distance over which the electrostatic potential of an ion is exponentially reduced, or screened, by free electrons. It is given by

$$\lambda_D = \sqrt{\frac{\epsilon_0 T_e}{e^2 n_e}}. \tag{4.8}$$

If the plasma is heated by a laser, there is another relevant length scale: the distance over which laser light is efficiently absorbed. This length scale is given by $b_\omega(v) \equiv v/\omega$. For impact parameters $b > b_\omega$, laser heating is ineffective because the collision time is much longer than the period of the laser pulse (viewed from the perspective of the bremsstrahlung process, collisions between electrons and ions with $b > b_\omega$ yield negligible emission).[128] In practice, the cut-off is whichever of λ_D and b_ω is smaller; that is, $b_{max} = \min(\lambda_D, b_\omega)$. In this paper we do not consider other screening lengths (such as the total electron–ion Debye length or Wigner–Seitz radius) or their effect on plasma absorption through the Rozsnyai correction factor (see Turnbull *et al.*[121,122] and Sherlock *et al.*[106] for extensive discussions on this point).

The minimum impact parameter b_{min} is taken to be the larger of two length scales: the impact parameter for classical perpendicular scattering, $b_\perp(v) = Ze^2/4\pi\epsilon_0 m v^2$, and the reduced de Broglie wavelength $b_q(v) = \hbar/2mv$. For the cases considered in this work, we find $b_\perp(v) > b_q(v)$ for all relevant v, and thus we take $b_{min} = b_\perp(v)$.

In Fig. 4.2 we plot the quantities b_ω (blue), λ_D (red), $b_\perp$ (green) and b_q (purple) as a function of electron velocity for plasmas with $T_e = 100$ eV, $Z_{eff} = 20$, $I_{las} = 1 \times 10^{12}$ W cm^{-2}, and (a) $\lambda_{las} = 2$ µm and (b) $\lambda_{las} = 10$ µm. We consider absorption at the critical electron density: $n_e \equiv n_{e,c}$. Note that $b_\omega(v = v_t) \equiv b_{\omega t} = \lambda_D(n_e = n_{e,c})$. The impact parameters shown as solid lines are the relevant b_{max} or b_{min}; otherwise they are shown as a dashed line. In this way, b_{max} is divided into two ranges: b_ω for $v < v_t$ (blue), and λ_D for $v > v_t$ (red). In the range $v < 0.17 \times 10^7$ m/s of subplot (a), one has $b_{min} > b_{max}$, rendering the theory invalid. Nevertheless, this can still be handled by using Eq. (4.7).

That absorption should occur *at* the critical density is not necessarily the case; for instance, absorption in plasmas driven by shorter-wavelength lasers (*e.g.* $\lambda_{las} = 1$ or 2 µm) is dominant in the underdense corona.[29] The Debye length λ_D typically increases the further one moves away from the critical surface. A larger λ_D means the switch from b_ω to λ_D occurs for larger v, meaning the range of velocities where $b_{max} = b_\omega$ increases.

4.2.3 Laser absorption involving super-Gaussian electron distributions

With knowledge of the relevant impact parameters and their dependence on electron velocity, we now proceed to quantify laser absorption in plasmas with super-Gaussian EDFs. Building on the analysis of Sherlock *et al.*,[106] we consider a velocity-dependent Coulomb logarithm $\ln\Lambda(v)$, rather than the thermal Coulomb logarithm $\ln\Lambda_t \equiv \ln\Lambda(v = v_t)$. We use $b_{max} = \lambda_D$ for all v; we will find that this assumption leads to an over-estimation of laser absorption by a few percent at most. We also set $b_{min} = b_\perp$, as discussed above.

Sherlock *et al.*[106] derived the following expression for the absorbed laser power per unit volume:

$$\langle P \rangle = -A m_e v_{osc}^2 \frac{2\pi}{3} \int_0^\infty \frac{df_m(v)}{dv} \ln\Lambda(v) dv, \tag{4.9}$$

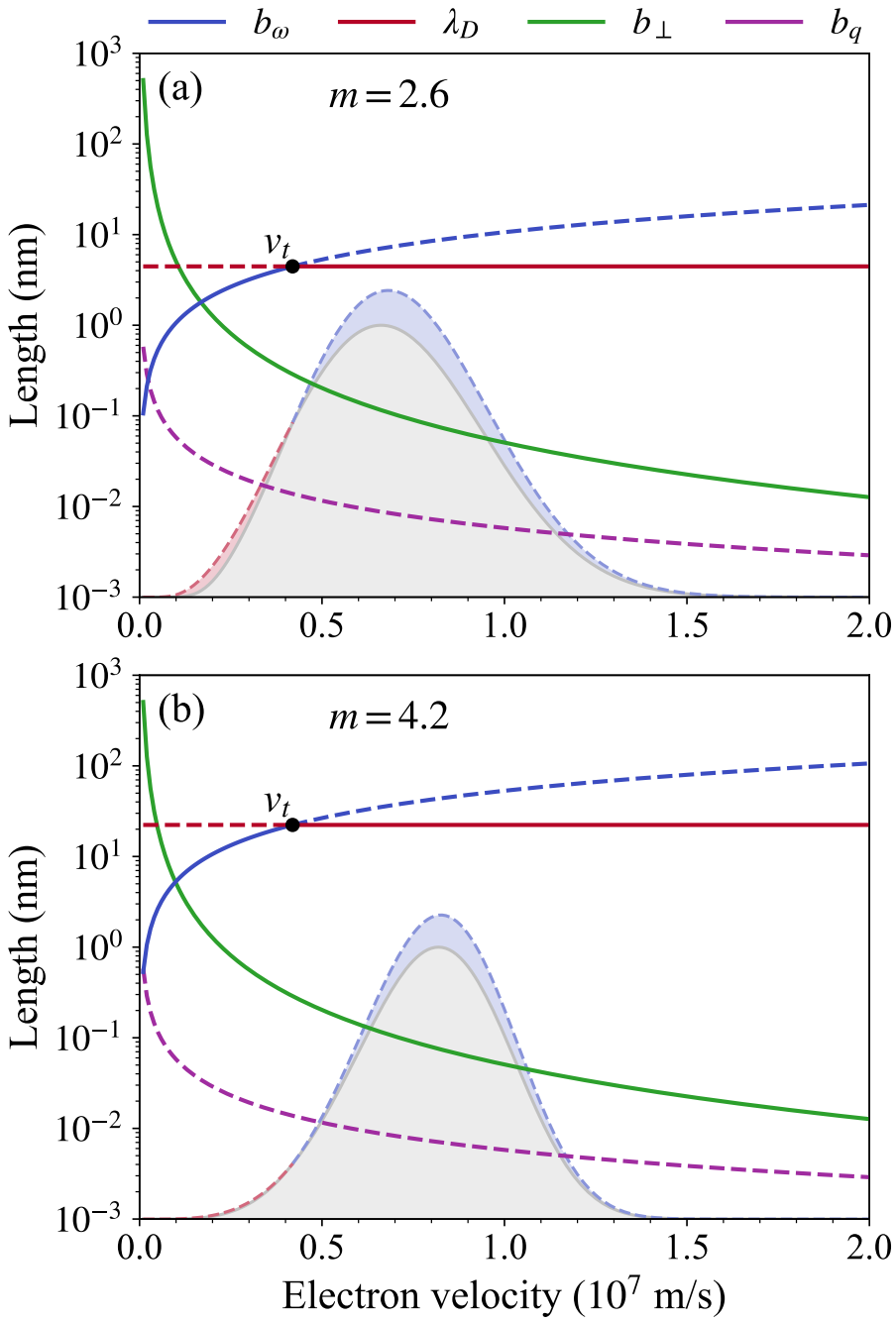


Figure 4.2: Upper and lower impact parameters as a function of velocity for (a) $\lambda_{las} = 2$ µm and (b) $\lambda_{las} = 10$ µm irradiation of plasmas with $I_{las} = 1 \times 10^{12}$ W cm^{-2}, $T_e = 100$ eV, $Z_{eff} = 20$. The curves show the length scales b_ω (blue), λ_D (red), $b_\perp$ (green), and b_q (purple). The shaded area is the integrand of Eq. (4.9) (arbitrary units). Gray represents the integrand for $b_{max} = \min(\lambda_D, b_\omega)$. The red and blue regions show the additional area when integrating using $b_{max} = \lambda_D$ (red) and $b_{max} = b_\omega$ (blue) everywhere.

where $A = 4\pi n_i (Ze^2/4\pi\epsilon_0 m_e)^2$. Considering a Maxwellian distribution ($m = 2$) and $\ln\Lambda = \ln\Lambda_t$, the following expression for $\langle P\rangle$ is retrieved:

$$\langle P\rangle = \frac{1}{3}\sqrt{\frac{2}{\pi}} A v_t^{-3} n_e \frac{1}{2} m_e v_{osc}^2 \ln\Lambda_t, \tag{4.10}$$

we retain the general v-dependence of the Coulomb logarithm and consider a generic super-Gaussian distribution $f_m(v)$. Using the Coulomb logarithm of Eq. (4.7), and re-writing the integral using integration by parts, one obtains:

$$\begin{aligned}\langle P\rangle = {} & A m_e v_{osc}^2 \frac{2\pi}{3}\frac{C_m n_e}{2^{3/2} v_t^3} \\ & \times \int_0^\infty \exp\left(-\left[\frac{v}{\alpha_e\sqrt{2}v_t}\right]^m\right)\frac{d\ln\Lambda(v)}{dv} dv.\end{aligned} \tag{4.11}$$

For the impact parameters specified above, $\ln\Lambda(v) = \ln\left(\sqrt{1+\lambda_D^2 b_{\perp t}^{-2} v_t^{-4} v^4}\right)$, where $b_{\perp t} \equiv b_\perp(v_t)$. Recasting Eq. (4.11) into a form similar to Eq. (4.10), we have:

$$\langle P\rangle = \frac{1}{3}\sqrt{\frac{2}{\pi}} A v_t^{-3} n_e \frac{1}{2} m_e v_{osc}^2 C_m \pi^{3/2} I_m. \tag{4.12}$$

where

$$I_m = \int_0^\infty e^{-u^m} \frac{2u^3}{u^4 + c^{-1}} du. \tag{4.13}$$

Here $u \equiv v/(\alpha_e\sqrt{2}v_t)$ and $c \equiv (\sqrt{2}\alpha_e)^4 \lambda_D^2 b_{\perp t}^{-2}$, both of which are dimensionless quantities. The two differences with respect to Eq. (4.10) are the appearance of the Langdon factor $f_L = C_m\pi^{3/2}$ and the 'Coulomb integral' I_m, which has replaced the thermal Coulomb logarithm.

We have found that the integral in Eq. (4.13) has an analytical solution for rational values of m in terms of Meijer-G functions. For generic m, the integral can be solved by transforming it to an integration in the complex plane and summing over the residues of the poles. This procedure yields an expansion of I_m in terms of powers of cWe present this derivation in detail in Ref. [107]. The general result for a super-Gaussian EDF and a Coulomb logarithm that scales like $\ln\Lambda(u) = \ln(\sqrt{1+cu^\beta})$ is as follows:

$$\begin{aligned} I_m = {} & \frac{1}{2}\ln c - \frac{\beta\gamma}{2m} \\ & + \sum_{n=1}^{\infty}\Big[-\frac{(-1)^n}{n!}\frac{\pi}{2}c^{-nm/\beta}\csc(\pi n m/\beta) \\ & \qquad + (-1)^n \frac{\beta}{2m}\Gamma(-\beta n/m)c^{-n}\Big].\end{aligned} \tag{4.14}$$

The case $b_{max}/b_{min} = \lambda_D/b_\perp$ corresponds to $\beta = 4$; using the definitions of c and α_e given above, the first-order approximation of Eq. (4.14) is

$$I_m \approx \ln\left(\frac{\lambda_D}{b_{\perp t}}\right) + 2T(m), \tag{4.15}$$

where

$$T(m) = \frac{1}{2}\ln\left[3\frac{\Gamma(3/m)}{\Gamma(5/m)}\right] - \frac{\gamma_E}{m}. \tag{4.16}$$

$\gamma_E \approx 0.577$ is the Euler–Mascheroni constant. The whole procedure has boiled down to the inclusion of a new m-dependent term $2T(m)$, which is plotted in Fig. 4.3 (red curve). It takes on a value between 0.116 ($m = 2$) and 1.266 ($m = 5$). Eq. (4.15) is a practical and conceptual simplification of the results of Sherlock *et al.*,[106] whose procedure consists in using the known analytical results $m = 2, 4, 6$ to construct a spline, and interpolating at the relevant m. That said, they consider a broader parameter space, also valid in the quantum regime, by setting $b_{max} = (b_\omega^2 + b_\perp^2)^{1/2}$ and $b_{min} = (b_q^2 + b_\perp^2)^{1/2}$. Our present derivation is restricted to the classical regime.

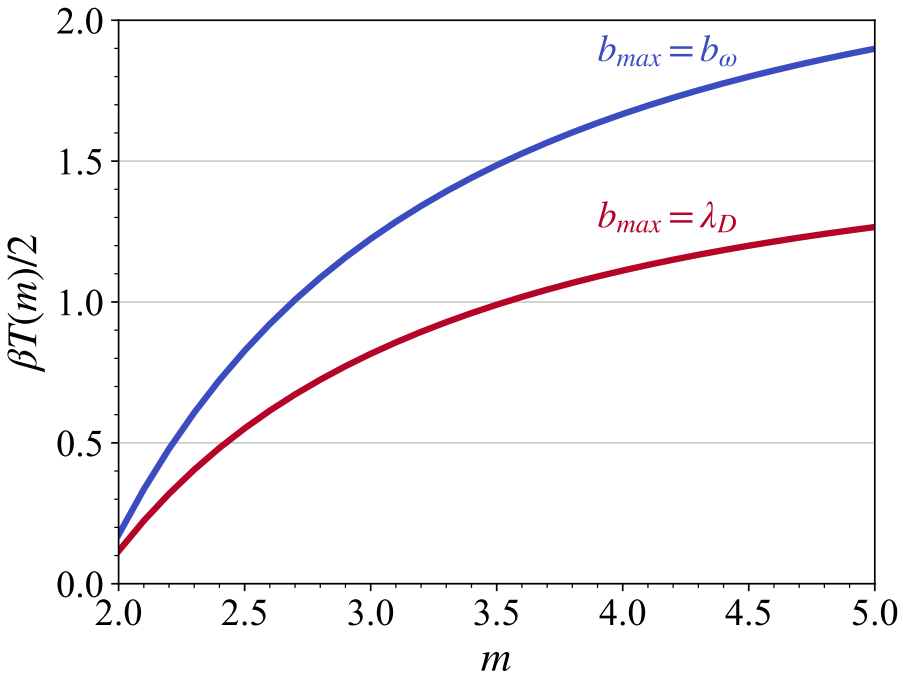


Figure 4.3: The term $\beta T(m)/2$ appearing in the first order of the Coulomb integrals, Eqs. (4.13) and (4.18). The red and blue curves correspond to $b_{max} = \lambda_D$ ($\beta = 4$) and $b_{max} = b_\omega$ ($\beta = 6$), respectively.

Eq. (4.15) has an error that scales like $c^{-1/2}$ at worst, which is for $m = 2$. If an error of ~ 0.1 is deemed acceptable, then Eq. (4.15) is accurate for $c \gtrsim 100$. With $b_{max} = \lambda_D$ and $b_{min} = b_\perp$, c increases with wavelength, and (more weakly) with intensity. For instance,

for $\lambda_{las} = 1$ µm and $I_{las} = 10^{12}$ W cm^{-2}, $c = 347$ at the critical electron density ($n_e = 10^{21}$ cm^{-3}). Eq. (4.15) then gives an error of 3%. For $\lambda_{las} = 10$ µm and $I_{las} = 10^{12}$ W cm^{-2}, we obtain $c \approx 10^5$; here the error is only 0.2%.

Caution must be taken when higher-order terms in Eq. (4.14) are computed, since their prefactors may diverge: specifically, singularities are encountered for $m = 2$ and $m = 4$. These singularities have no physical significance, but are merely a consequence of how I_m is written as a series. This can be dealt with by taking a Taylor expansion of the terms around the problematic values; this cancels out the singular parts. Results relevant here can be found in the Appendix.

As previously mentioned, absorption in the underdense corona involves larger Debye lengths, and the range where $b_{max} = b_\omega$ dominates the integral. It is interesting to consider the case where $b_{max} = b_\omega$ for all v. This has already been considered by Sherlock *et al.*,[106] but to our knowledge the generalization to any m is new. In this case, the Coulomb logarithm is of the form

$$\ln\Lambda = \sqrt{1 + b_{\omega t}^2 b_{\perp t}^{-2} v_t^{-6} v^6}, \tag{4.17}$$

which yields the following integral:

$$J_m = \int_0^\infty e^{-u^m} \frac{3u^5}{u^6 + c^{-1}} du. \tag{4.18}$$

In this equation, $c \equiv (\sqrt{2}\alpha_e)^6 b_{\omega t}^2 b_{\perp t}^{-2}$. Eq. (4.14) can once again be used (with $\beta = 6$), and the following first-order behaviour is obtained:

$$J_m \approx \ln\left(\frac{b_{\omega t}}{b_{\perp t}}\right) + 3T(m). \tag{4.19}$$

We have thus considered the two edge cases, where b_{max} is identified with either λ_D or b_ω for all integrated velocities in Eq. (4.11). The validity of setting $b_{max} = \lambda_D$ for all v is visualized in Fig. 4.2. The gray area is the integrand of Eq. (4.11), evaluated using $b_{max} = \min(\lambda_D, b_\omega)$. The red area is the additional absorptivity found when $b_{max} = \lambda_D$ is used for $v < v_t$. Clearly the effect of this approximation is small in this case. Likewise, the blue area is the additional absorptivity calculated when $b_{max} = b_\omega$ is used for $v > v_t$; this is significantly less accurate. We note that most absorptivity is due to electrons of velocities somewhat larger than v_t, whereas low-velocity electrons are little affected.

It is informative to see the accuracy of the approximations of the Coulomb integrals as a function of the electron density n_e. This is illustrated in Fig. 4.4. The red and blue curves use $b_{max} = \lambda_D$ and $b_{max} = b_\omega$, respectively. Naturally, the former is most accurate for high densities ($n_e \gg n_{e,c}$), and the latter is appropriate for subcritical densities ($n_e \ll n_{e,c}$). The 'exact' Coulomb integral (black), the integral in Eq. (4.11), is integrated with the rule

$b_{max} = \min(\lambda_D, b_\omega)$; it is always smaller than both I_m and J_m. The solid curves are obtained by numerical integration of Eqs. (4.13) and (4.18); the dashed curves are obtained from Eqs. (4.15) and (4.19), and show very good agreement.

When using the first-order approximations, one finds that the largest discrepancy with the exact value is where the two cases intersect. At $n_e = 1.42 \times 10^{20}$ cm^{-3} in Fig. 4.4, the Coulomb logarithm is overestimated by 0.17, or 5%. Using Eqs. (4.15) and (4.19), the electron density at which the two curves intersect is approximately

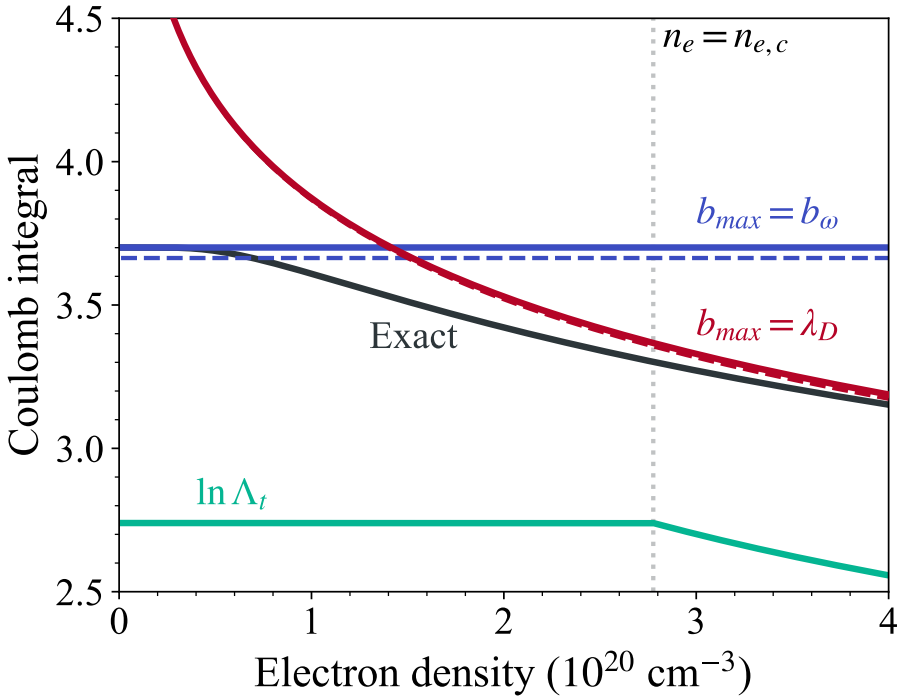


Figure 4.4: The Coulomb integrals as a function of electron density, with $T_e = 100$ eV, $Z_{eff} = 20$, $\lambda_{las} = 2$ µm, and $I_{las} = 10^{12}$ W cm^{-2}. The critical density is indicated by the vertical dotted line. The velocity integral of Eq. (4.11) is calculated assuming $b_{max} = \lambda_D$ for all v (red), $b_{max} = b_\omega$ for all v (blue), and $b_{max} = \min(\lambda_D, b_\omega)$ (black). The dashed red (I_m) and blue (J_m) lines show the first-order approximations given by Eqs. (4.15) and (4.19). The light blue curve shows the thermal Coulomb logarithm $\ln \Lambda_t$, with $b_{max} = \min(\lambda_D, b_\omega)$.

$$n_{e,i} = n_{e,c} e^{-2T(m)}. \tag{4.20}$$

As such, the best value for the Coulomb logarithm is given by $b_{max} = b_\omega$ when $n_e < n_{e,i}$, and $b_{max} = \lambda_D$ when $n_e > n_{e,i}$.

Lastly, one might wonder if there exists an analytic formula for an integral from 0 to $u_t \equiv 1/(\alpha_e\sqrt{2})$ (*i.e.* $v = v_t$), and from u_t to ∞, so that the proper b_{max} can always be used. Unfortunately, this is not the case. In short, the cosecant in Eq. (4.14) was obtained from an identity involving an integral over the $[0, \infty)$ range. No such identity exists for other bounds, and this stops us from writing such an integral as a sum of residues.

4.3 Wavelength and intensity scans

We will now apply the theory described above to a variety of plasmas. First, we define f_r as the ratio of I_m to the thermal Coulomb logarithm:

$$f_r = \frac{I_m}{\ln\left(\frac{\lambda_D}{b_{\perp t}}\right)} \approx 1 + \frac{\ln\left[3\frac{\Gamma(3/m)}{\Gamma(5/m)}\right] - \frac{2\gamma_E}{m}}{\ln\left(\frac{\lambda_D}{b_{\perp t}}\right)}. \tag{4.21}$$

We first consider the values f_L (Eq. (4.5)) and f_r as a function of λ_{las} (1–10 µm), for fixed $I_{las} = 10^{12}$ W cm^{-2}. The results are shown in Fig. 4.5. As before, $T_e = 100$ eV, $Z_{eff} = 20$, and $n_e = n_{e,c}$. The familiar Langdon factor f_L decreases with wavelength; it falls from 0.85 (1 µm) to 0.49 (10 µm). The ratio f_r weakly counteracts this: it rises from 1.20 (1 µm) to 1.26 (10 µm). Combined, the quantity $f_L f_r$ falls from 1.02 to 0.62. When λ_{las} is tuned, λ_D and m are affected, but not $b_{\perp t}$. The solid orange and green curves show f_r and $f_L f_r$ calculated numerically, while the dashed curves use Eq. (4.15). The numbers on the green curve show super-Gaussian exponents m induced by a particular laser wavelength.

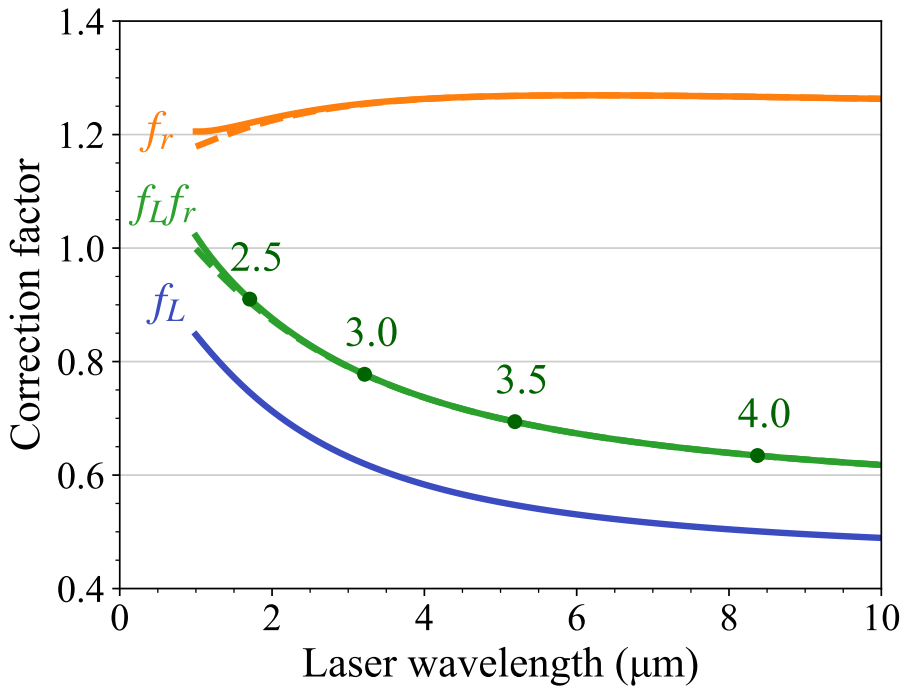


Figure 4.5: Laser wavelength scan of the Langdon factor (f_L, blue) and the ratio $I_m / \ln \Lambda_t$ (f_r, orange). The dashed lines show the values obtained by approximating I_m through Eq. (4.15). The numbers on the combined curve ($f_L f_r$, green) indicate m at half-integer values.

The same analysis is conducted for variable laser intensity, see Fig. 4.6. λ_{las} is held fixed at 1 µm, and we scan over the intensities $I_{las} = 1$–5×10^{12} W cm^{-2}. This means $\lambda_{las} = 1$ µm in Fig. 4.5 corresponds to $I_{las} = 1 \times 10^{12}$ W cm^{-2} in Fig. 4.6. Since, in practice, temperature and charge state vary with laser intensity, we implement power laws for temperature [102] and charge state:

$$T_e = 100 \times (10^{-12} I_{las})^{0.5}, \quad Z_{eff} = 20 \times (10^{-2} T_e)^{0.6}. \tag{4.22}$$

In these formulas, T_e is in units of eV, and I_{las} in W cm^{-2}. The prefactors 100 and 20 are fixed to agree with values used previously. Compared to the wavelength scan, the change in m for varying intensities is relatively small. In terms of the above power laws, α scales with $I_{las}^{0.8}$ and with λ_{las}^2 (Eq. (4.2)). This leads to a weaker change in the Langdon factor: f_L decreases from 0.85 (10^{12} W cm^{-2}) to 0.72 (5×10^{12} W cm^{-2}). It very weakly affects f_r, which depends on m in the numerator: it changes from 1.21 to 1.22. The result is a decrease in $f_L f_r$ from 1.02 to 0.88: this is the total fractional change in absorptivity compared to an absorption model that does not use Langdon's correction and does not integrate over electron velocities to obtain $\ln \Lambda$. Note that $\lambda_{las} = 1$ µm was chosen to show both the exact (solid) and approximate (dashed) formulas. For wavelengths 2 µm and larger, the dashed and solid curves completely overlap.

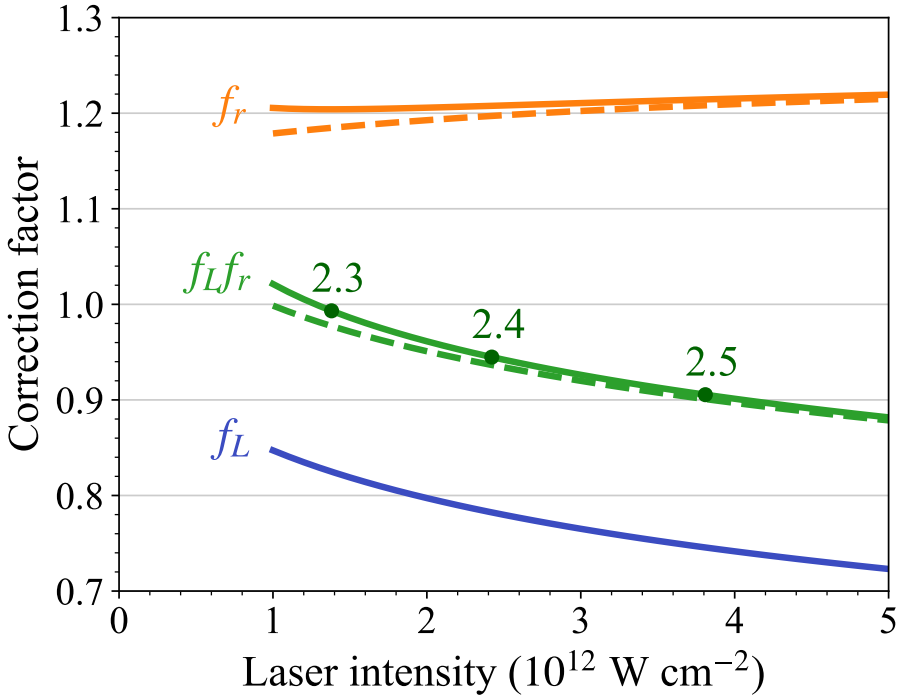


Figure 4.6: Laser intensity scan of the Langdon factor (f_L, blue) and ratio $I_m / \ln \Lambda_t$ (f_r, orange). The dashed lines show the values obtained by approximating I_m through Eq. (4.15). The numbers on the combined curve ($f_L f_r$, green) indicate m at tenth-integer values.

Finally, we will apply these results to a case in indirect-driven fusion, for conditions considered by Blancard, Cossé, and Faussurier.[118] The parameters are $T_e = 2000$ eV, $Z_{eff} = 47$, $\lambda_{las} = 0.351$ µm, $I_{\text{las}} = 3 \times 10^{15}$ W cm^{-2}, and $n_e = 10^{21}$ cm^{-3}. This yields $m \approx 3.76$. The resultant critical density is $n_{e,c} = 9.0 \times 10^{21}$ cm^{-3}, and from Eq. (4.20) $n_{e,i} = 3.1 \times 10^{21}$ cm^{-3}. Hence $n_e < n_{e,i}$, and the velocity integral is therefore accurately calculated using $b_{max} = b_\omega$ for all v. From Eq. (4.19) one obtains $J_m = 6.23$: an increase of 1.59 on the thermal Coulomb logarithm $\ln(b_{\omega t}/b_{\perp t}) = 4.64$. J_m must of course be multiplied by the Langdon factor, $f_L = 0.52$, to obtain the final value $\ln \Lambda = 3.24$. Thus, the combined effect

of the Langdon factor and the Coulomb integral leads to a net *decrease* in absorptivity by 30%. For underdense plasmas, lower absorptivity leads to less energy transferred to the plasma, and hence a lower plasma temperature. For a dense plasma, such as a solid target, the decreased absorptivity means the laser beam can penetrate deeper into the plasma, altering the temperature distribution of the plasma, and possibly increasing reflectivity off the critical surface.

4.4 Conclusion

We have derived an improved formula for the Coulomb logarithm for laser absorption in plasmas, which integrates over all electron velocities for a super-Gaussian distribution. For absorption near the critical density, the integral is dominated by $b_{max} = \lambda_D$. The result is Eq. (4.15): the thermal Coulomb logarithm plus an extra term. If this formula is not sufficiently accurate (*e.g.* for short laser wavelengths), higher-order terms may be retained. For absorption in underdense plasmas, $b_{max} = b_\omega$ will dominate the integral, and Eq. (4.19) may be used instead.

The effect of the extra $T(m)$-term may be significant. For instance, consider the two cases of Fig. 4.2: for the $\lambda_{las} = 2$ µm case, $\ln \Lambda_t = 2.74$, and $2T(m) = 0.62$ (yielding a 23% increase); for $\lambda_{las} = 10$ µm, $\ln \Lambda_t = 4.35$, and $2T(m) = 1.14$ (a 26% increase). An even more significant enhancement was found for the underdense, indirect-driven fusion conditions discussed above.

Due to the simple form of the improved formula, it is straightforward to implement in (radiation-)hydrodynamic codes: calculate the super-Gaussian exponent m and add $2T(m)$ (or $3T(m)$ for underdense absorption) to the usual expression for $\ln \Lambda_t$. The following criteria can be used to ensure accuracy: (i) if $n_e/n_{e,i} > 1$, then $b_{max} = \lambda_D$ ($\beta = 4$), otherwise $b_{max} = b_\omega$ ($\beta = 6$); (ii) if $c \lesssim 100$, extra terms of Eq. (4.14) should be retained; and (iii) if $m \approx 2,4$ ($\beta = 4$) or $m \approx 2,3$ ($\beta = 6$), the Coulomb integral should be calculated using Eqs. (4.23)–(4.26) to avoid singularities.

Acknowledgments

We would like to thank Mark Sherlock, Felix Kohlmeier, Oscar Versolato, and Ronnie Hoekstra for useful discussions. This publication is part of the project ARIES with file number 20152 of the research programme VENI which is (partly) financed by the Dutch Research Council (NWO) under an NWO grant. This publication is also part of the project 'Plasma driven by a variable-wavelength laser for next-generation EUV sources for nanolithography' (with project number 19458) of the Open Technology Programme which is financed by NWO. This work was conducted at the Advanced Research Center for Nanolithography, a public–private partnership between the University of Amsterdam, Vrije Universiteit Amsterdam, University of Groningen, the Netherlands Organization for Scientific Research (NWO), and the semiconductor equipment manufacturer ASML, and was (partly) financed by 'Toeslag voor Topconsortia voor Kennis en Innovatie (TKI)' from the Dutch Ministry of Economic Affairs.

4.5 Appendix

The $\beta = 4$ case of the expansion of I_m given by Eq. (4.15) has singular terms for $n = 1$ at $m = 2, 4$. To avoid these, the Coulomb logarithm may instead be computed around these points using a Taylor expansion. Retaining terms up to order c^{-1}, the result for $m \approx 2$ is

$$\begin{aligned} I_m \approx & \ln\left(\frac{\lambda_D}{b_{\perp t}}\right) + 2T(m) + \frac{\pi}{2}c^{-1/2} \\ & + \frac{1}{4c}(-\ln(c) + 2\gamma_E - 3) \\ & - \frac{\pi \ln(c)}{8}c^{-1/2}(m-2) \\ & + \frac{1}{48c}(3\ln(c)^2 - 12\gamma_E^2 - \pi^2 + 24\gamma_E - 24)(m-2). \end{aligned} \tag{4.23}$$

When $m = 2$, the latter two terms vanish and one is left with the analytic $m = 2$ solution, expanded to order c^{-1}. Likewise, expanding for $m \approx 4$ yields

$$\begin{aligned} I_m \approx & \ln\left(\frac{\lambda_D}{b_{\perp t}}\right) + 2T(m) \\ & + \frac{1}{2c}(\ln(c) - \gamma_E + 1) \\ & + \frac{1}{96c}(-6\ln(c)^2 + 6\gamma_E^2 - \pi^2)(m-4). \end{aligned} \tag{4.24}$$

The $\beta = 6$ integral has two singular values in the $n = 1$ terms. For $m \approx 2$:

$$\begin{aligned} J_m \approx & \ln\left(\frac{b_{\omega t}}{b_{\perp t}}\right) + 3T(m) + \frac{\pi}{\sqrt{3}}c^{-1/3} - \frac{\pi}{2\sqrt{3}}c^{-2/3} \\ & + \frac{1}{24c}(2\ln(c) - 6\gamma_E + 11) \\ & - \frac{\pi\sqrt{3}\ln(c) + \pi^2}{18}c^{-1/3}(m-2) \\ & + \frac{\pi\sqrt{3}\ln(c) - \pi^2}{18}c^{-2/3}(m-2) \\ & + \frac{1}{288c}(-6\ln(c)^2 + 54\gamma_E^2 + 7\pi^2 - 162\gamma_E + 189)(m-2). \end{aligned} \tag{4.25}$$

And for $m \approx 3$:

$$
\begin{aligned}
J_m \approx & \ln\left(\frac{b_{\omega t}}{b_{\perp t}}\right) + 3T(m) + \frac{\pi}{2}c^{-1/2} \\
& + \frac{1}{4c}(-\ln(c) + 2\gamma_E - 3) \\
& - \frac{\pi \ln(c)}{12}c^{-1/2}(m-3) \\
& + \frac{1}{72c}(3\ln(c)^2 - 12\gamma_E^2 - \pi^2 + 24\gamma_E - 24)(m-3).
\end{aligned}
\tag{4.26}
$$

If these formulas (or at least some of their terms) are used around the respective values of m, division by zero and associated floating-point errors are avoided.

Chapter 5

Super-Gaussian integration for the Langdon effect

Bowie Brewster, Stan J. J. de Lange,* and John Sheil.
In preparation.

We provide a perturbative solution to a family of integrals relevant to inverse bremsstrahlung absorption in laser-driven plasmas. The general integral is obtained by assuming a super-Gaussian electron velocity distribution due to the Langdon effect, and keeping the velocity dependence of the maximum and minimum impact parameters in the Coulomb logarithm explicit. We provide a detailed mathematical treatment of this integral in the complex plane, and obtain a solution in the form of an infinite series. When the higher-order terms can be neglected, our results provide a simple formula that can be readily implemented in radiation-hydrodynamic codes. The Coulomb integral leads to a laser absorptivity that is generally higher than the (conventional) Coulomb logarithm evaluated at the thermal velocity. To demonstrate this, we consider a gold plasma studied by Shang *et al.*,[129] and find an 18% higher absorptivity compared to conventional values.

5.1 Introduction

Radiation-hydrodynamic simulations play a crucial role in understanding and predicting the outcomes of laser-plasma experiments.[130,131,132,34,60,133] Essential to their success is their ability to predict the attenuation of laser light in a high-temperature, strongly dynamic environment. In the context of plasma-based sources of extreme ultraviolet (EUV)[61,134] and x-ray radiation,[135,136,137] the laser is responsible for heating the plasma to temperatures where EUV/x-ray emitting charge states are created. Radiation-hydrodynamic simulations are used to pinpoint those experimental conditions (notably laser parameters and target geometry) for which the radiative properties of the plasma are optimized (see Refs. [130, 131, 132, 34, 60, 133]). Pushing these radiation sources to even higher levels of performance (*e.g.*, radiative power) demands more accurate simulation tools, and, with that, ever-more accurate models of laser absorption in plasmas.

First predicted by A. B. Langdon in 1980,[30] a phenomenon unique to plasmas heated by monochromatic (laser) radiation, and one which complicates the calculation of laser absorp-

*Contributions to this chapter include assisting with theoretical derivations and the writing of the manuscript.

tion, is the laser-induced distortion of the electron velocity distribution into a non-equilibrium (*i.e.*, non-Maxwellian) distribution. By numerically solving the time-dependent Fokker–Planck equation for electrons, Matte *et al.*[108] showed that the distorted electron distribution function (EDF) is accurately fitted by a super-Gaussian function of the form

$$f_m(v) \propto \exp[-(v/v_m)^m], \tag{5.1}$$

where v is the electron velocity, v_m is proportional to the electron thermal velocity, and the exponent m characterizes the degree of the distortion. It can take on values anywhere between $m = 2$ (a Maxwellian distribution) and $m = 5$; the exact magnitude is determined by the competition between IBA heating and electron–electron collisions. Experimental measurements of the EDF in laser-heated plasmas corroborate Langdon's prediction,[109,110,111,112] and this laser-induced distortion is nowadays known as the *Langdon effect*.

In the context of laser absorption, the Langdon effect results in a *lower* laser absorption than if the distribution were held 'fixed' in equilibrium (this is implicit in radiation-hydrodynamic simulations). This reduction in absorption was confirmed in the very recent experiments of Turnbull and collaborators,[121,122] who showed that use of the laser frequency (rather than plasma frequency) in the Coulomb logarithm $\ln\Lambda$, as well as a factor due to ion screening, was essential to reproduce experimentally measured IBA. Subsequently, Sherlock *et al.*[106] performed a detailed theoretical study of laser absorption in plasmas, presenting analytical expressions for the absorbed laser power that account for both the super-Gaussian nature of the EDF and the velocity dependence of the Coulomb logarithm. The expressions derived in that work are very complicated, involving Meijer G-functions (see Eq. (22) of Ref. [106]). This complexity motivated the authors to present simplified fits to numerical calculations of IBA integrals (see Eq. 5.4 below), which they propose can be used in radiation-hydrodynamic simulations to accurately model laser absorption.

In this Chapter, we present a perturbative solution to the IBA integrals studied in the work of Sherlock *et al.*[106] Our solution, which does not involve any fitting procedure, represents a significant simplification of the aforementioned results. We provide a detailed mathematical treatment of the IBA integral in the complex plane, and obtain a solution in the form of an infinite series. We show that higher order terms are rarely significant, and that the simple, m-dependent formula we derive be easily implemented in radiation-hydrodynamic codes.

5.2 Absorbed laser power

Our starting point is the expression derived by Sherlock *et al.*[106] for the absorbed laser power (per unit volume) for an electron velocity distribution $f_m(v)$ and a velocity-dependent Coulomb logarithm $\ln\Lambda(v)$. Neglecting constants of proportionality, the absorbed power takes the form

$$\langle P\rangle \propto \int_0^\infty f_m(v)\frac{d\ln\Lambda(v)}{dv}\,dv. \tag{5.2}$$

The (velocity-dependent) Coulomb logarithm $\ln\Lambda(v)$ quantifies the cumulative effect of Coulomb scattering over a range of interaction scales. It arises from an integral over the

impact parameter b, defined as the perpendicular distance between the initial electron trajectory and the ion. We adopt a hyperbolic form for this quantity

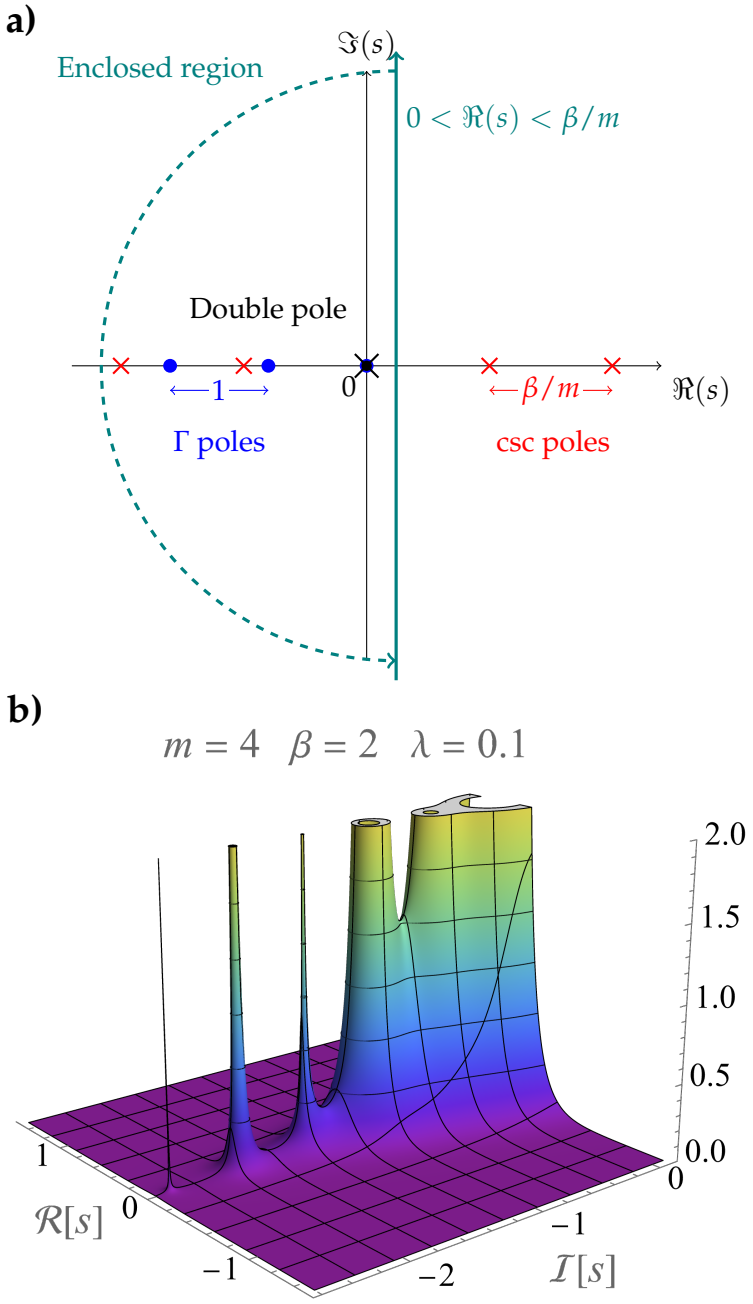


Figure 5.1: a) Schematic of the location of the poles in the integrand in Eq. 5.6. The contour must be chosen to be $0 < \Re(s) < \beta/m$, so that the double pole at 0 is included, but the poles of the cosecant function in the positive real half-plane are excluded. b) Modulus of the integrand of Eq. 5.6 for $m = 4$, $\beta = 2$, and $\lambda = 0.1$.

$$\ln\Lambda = \ln\left(\sqrt{1+\left(\frac{b_{max}}{b_{min}}\right)^2}\right), \tag{5.3}$$

where b_{min} and b_{max} represent the minimum and maximum impact parameters, respectively. A hyperbolic form ensures that this quantity remains well-behaved when $b_{max} \lesssim b_{min}$. If quantum effects can be neglected (often case in many laser-plasma conditions), one takes $b_{min} = b_\perp(v) = Ze^2/4\pi\epsilon_0 m_e v^2$; the impact parameter for classical perpendicular scattering (here Z is the ion charge state, e is the elementary charge, m_e is the electron mass and ϵ_0 is the permittivity of free space). The maximum impact parameter is taken to be the smaller of two quantities: either the Debye length $\lambda_D = \sqrt{\epsilon_0 T_e e^{-2} n_e^{-1}}$ (T_e is the electron temperature and n_e is the electron density), or the length scale over which laser absorption occurs, which is given by $b_\omega(v) \equiv v/\omega$ where ω is the laser frequency. Depending on the specific plasma conditions, the ratio $b_{max}/b_{min} \propto v^2$ or $b_{max}/b_{min} \propto v^3$. Taking the derivative of Eq. 5.3 for a proportionality constant c yields the term $\frac{d}{dv}(\ln(\sqrt{1+cv^\beta})) \propto v^{\beta-1}/(v^\beta + c^{-1})$. Introducing a dimensionless parameter u and defining $\eta \equiv c^{-1}$, we arrive at the 'Coulomb integral':

$$I = \int_0^\infty \frac{e^{-u^m}\, u^{\beta-1}}{u^\beta + \eta}\, du, \tag{5.4}$$

5.3 Rewriting the integral

The first step involves rewriting the exponential function appearing in Eq. 5.4 using the Cahen–Mellin integral representation of the exponential function,[138] $e^{-x} = (2\pi i)^{-1}\int_L \Gamma(s)\, x^{-s}\, ds$. The path L is a vertical line in the complex s-plane, lying within the fundamental strip $0 < \Re(s) < \beta/m$, which ensures absolute convergence of the Mellin transform and justifies the interchange of the order of integration in Eq. 5.5. Introducing the scaled variable $t = \eta^{-1/\beta}u$ and defining $\lambda = \eta^{m/\beta}$, we can re-write Eq. 5.4 in the form

$$\begin{aligned} I &= \int_0^\infty \frac{t^{\beta-1}}{t^\beta+1}\left[\frac{1}{2\pi i}\int_L \Gamma(s)\,\lambda^{-s}t^{-ms}\, ds\right] dt \\ &= \frac{1}{2\pi i}\int_L \Gamma(s)\,\lambda^{-s}\left[\int_0^\infty \frac{t^{\beta-1-ms}}{t^\beta+1}\, dt\right] ds. \end{aligned} \tag{5.5}$$

The inner integral is a Beta-type integral[139] $\int_0^\infty t^{w-1}dt/(t^\beta+1) = \beta^{-1}\Gamma(w/\beta)\Gamma(1-w/\beta) = (\pi/\beta)\csc(\pi w/\beta)$, where we define w such that $w-1 \equiv \beta - 1 - ms$. We note that the identity is only valid if $0 < w < \beta$. We can therefore rewrite Eq. 5.5 in the following form:

$$\begin{aligned} I &= \frac{1}{2\pi i}\int_L \frac{\pi}{\beta}\Gamma(s)\,\lambda^{-s}\csc\left(\frac{\pi ms}{\beta}\right) ds \\ &= \frac{1}{2\pi i}\int_L \frac{1}{\beta}\Gamma(ms/\beta)\Gamma(1-ms/\beta)\Gamma(s)\,\lambda^{-s} ds, \end{aligned} \tag{5.6}$$

where we used the identity $\sin(\pi(1 - ms/\beta)) = \sin(\pi ms/\beta)$. The contour-integration method relies on the fact that the relevant Mellin–Barnes integrand is meromorphic (smooth with poles) when the integral runs over the full interval $[0, \infty)$. In that case, the inner integral reduces to a complete Beta-function factor, which may be rewritten in terms of gamma functions or the cosecant. The inner integral only has isolated poles in the Mellin variable s. We will see that the residue theorem converts the contour integral into a sum over the residues of these poles. If, however, the integration range is truncated at an intermediate point, the same step produces incomplete Beta functions rather than a complete Beta function. Their analytic continuation generally introduces branch points and branch cuts. The contour deformation is then no longer determined solely by residues, and branch-cut contributions need to be accounted for. For this reason, the clean residue-sum representation available for the full $[0, \infty)$ integral does not extend to integrals with intermediate limits (which would be of physical interest, since $b_{max} = \min(\lambda_D, b_\omega(v))$, so segmenting the integral would be appropriate).

In Fig. 5.1(a) we show the regions in the complex plane where the integrand in Eq. 5.6 has isolated poles arising from the gamma and cosecant factors, and in Fig. 5.1(b) we plot the modulus of the integrand of Eq. 5.6 for $m = 4$, $\beta = 2$, and $\lambda = 0.1$. For $0 < \eta < 1$, the factor λ^{-s} ensures exponential decay of the integrand in the left half-plane, while $\Gamma(s)$ provides additional decay along vertical lines. Consequently, the contribution from the large semicircular arc vanishes when the contour is closed to the left. Since the integrand is analytic inside the contour except at isolated poles, and no branch cuts are present, the residue theorem applies, and the integral reduces to a sum over the enclosed poles.

5.4 Small-η expansion

Our goal now is to evaluate Eq. 5.6 for conditions encountered in a laser-plasma. Recall that we defined $\lambda = \eta^{m/\beta} = (1/c)^{m/\beta}$. The limit of large c (*i.e.*, $c \gg 1$) is precisely the regime in which the standard Coulomb logarithm picture is valid. It corresponds to a strong separation between the maximum and minimum impact parameters. Therefore we choose to expand around the small parameter η.

To determine the small-η expansion we examine the enclosed poles from the integrand in Eq. 5.6: $\Gamma(s)$ has simple poles located at all non-positive integers: $0, -1, -2, \ldots$ The cosecant poles are also simple and are located at $s = \beta z/m$ where $z \in \mathbb{Z}$. The value of the integral is thus given by the sum of the residues of all poles satisfying $\Re(s) \leq 0$. Since we are treating the double pole at $s = 0$ separately, we will be considering $\Re(s) < 0$ in the case of the gamma and cosecant poles. We assume that β/m is irrational, such that the integral only involves simple poles, but we will see that the argument holds for rational values as well.

There is one double pole at $s = 0$; we insert $\lambda^{-s} = \eta^{-ms/\beta}$ and do a Laurent expansion:

$$\frac{\pi}{\beta}\Gamma(s)\eta^{-ms/\beta}\csc(\pi ms/\beta) \approx \frac{1}{m}\frac{1}{s^2} - \left(\ln(\eta^{m/\beta}) + \gamma\right)\frac{1}{m}\frac{1}{s} + \mathcal{O}(s^0), \tag{5.7}$$

where γ denotes the Euler–Mascheroni constant. The residue of a double pole is the coefficient of the $1/s$ term; hence the contribution of the double pole is (exactly)

$$I_0 = -\frac{1}{\beta}\ln\eta - \frac{\gamma}{m}. \tag{5.8}$$

For typical IBA conditions, this leading order is a very accurate approximation, and for that reason we can neglect the higher-order terms in Chapter 4. To calculate the poles of $\Gamma(s)$, we use the fact that the residue of the gamma function is given by[140] $\mathrm{Res}_{s=-n}\ \Gamma(s) = (-1)^n/n!$. Summing over the poles with $\Re(s) < 0$ gives the series

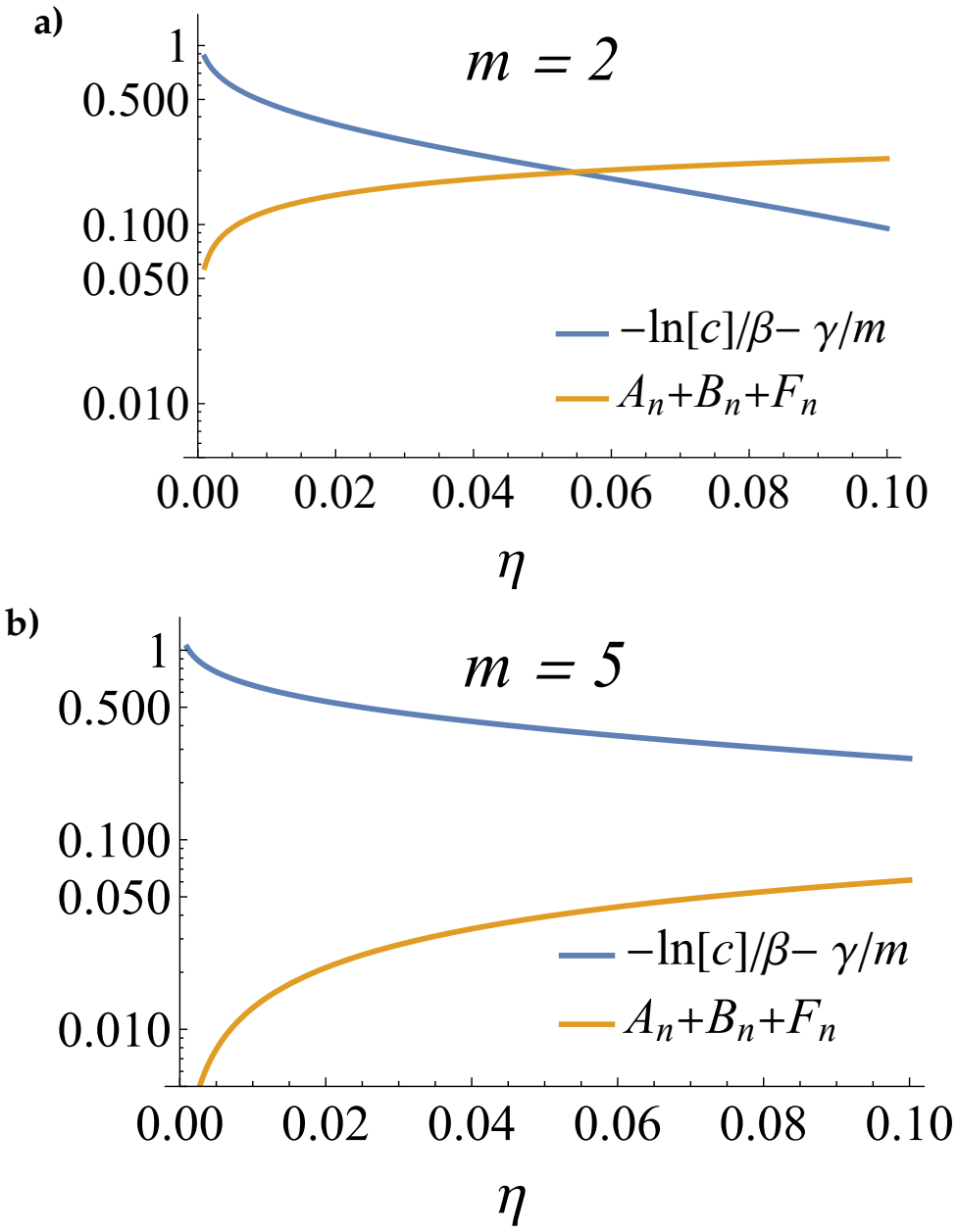


Figure 5.2: $I_0 = -\frac{1}{\beta}\ln\eta - \frac{\gamma}{m}$ together with the sum of all higher-order corrections, plotted as a function of η for $\beta = 6$. The two extreme cases are shown: a) $m = 2$ and b) $m = 5$.

$$\begin{aligned}&\sum_{n=-1}^{-\infty}\frac{(-1)^n}{(-n)!}\frac{\pi}{\beta}\eta^{-nm/\beta}\csc\left(\pi nm/\beta\right)\\&=\sum_{n=1}^{\infty}\frac{(-1)^n}{n!}\frac{-\pi}{\beta}\eta^{nm/\beta}\csc\left(\pi nm/\beta\right).\end{aligned}\tag{5.9}$$

To calculate the poles of the cosecant term, we use the fact that the residue of the cosecant function is given by $\mathrm{Res}_{s=n\beta/m}\csc(\pi ms\beta^{-1}) = (-1)^n\beta/(m\pi)$. The poles are located at $s = \beta z/m$, where $z \in \mathbb{Z}\setminus\{0\}$. We are left with the following summation:

$$\begin{aligned}&\sum_{n=-1}^{-\infty}(-1)^n\frac{\beta}{m\pi}\frac{\pi}{\beta}\Gamma(\beta n/m)\eta^{-n}\\&=\sum_{n=1}^{\infty}(-1)^n\frac{1}{m}\Gamma(-\beta n/m)\eta^n.\end{aligned}\tag{5.10}$$

Finally, we obtain a perturbative solution of the integral first defined in Eq. 5.5:

$$\begin{aligned}I = &-\frac{1}{\beta}\ln\eta-\frac{\gamma}{m}\\&+\sum_{n=1}^{\infty}\Big[-\frac{(-1)^n}{n!}\frac{\pi}{\beta}\eta^{nm/\beta}\csc(\pi nm/\beta)\\&\qquad+(-1)^n\frac{1}{m}\Gamma(-\beta n/m)\eta^n\Big].\end{aligned}\tag{5.11}$$

Note that this derivation strictly holds only when β/m is irrational; otherwise, one must take into account the presence of double poles at locations other than $s = 0$. Although the residue expansion is simplest for irrational values of β/m, the underlying integral defining I is analytic in m. Intuitively, since there is always a rational number in an arbitrarily small neighbourhood of an irrational number, and the function is continuous, the solutions for rational and irrational β/m can in the limit be taken arbitrarily close to one another. The apparent divergences in Eq. 5.11 arise from separate contributions that individually diverge but converge together; regrouping allows one to cancel the divergent terms with a finite remainder, as we will show below. To cancel out the divergent terms, we first define:

$$\begin{aligned}A_n(m) &\equiv -\frac{(-1)^n}{n!}\frac{\pi}{\beta}\eta^{nm/\beta}\csc(\pi nm/\beta)\\B_n(m) &\equiv (-1)^n\frac{1}{m}\Gamma(-\beta n/m)\eta^n.\end{aligned}\tag{5.12}$$

For a given m, the poles of A_n are located where nm/β is an integer; the values of n for which A_n and B_n diverge are given by

$$n_A \equiv \frac{\beta z}{\gcd(m,\beta)}, \quad n_B \equiv \frac{mz}{\gcd(m,\beta)}, \quad z \in \mathbb{Z}^+ \tag{5.13}$$

respectively, where gcd is the greatest common divisor (see the Appendix for the definition in the case of $m \in \mathbb{Q}$, $\beta \in \mathbb{Q}$). We decompose Eq. 5.11 into convergent and divergent contributions:

$$I = -\frac{1}{\beta}\ln\eta - \frac{\gamma}{m}\sum_{n\notin n_A} A_n + \sum_{n\notin n_B} B_n + \sum_{n\in n_A} A_n + \sum_{n\in n_B} B_n. \tag{5.14}$$

To align the values of n for which A_n and B_n diverge, we write

$$\sum_{n\in n_A} A_n + \sum_{n\in n_B} B_n = \sum_{n\in n_A} A_n + B_{\frac{nm}{\beta}}. \tag{5.15}$$

Here n is the index from n_A, and the corresponding divergent indices of B_n are generated by the bijection $n_B = mn_A/\beta$. We regularize the coincident poles by replacing m with $m+s$ and expanding for s around 0. The Laurent expansion of the cosecant function about an integer pole is

$$\csc\big(\pi(s-n)\big) = \frac{(-1)^n}{\pi s} + \mathcal{O}(s). \tag{5.16}$$

Applying this expansion to $A_n(m+s)$ yields

$$A_n(m+s) = \frac{(-1)^n(-\eta)^{\frac{mn}{\beta}}}{n!}\left[\frac{1}{s}\frac{1}{n} + \frac{\ln\eta}{\beta} + \mathcal{O}(s)\right], \tag{5.17}$$

where the logarithmic term arises from expanding $\eta^{n(m+s)/\beta}$ about $s = 0$. The Laurent expansion of the gamma function about a negative integer is

$$\Gamma(s-n) = \frac{(-1)^n}{n!}\left[\frac{1}{s} - \gamma + H_n\right] + \mathcal{O}(s), \tag{5.18}$$

where H_n is the n^{th} harmonic number. Note that $\lim_{n\to\infty}(H_n - \ln(n)) = \gamma$. Inserting this, the corresponding expansion of the paired term $B_{n_B}(m+s)$, with $n_B = mn/\beta$, becomes

$$B_n(m+s) = \frac{(-1)^n(-\eta)^{\frac{mn}{\beta}}}{n!}\left[-\frac{1}{s}\frac{1}{n} - \frac{H_n - \gamma}{m} + \mathcal{O}(s)\right], \tag{5.19}$$

where $n \in n_A$. See the Appendix for the first-order corrections of A_n and B_n. As expected, the $1/s$ divergences cancel exactly between A_n and B_n, leaving the finite remainder

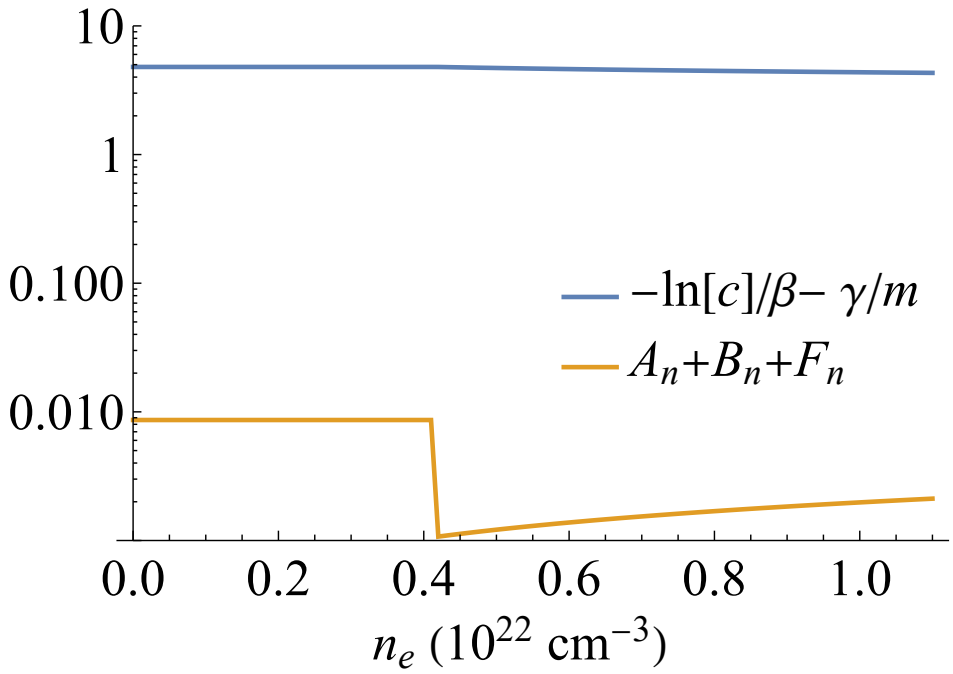


Figure 5.3: The first-order term I_0 and the sum of the higher-order terms, evaluated using parameters from the experiment of Shang *et al.*,[129] which yield $m \approx 2.90$ and a critical density of $n_{e,c} = 9.05 \times 10^{21}\,\mathrm{cm}^{-3}$. The discontinuity at $n_e = 4.19 \times 10^{21}\,\mathrm{cm}^{-3}$ is caused by the transition between the $\beta = 6$ and $\beta = 4$ regimes. The maximum density in the scan is based on the experimental number density, $n_e = 1.10 \times 10^{22}\,\mathrm{cm}^{-3}$.

$$F_n = \frac{(-1)^n(-\eta)^{\frac{nm}{\beta}}}{m\,n!}\left[\frac{m}{\beta}\ln\eta - H_n + \gamma + \mathcal{O}(s)\right], \quad n \in n_A. \tag{5.20}$$

Therefore, after properly accounting for all coincident poles, the analytically continued expression for I becomes

$$I = -\frac{1}{\beta}\ln\eta - \frac{\gamma}{m} + \sum_{n\notin n_A} A_n + \sum_{n\notin n_B} B_n + \sum_{n\in n_A} F_n. \tag{5.21}$$

See Fig. 5.2 for a comparison of I_0 with all higher-order terms as a function of η. We show the extreme values $m = 2$ and $m = 5$ for $\beta = 6$.

As discussed in Chapter 4, the most relevant values of η in laser-driven plasmas are $\eta < 0.01$. This is because, for the impact parameters considered there, $\eta \propto n_e Z_{\mathrm{eff}}^2 T_e^{-3}\alpha_e^{-4}$ when $\beta = 4$, and $\eta \propto Z_{\mathrm{eff}}^{-2} T_e^{-3}\alpha_e^{-6}\lambda_{\mathrm{las}}^{-2}$ when $\beta = 6$. Here, α_e is a mildly monotonically increasing function of m, n_e is the electron number density, T_e is the electron temperature, Z_{eff} is the effective charge state, and λ_{las} is the laser wavelength. Using the approximate scaling $Z_{\mathrm{eff}} \propto T_e^{0.6}$, large values of η require high n_e, short laser wavelengths, and (most importantly) low-temperature plasmas. However, the regions of the plasma where IBA occurs are typically the hottest. Therefore, in Chapter 4, we only consider I_0, and discard the higher-order

terms. To illustrate the validity of this approximation, we apply these results to laser-driven gold plasmas studied by Shang *et al.*;[129] see Fig. 5.3 where $T_e = 1000$ eV, $\rho = 0.08$ g/cm^3, $Z_{\text{eff}} = 45$ on the basis of a calculation performed with FLYCHK,[141] $\lambda_{\text{las}} = 0.351\,\mu$m, and $I_{\text{las}} = 3 \times 10^{14}\,\text{W}\,\text{cm}^{-2}$. This yields an electron destiny of $n_e = 1.10 \times 10^{22}\,\text{cm}^{-3}$ and a critical density of $n_e = 9.05 \times 10^{21}\,\text{cm}^{-3}$. For these parameters, at the critical density, the thermal Coulomb logarithm predicts $\ln(\lambda_D/b_{\perp t}) \approx 3.64$, whereas the actual value $I_0 \approx 4.41$. Thus, the thermal Coulomb logarithm underestimates the result by approximately 18%. Note that this is *before* applying the Langdon reduction factor (which here is 0.64) so the total absorptivity is still lower than if the Langdon effect were not accounted for; but properly solving the Coulomb integral I mitigates this decrease somewhat.

5.5 Conclusion

In this work, we have presented a systematic analytic treatment of a family of integrals I motivated by the kinetic theory of inverse bremsstrahlung absorption in plasmas with super-Gaussian electron distributions due to the Langdon effect. This family comprises arbitrary values of the super-Gaussian parameter m, as well as arbitrary values of the power β, representing different physical distances for b_{max}. The final result, Eq. 5.21, is an expansion in terms of the dimensionless parameter η.

The leading term, $-\frac{1}{\beta}\ln\eta - \gamma/m$, provides a simple, closed-form approximation that captures the small-η regime, while the extra terms A_n and B_n provide the systematic corrections when higher accuracy is required. In deriving these extra terms, we explicitly cancel the divergent terms in A_n and B_n and collect the finite remainder into the terms of F_n. Finally, we show in the Appendix that I can be expressed in terms of a Meijer G-function. We also provide next-order terms for values of m near divergences, to avoid numerical instabilities.

In current plasma codes, the Langdon effect is still often overlooked. With these results, the physical effects of super-Gaussian EDFs can be evaluated in a relatively simple and straightforward manner. In fact, the leading term I_0 differs from the thermal Coulomb logarithm only by an m-dependent term; nevertheless, we show that this term can significantly alter the Coulomb logarithm value, thereby affecting physical plasma quantities such as absorptivity and thermal conduction.

Acknowledgments

This work has been carried out at the Advanced Research Center for Nanolithography (ARCNL). ARCNL is public–private partnership with founding partners UvA, VU, NWO-I and ASML, and associate partner RUG. This work was (partly) financed by "Toeslag voor Topconsortia voor Kennis en Innovatie (TKI) from the Dutch Ministry of Economic Affairs." This publication is part of the project ARIES with file number 20152 of the research programme VENI which is (partly) financed by the Dutch Research Council (NWO) under an NWO grant.

5.6 Appendix

Here we provide an exact representation of the integral I in terms of a Meijer G-function for rational m. The Meijer G-function is commonly defined as[142]

$$G_{p,q}^{\mu,\nu}\left(\begin{matrix}a_1,\ldots,a_p\\ b_1,\ldots,b_q\end{matrix}\,\middle|\, z\right) \equiv \frac{1}{2\pi i}\int_L \frac{\prod_{j=1}^{\mu}\Gamma(b_j-s)\prod_{j=1}^{\nu}\Gamma(1-a_j+s)}{\prod_{j=\mu+1}^{q}\Gamma(1-b_j+s)\prod_{j=\nu+1}^{p}\Gamma(a_j-s)}\,z^s\,ds, \tag{5.22}$$

with the caveat that $a_k - b_j \neq 1,2,3,\ldots$ for any combination of k,j for which $k = 1,2,\ldots,\nu$, and $j = 1,2,\ldots,\mu$. This integral is of the Mellin–Barnes type, and may be viewed as an inverse Mellin transform, just like the integral under our consideration. a_p and b_q are lists of parameters with finite length, for example:

$$G_{2,2}^{1,1}\left(\begin{matrix}1,\,2\\ 3,\,2\end{matrix}\,\middle|\, z\right) = \frac{1}{2\pi i}\int_L \frac{\Gamma(3-s)\,\Gamma(1-1+s)}{\Gamma(1-2+s)\,\Gamma(2-s)}\,z^s\,ds. \tag{5.23}$$

In the present case, all gamma factors occur in the numerator, so $\mu = q$ and $\nu = p$. Hence the Meijer G-function reduces to

$$G_{p,q}^{q,p}\left(\begin{matrix}a_1,\ldots,a_p\\ b_1,\ldots,b_q\end{matrix}\,\middle|\, z\right) = \frac{1}{2\pi i}\int_L \left[\prod_{j=1}^{q}\Gamma(b_j-s)\right]\times\left[\prod_{j=1}^{p}\Gamma(1-a_j+s)\right] z^s\,ds. \tag{5.24}$$

We rewrite the gamma functions $\Gamma(s)\Gamma(ms/\beta)\Gamma(1-ms/\beta)$ in the form of $\Gamma(b_j-s)\Gamma(1-a_j+s)$. For this purpose we make use of the Gauss multiplication formula:[143]

$$\Gamma(nz) = (2\pi)^{\frac{1-n}{2}}\,n^{nz-\frac{1}{2}}\prod_{k=0}^{n-1}\Gamma\left(z+\frac{k}{n}\right). \tag{5.25}$$

Since this formula applies only for integer values of n, we write $m = a/b$ with $a,b \in \mathbb{Z}^+$, and choose b such that $\beta b \in \mathbb{Z}^+$ (which is always possible for a $\beta \in \mathbb{Q}$ with an appropriate choice of b). Making use of the substitution $s = \beta b t$, we may then apply the multiplication formula with $n = a$ and $n = \beta b$, after which we apply the Gauss multiplication formula to $\Gamma(at)$, $\Gamma(1-at)$ and $\Gamma(\beta b t)$ from Eq. 5.6. In the case of $1-at$, we use the multiplication formula with $n = a$ and $z = 1/a - t$.

$$\begin{aligned} I = \frac{1}{2\pi i}\int_L b\lambda^{-\beta b t}&\left[(2\pi)^{\frac{1-a}{2}}\,a^{at-\frac{1}{2}}\prod_{k=0}^{a-1}\Gamma\left(t+\frac{k}{a}\right)\right]\\ \times&\left[(2\pi)^{\frac{1-a}{2}}\,a^{a(1/a-t)-\frac{1}{2}}\times\prod_{k=0}^{a-1}\Gamma\left((1/a-t)+\frac{k}{a}\right)\right]\\ \times&\left[(2\pi)^{\frac{1-\beta b}{2}}\,(\beta b)^{\beta b t-\frac{1}{2}}\prod_{k=0}^{\beta b-1}\Gamma\left(t+\frac{k}{\beta b}\right)\right]dt. \end{aligned} \tag{5.26}$$

Collecting terms and substituting $\lambda = \eta^{m/\beta} = \eta^{a/(\beta b)}$,

$$
\begin{aligned}
I = & \frac{1}{2\pi i}\sqrt{\frac{b}{\beta}}(2\pi)^{3/2-a-\beta b/2} \\
& \times \int_L \left[(\beta b)^{\beta b}\eta^{-a}\right]^t \left[\prod_{k=0}^{a-1}\Gamma\left(t+\frac{k}{a}\right)\right] \\
& \times \left[\prod_{k=0}^{a-1}\Gamma\left(1/a-t+\frac{k}{a}\right)\right]\left[\prod_{k=0}^{\beta b-1}\Gamma\left(t+\frac{k}{\beta b}\right)\right] dt.
\end{aligned}
\tag{5.27}
$$

Comparing the expression above with the Meijer G-function, we identify the following relation in the case of $\beta \in \mathbb{Q}$, $m \equiv a/b \in \mathbb{Q}$, where a and b should be multiplied by an integer such that $\beta b \in \mathbb{Z}^+$:

$$
I = \sqrt{\frac{b}{\beta}}\,(2\pi)^{3/2-a-\beta b/2} \times G^{a,\,a+\beta b}_{a+\beta b,\,a}\left(\begin{matrix}\frac{1}{a},\frac{2}{a},\ldots,1,\,\frac{1}{\beta b},\frac{2}{\beta b},\ldots,1\\ \frac{1}{a},\frac{2}{a},\ldots,1\end{matrix}\,\middle|\,(\beta b)^{\beta b}\eta^{-a}\right). \tag{5.28}
$$

The product $\prod_{k=0}^{a-1}\Gamma(1/a-t+k/a)$ yields the lower parameters $1/a, 2/a, \ldots, 1$ The remaining two products, $\prod_{k=0}^{a-1}\Gamma(t+k/a)$, $\prod_{k=0}^{\beta b-1}\Gamma(t+k/(\beta b))$, yield the upper parameters.

In the above, we have shown that the Meijer G-function provides a valid solution for rational m.

In practice, retaining higher-order terms (A_n and B_n) may be useful to improve accuracy, as the poles may lead to numerical instability. It is then useful to retain the first-order terms in the Laurent expansions of the colliding contributions. The first order correction for $A_n(m+s)$ from Eq. (5.17) with the prefactor omitted is

$$
-s\frac{n\left(6\log^2(\eta)+2\pi^2\right)}{12\,\beta^2}+\mathcal{O}\left(s^2\right). \tag{5.29}
$$

The first-order correction for $B_n(m+s)$ from Eq. 5.19 with the prefactor omitted is

$$
-s\,\frac{-3n\left(H_n-\gamma\right)^2+6\left(H_n-\gamma\right)+3n\left(\frac{\pi^2}{6}-H_n^{(2)}\right)-\pi^2 n}{6m^2}+\mathcal{O}\left(s^2\right), \tag{5.30}
$$

where $H_n^{(2)}$ is the harmonic number of order 2: $H_n^{(2)} = \sum_{k=1}^{n} k^{-2}$. The first-order correction to $F_n(m+s)$ is just the sum of Eq. 5.29 and Eq. 5.30.

For two rational numbers r_1 and r_2, their greatest common divisor is defined as

$$
\gcd(r_1,r_2) = \max\left\{r\in\mathbb{Q}\;\middle|\;\frac{r_1}{r}\in\mathbb{Z}\text{ and }\frac{r_2}{r}\in\mathbb{Z}\right\}. \tag{5.31}
$$

Equivalently, writing $r_1 = a_1/b_1$ and $r_2 = a_2/b_2$ with $a_1, a_2 \in \mathbb{Z}$ and $b_1, b_2 \in \mathbb{N}$, where r_1 and r_2 are fully reduced, one has

$$\gcd(r_1, r_2) = \frac{\gcd(a_1, a_2)}{\mathrm{lcm}(b_1, b_2)}, \tag{5.32}$$

where lcm is the least common multiple.

Chapter 6

Conclusion & Outlook

6.1 Summary

Good research is cyclical: it builds upon previous works and inspires others in kind. The roots of this thesis lie in the work of my predecessor, Dr. Diko Hemminga. By performing laser wavelength scans for laser–droplet simulations, he found that conversion efficiency could be increased if a laser of 2 µm wavelength were used instead of the current 10.6 µm.[72] In the outlook of his thesis, he briefly discussed a simulation of a tin droplet irradiated with a 2 µm long pulse; a more complete investigation was left to future work.

That future work became Chapter 2 of this thesis. The goal was to provide a broad overview of the physics of the laser–droplet system within the proposed 2 µm long pulse irradiation scheme. It would, in essence, explore its promises and challenges before conducting experiments in a laboratory setting. Most importantly, we found that the EUV energy produced in this scheme is on the order of tens of millijoules per shot. At a laser intensity of 0.7×10^{11} W cm^{-2} (the CE-optimal intensity) and a droplet diameter of 30 µm, we find that 19 mJ of EUV is emitted in the direction of the collector mirror and is therefore usable in the lithography process. This yield is increased to 28 mJ by using an intensity of 1.4×10^{11} W cm^{-2} at a marginal loss in CE. With larger droplets, even higher energies are reached, with a 45 µm diameter droplet providing 101 mJ for a 1.4×10^{11} W cm^{-2} intensity laser. These results are competitive with experimental EUV-per-shot values for pre-pulsed targets, such as the 12.5 mJ reported by Mostafa *et al.*,[70] also using a 2 µm-wavelength pulse, and the 10 mJ reported by Reuters,[38] driven by a CO_2 laser.

As the droplet is irradiated by the laser light, an EUV-emitting plasma is formed in front of the droplet. Over the course of >100 ns of steady irradiation, the droplet continuously loses mass due to ablation, until it is finally fully vaporized. This ablation causes the droplet (and thereby the EUV source) to move along the laser axis by 0.5–1 mm, depending on the droplet size. Generally, three-quarters of the EUV energy is produced over the first half of this distance. Ablation rate and vaporization time are shown to be power-law functions of laser intensity. To understand the motion of the droplet, we proposed a simple 'rocket propulsion' model, which incorporates the ablation rate to predict the droplet position as a function of time.

Ion emissions are another practical point of concern, and this matter is explored in Chapter 3. We considered two cases: the 'long pulse' scheme identical to the one studied in the previous work, and a 'short pulse' scheme (27 ns pulse length). The ion kinetic energy

spectrum from the 'long pulse' is characterized by a narrow peak, as the steady state plasma generates an ion outflux of a near-constant kinetic energy. As the droplet is fully vaporized, virtually all ions are emitted in this manner. This is notably different from the 'short pulse': as the laser intensity falls, a droplet remnant persists, and ions of lower energies are emitted and detected.

The peak kinetic energy E_{peak} is the strongest at 0°—facing the laser—and decreases for larger angles. The number of ions emitted per solid angle, $dNd\Omega^{-1}$, is mostly constant up to 60°, and then increases. This is attributed to a secondary tin outflux due to the expansion of the highly-deformed droplet at late times. Due to the peakedness of the spectrum, we find that the angular energy emission $dEd\Omega^{-1}$ can be calculated from the product of E_{peak} and $dNd\Omega^{-1}$. We also derived a scaling law for E_{peak} as a function of laser intensity in the range 0.7–3.5 $\times$ 10^{11} W cm^{-2}, though this scaling is angle-dependent.

Chapter 4 presents a theoretical analysis of laser absorption in a plasma. Absorptivity depends on the Coulomb logarithm $\ln\Lambda(v)$, and in plasma calculations v is commonly assumed to be thermal, *i.e.* $v = v_t$, instead of considering the full electron velocity distribution. Following the work of Sherlock *et al.*[106], we assume a super-Gaussian EDF as described by the Langdon effect, and compute $\ln\Lambda$ by integrating over all v. We conducted an extensive analysis of the relevant impact parameters that define the Coulomb logarithm. For the plasmas considered, the absorption is mostly defined by the impact parameter $b_{max} = b_\omega \equiv v/\omega_{\text{laser}}$; the Debye length is relevant for absorption in underdense plasmas: $b_{max} = \lambda_D$. We obtained a simple perturbative formula for the absorptivity, which can easily be implemented into numerical codes. The first-order term is generally sufficiently accurate, and higher-order terms can be retained if this is not the case, for example for plasmas driven by short laser wavelengths. This formula typically leads to a notable change in the value of $\ln\Lambda$, such as the ICF case where we find it to be 30% lower compared to the standard thermal Coulomb logarithm. Integration of the Coulomb logarithm has thereby somewhat mitigated the absorption reduction due to the Langdon factor. Nevertheless, this new formula leads to a significant decrease in laser absorptivity, which means the laser can penetrate deeper and change the temperature distribution of the plasma. This, in turn, changes our understanding of radiative behaviour: we may find that the plasma is *hotter* than current models predict, and that the hot spot is located deeper, resulting in more reabsorption. In both of these aspects, the plasma would be less efficient than predicted by the models.

A general form of the Coulomb integral is derived in detail in Chapter 5. By using the Cahen–Mellin representation of the exponential factor and solving the Beta-type integral, one finds a contour integral in the complex plane. By summing over the residues of the poles on the negative real axis, consecutive terms of the integral are obtained. The first-order term is given by the double pole at the origin. If the parameter m is rational, the integral can be written as a Meijer G-function; these also have a perturbative form, where the double (*i.e.*, overlapping) poles require special treatment. If the generic formula for irrational m is used for rational values, such as $m = 2$, the expansion contains divergent terms. It is therefore recommended that a first-order Laurent expansion in m is performed in the vicinity of these values, such that the divergent terms cancel and the formula is well-behaved.

6.2 Outlook

The two simulation-focused Chapters, 2 and 3, have made promising strides in exploring the feasibility of a 2 µm long pulse source. Now that these initial results are in, progress can best be made in the lab. The first challenge is, of course, to set up a stable 2 µm-wavelength laser that can generate pulses long enough to fully vaporize tin microdroplets. Then, there will be two goals. The first is to confirm the main findings of these two works. Ion emission for the 'short pulse' case can be benchmarked to an optical parametric oscillator laser as proposed in Chapter 3. By validating the accuracy of quantities like the predicted peak ion kinetic energy, total ion numbers, and EUV yield, a better picture can be made before experimentally investigating the 'long pulse' case. Simulated results like vaporization time and droplet motion (vaporization distance) can also be checked. If discrepancies are found, one may turn to a closer study of ablation dynamics and droplet deformation—for example by using the hydrodynamics code `Basilisk`.[144]

The second goal is to optimize the source within the realm of practical constraints. In this, an experimental proof-of-concept will face several challenges. A >100 ns irradiation time is much longer than is the current practice, and the beam must stay stable and on-target to fully vaporize the droplet. Droplet motion, for its part, has two consequences. First, it increases the effective size of the source along the z-axis, which affects the source étendue. Second, the system is constrained by the *Rayleigh length*, *i.e.*, the characteristic distance over which the beam radius increases. As the droplet moves, it will therefore be irradiated by a more spread-out beam, and light will increasingly miss the droplet. Optimal EUV production therefore becomes a matter of precise engineering, and parameters such as droplet size must be tuned accordingly.

In Chapter 4, we considered laser absorption in a plasma in the presence of the Langdon effect, using a gadolinium plasma as an example. The concept of a gadolinium plasma for beyond-EUV light production is still in a very early stage, and radiation-hydrodynamic simulations may be of use to explore its feasibility in terms of source design. For such plasmas, it is not uncommon to find super-Gaussian parameter values $m > 3$, especially for lasers of longer wavelengths such as the CO_2 laser. With the Coulomb integral formula, laser absorption will be lower, resulting in changes to plasma properties discussed above. These effects are yet to be quantified, and comparing simulations using the old and new Coulomb logarithm formulas one-to-one will be instructive. Furthermore, a super-Gaussian EDF will affect the rates of the different collisional processes, which affects plasma properties such as the pressure and the average charge state; these may be expected to deviate from equilibrium values. This is at odds with the LTE assumption of hydrodynamic codes like `RALEF-2D`, and, as such, high-m laser-produced plasmas could face significant discrepancies.

Pain and Benredjem[145] proposed formulas for the electron-impact excitation rate for non-LTE plasmas. It would be illustrative to compare rates for plasmas with super-Gaussian velocity distributions of various m to the familiar Maxwellian case. From there, a wider study into non-LTE physics can be launched. Finally, the theoretical results of this investigation can be implemented in rad-hydro codes. However, a detailed numerical treatment of super-Gaussian plasmas may face practical constraints: `RALEF-2D` already relies on large lookup tables for EOS variables and radiative properties. If no simple m-dependent adjustment formula can be found, treating m as another input parameter would enlarge such tables further.

List of Publications

CHAPTER 2
S. J. J. de Lange, D. J. Hemminga, Y. Mostafa, R. A. Meijer, O. O. Versolato, and J. Sheil, *Modeling the hundreds-of-nanoseconds-long irradiation of tin droplets with a 2 µm-wavelength laser for future EUV lithography*, Plasma Sources Sci. Technol., **33**, 105003 (2024).

CHAPTER 3
S. J. J. de Lange, J. Gonzalez, D. J. Engels, F. M. Kohlmeier, and J. Sheil. *Ion emission properties of tin plasmas generated by 2 µm-wavelength laser pulses*, Plasma Sources Sci. Technol., **34**, 125013 (2025).

CHAPTER 4
S. J. J. de Lange, B. Brewster, and J. Sheil. *A refined model for laser absorption in plasmas involving the Langdon effect*, Submitted for publication.

CHAPTER 5
B. Brewster, **S. J. J. de Lange**,* and J. Sheil. *Super-Gaussian integration for the Langdon effect*, In preparation.

I

The author has also contributed to the following publications:

S. J. J. de Lange, J. Sheil, O. O. Versolato, M. A. Purvis, and D. J. W. Brown. *EUV radiation generating method*, WO Patent WO2025201792A1 (2025).

K. Mongey, **S. J. J. de Lange**,* R. Brady, Diko J. Hemminga, B. Delaney, Mikhail M. Basko, E. Sokell, F. O'Reilley, and John Sheil. *Characterization of experimental and simulated micrometer-scale soft x-ray-emitting laser plasmas: Toward predictive radiance calculations*, Appl. Phys. Lett., **124**, 102104 (2024).

S. Aggarwal, **S. J. J. de Lange**,† and J. Sheil. *Thermal conduction in laser-driven tin plasmas and the sensitivity of plasma properties to the flux limiter*, Submitted for publication.

*Contributions to these works include supporting the investigation, methodology, software, visualization, and writing.
†Contributions to this work include supporting simulations design, interpretation of data, and presentation of results.

Bibliography

[1] X. Fan, T. G. Myers, B. A. D. Sukra, and G. Gabrielse, Measurement of the electron magnetic moment, Phys. Rev. Lett. **130**, 071801 (2023).

[2] Sir G. I. Taylor, The formation of a blast wave by a very intense explosion. I. Theoretical discussion, Proc. R. Soc. Lond. A. **201**, 159–174 (1950).

[3] Sir G. I. Taylor, The formation of a blast wave by a very intense explosion. II. The atomic explosion of 1945, Proc. R. Soc. Lond. A. **201**, 175–186 (1950).

[4] A. H. Foundation, Fireball, `https://www.atomicarchive.com/media/photographs/trinity/fireball-1.html` (2024), accessed: 24–03–2026.

[5] A. H. Foundation, Fireball, `https://www.atomicarchive.com/media/photographs/trinity/fireball-3.html` (2024), accessed: 24–03–2026.

[6] Y. Zel'dovich and Y. Raizer, *Physics of Shock Waves and High-Temperature Hydrodynamic Phenomena* (Academic Press, 1966).

[7] G. W. Bluman and S. Kumei, *Symmetries and differential equations* (Springer, 1989).

[8] M. A. Deakin, G.I. Taylor and the Trinity test, Int. J. Math. Educ. Sci. Technol. **42**, 1069–1079 (2011).

[9] D. Salzmann, *Atomic Physics in Hot Plasmas* (Oxford University Press, 1998).

[10] J. Bauche, C. Bauche-Arnoult, and O. Peyrusse, *Atomic Properties in Hot Plasmas* (Springer International Publishing, 2015).

[11] J. Sheil, O. O. Versolato, A. J. Neukirch, and J. Colgan, Multiply-excited states and their contribution to opacity in CO_2 laser-driven tin-plasma conditions, J. Phys. B **54**, 035002 (2021).

[12] F. Chen, *Introduction to Plasma Physics and Controlled Fusion*, 3rd ed. (Springer, 2016).

[13] A. Beck and N. Meyer-Vernet, The trajectory of an electron in a plasma, Am. J. Phys. **76**, 934–936 (2008).

[14] S. Baalrud, K. Ø. Rasmussen, and J. Daligault, Effective potential theory: A practical way to extend plasma transport theory to strong coupling, Contrib. Plasma Phys. **55**, 209–214 (2015).

II

[15] L. Spitzer and R. Härm, Transport phenomena in a completely ionized gas, Phys. Rev. **89**, 977–981 (1953).

[16] F. L. Hinton, *Collisional transport in plasma*, Vol. 1 (North-Holland Publishing Company, 1983) p. 147–197.

[17] A. S. Richardson, *NRL Plasma Formulary*, Tech. Rep. (Naval Research Laboratory, 2019).

[18] S. I. Braginskii, Transport processes in a plasma, Rev. Plasma Phys. **1**, 205 (1965).

[19] G. Mantas, Electron collision frequencies and energy transfer rates, J. Atmos. Terr. Phys. **36**, 1587–1600 (1974).

[20] L. Spitzer, *Physics of Fully Ionized Gases*, 2nd ed. (Interscience, 1962).

[21] S. Chapman and T. G. Cowling, *The Mathematical Theory of Non-Uniform Gases*, 3rd ed. (Cambridge University Press, 1990).

[22] L. D. Landau and E. M. Lifshitz, *Fluid Mechanics*, 2nd ed., Course of Theoretical Physics, Vol. 6 (Butterworth-Heinemann, 1987).

[23] S. Faik, A. Tauschwitz, and I. Iosilevskiy, The equation of state package FEOS for high energy density matter, Comp. Phys. Comm. **227**, 117–125 (2018).

[24] H. Brysk, P. M. Campbell, and P. Hammerling, Thermal conduction in laser fusion, Plasma Physics **17**, 473 (1975).

[25] S. Aggarwal, J. Gonzalez, S. J. J. de Lange, and J. Sheil, Thermal conduction in laser-driven tin plasmas and the sensitivity of plasma properties to the flux limiter, Submitted for publication.

[26] F. Torretti, J. Sheil, R. Schupp, M. M. Basko, M. Bayraktar, R. A. Meijer, S. Witte, W. Ubachs, R. Hoekstra, O. O. Versolato, A. J. Neukirch, and J. Colgan, Prominent radiative contributions from multiply-excited states in laser-produced tin plasma for nanolithography, Nat. Commun. **11**, 2334 (2020).

[27] W. Jarrah, J.-C. Pain, and D. Benredjem, Plasma potential and opacity calculations, High Energy Density Phys. **32**, 8–13 (2019).

[28] Y. Ralchenko, ed., *Modern Methods in Collisional-Radiative Modeling of Plasmas*, Springer Series on Atomic, Optical, and Plasma Physics, Vol. 90 (Springer International Publishing, 2016).

[29] M. M. Basko, V. G. Novikov, and A. S. Grushin, On the structure of quasi-stationary laser ablation fronts in strongly radiating plasmas, Phys. Plasmas **22**, 053111 (2015).

[30] A. B. Langdon, Nonlinear inverse bremsstrahlung and heated-electron distributions, Phys. Rev. Lett. **44**, 575–579 (1980).

[31] ISO 21348:2007, *Space environment (natural and artificial) — Process for determining solar irradiances*, Standard (International Organization for Standardization, Geneva, CH, 2007).

[32] V. Bakshi, ed., *EUV Lithography*, 2nd ed. (SPIE Press, 2018).

II

[33] S. Bajt, J. B. Alameda, T. W. Barbee, Jr., W. M. Clift, J. A. Folta, B. Kaufmann, and E. A. Spiller, Improved reflectance and stability of Mo/Si multilayers, Opt. Eng. **41**, 1797–1804 (2002).

[34] M. Basko, On the maximum conversion efficiency into the 13.5-nm extreme ultraviolet emission under a steady-state laser ablation of tin microspheres, Phys. Plasmas **23**, 083114 (2016).

[35] M. Reitsma, J. Sheil, O. Versolato, E. V. Kahl, and J. C. Berengut, Resolving the blueshift in calculations of the EUV spectrum of multiply charged tin ions, Submitted for publication.

[36] J. Van Schoot, High NA EUVL, in *EUVL and Source Workshop*, 2 (EUV Litho, Inc., 2025).

[37] Q. Zhu, A. A. Schafgans, J. Stewart, S. Rich, M. Purvis, H. Wang, K. Hummler, A. LaForge, P. Mayer, D. Urone, O. Biabani, A. Dorobantu, Y. Ma, and B. Rollinger, Evolution of EUV light source architecture for continued advancements in EUV high volume manufacturing, in *Optical and EUV Nanolithography XXXVIII*, Vol. 13424, edited by M. Burkhardt and C. van Lare, International Society for Optics and Photonics (SPIE, 2025) p. 134240Y.

[38] S. Nellis, Exclusive: ASML unveils EUV light source advance that could yield 50% more chips by 2030, https://www.reuters.com/world/china/asml-unveils-euv-light-source-advance-that-could-yield-50-more-chips-by-2030-2026-02-23/ (2026), accessed: 24–03–2026.

[39] H. Wang, E. G. Champenois, B. Kamerin, K. Post, J. F. M. Keeris, M. Purvis, J. Stewart, S. Rich, K. Hummler, Q. Zhu, A. LaForge, P. Mayer, D. Urone, Y. Ma, B. Rollinger, and A. A. Schafgans, First 1000 W in-band EUV power demonstration using laser-produced plasma technology, in *Optical and EUV Nanolithography XXXIX*, edited by C. van Lare and I. Mochi, International Society for Optics and Photonics (SPIE, 2026) p. 139790J.

[40] I. Tamer, B. A. Reagan, T. Galvin, J. Galbraith, E. Sistrunk, A. Church, G. Huete, H. Neurath, and T. Spinka, Demonstration of a compact, multi-joule, diode-pumped Tm:YLF laser, Opt. Lett. **46**, 5096–5099 (2021).

[41] M. Basko, J. Maruhn, and A. Tauschwitz, RALEF-2D: A 2D hydrodynamic code with heat conduction and radiation transport, RALEF 2D Main Report: http://www.basko.net/mm/RALEF/ralef-main-report.pdf (2017).

[42] F. L. Addessio, J. R. Baumgardner, J. K. Dukowicz, N. L. Johnson, B. A. Kashiwa, R. M. Rauenzahn, and C. Zemach, CAVEAT: A computer code for fluid dynamics problems with large distortion and internal slip (Report No. LA-10613-MS-Rev. 1, UC-32, Los Alamos National Laboratory, 1992).

[43] I. Vichev, A. Solomyannaya, A. Grushin, and D. Kim, On certain aspects of the THERMOS toolkit for modeling experiments, High Energy Density Phys. **33**, 100713 (2019).

[44] D. J. Hemminga, L. Poirier, M. M. Basko, R. Hoekstra, W. Ubachs, O. O. Versolato, and J. Sheil, High-energy ions from Nd:YAG laser ablation of tin microdroplets: comparison between experiment and a single-fluid hydrodynamic model, Plasma Sources Sci. Technol. **30**, 105006 (2021).

II

[45] D. Bleiner, J. Costello, F. Dortan, G. O'Sullivan, L. Pina, and A. Michette, eds., *Short Wavelength Laboratory Sources: Principles and Practices* (The Royal Society of Chemistry, London, 2014).

[46] G. D. O'Sullivan and R. Faulkner, Tunable narrowband soft x-ray source for projection lithography, Opt. Eng. **33**, 3978–3983 (1994).

[47] P. G. Burkhalter, U. Feldman, and R. D. Cowan, Transitions in highly ionized Sn spectra from a laser-produced plasma, J. Opt. Soc. Am. **64**, 1058–1062 (1974).

[48] S. S. Harilal, M. C. Phillips, D. H. Froula, K. K. Anoop, R. C. Issac, and F. N. Beg, Optical diagnostics of laser-produced plasmas, Rev. Mod. Phys. **94**, 035002 (2022).

[49] H. Legall, G. Blobel, H. Stiel, W. Sandner, C. Seim, P. Takman, D. H. Martz, M. Selin, U. Vogt, H. M. Hertz, D. Esser, H. Sipma, J. Luttmann, M. Höfer, H. D. Hoffmann, S. Yulin, T. Feigl, S. Rehbein, P. Guttmann, G. Schneider, U. Wiesemann, M. Wirtz, and W. Diete, Compact x-ray microscope for the water window based on a high brightness laser plasma source, Opt. Express **20**, 18362–18369 (2012).

[50] K. Fahy, V. Weinhardt, M. Vihinen-Ranta, N. Fletcher, D. Skoko, E. Pereiro, P. Gastaminza, R. Bartenschlager, D. Scholz, A. Ekman, and T. McEnroe, Compact cell imaging device (CoCID) provides insights into the cellular origins of viral infections, J. Phys. Photonics **3**, 031002 (2021).

[51] A. Zylstra, O. Hurricane, D. Callahan, A. Kritcher, J. Ralph, H. Robey, J. Ross, C. Young, K. Baker, D. Casey, T. Döppner, L. Divol, M. Hohenberger, S. Pape, A. Pak, P. Patel, R. Tommasini, S. J. Ali, P. Amendt, and G. Zimmerman, Burning plasma achieved in inertial fusion, Nature **601**, 542–548 (2022).

[52] S. K. Moore, EUV lithography finally ready for fabs, IEEE Spectrum **55**, 46–48 (2018).

II

[53] O. O. Versolato, Physics of laser-driven tin plasma sources of EUV radiation for nanolithography, Plasma Sources Sci. Tech. **28**, 083001 (2019).

[54] K. Tomita, Y. Sato, S. Tsukiyama, T. Eguchi, K. Uchino, K. Kouge, H. Tomuro, T. Yanagida, Y. Wada, M. Kunushima, G. Soumagne, T. Kodama, H. Mizoguchi, A. Sunahara, and K. Nishihara, Time-resolved two-dimensional profiles of electron density and temperature of laser-produced tin plasmas for extreme-ultraviolet lithography light sources, Sci. Rep. **7**, 12328 (2017).

[55] F. Torretti, F. Liu, M. Bayraktar, J. Scheers, Z. Bouza, W. Ubachs, R. Hoekstra, and O. Versolato, Spectral characterization of an industrial EUV light source for nanolithography, J. Phys. D Appl. Phys. **53**, 055204 (2019).

[56] J. Sheil, O. Versolato, V. Bakshi, and H. Scott, Review of the 1st EUV light sources code comparison workshop, Atoms **11**, 130 (2023).

[57] W. Svendsen and G. O'Sullivan, Statistics and characteristics of xuv transition arrays from laser-produced plasmas of the elements tin through iodine, Phys. Rev. A **50**, 3710–3718 (1994).

[58] A. Sasaki, A. Sunahara, H. Furukawa, K. Nishihara, S. Fujioka, T. Nishikawa, F. Koike, H. Ohashi, and H. Tanuma, Modeling of radiative properties of Sn plasmas for extreme-ultraviolet source, J. Appl. Phys. **107**, 113303 (2010).

[59] G. O'Sullivan, B. Li, R. D'Arcy, P. Dunne, P. Hayden, D. Kilbane, T. McCormack, H. Ohashi, F. O'Reilly, P. Sheridan, E. Sokell, C. Suzuki, and T. Higashiguchi, Spectroscopy of highly charged ions and its relevance to EUV and soft x-ray source development, J. Phys. B: At. Mol. Opt. Phys. **48**, 144025 (2015).

[60] K. Nishihara, A. Sunahara, A. Sasaki, M. Nunami, H. Tanuma, S. Fujioka, Y. Shimada, K. Fujima, H. Furukawa, T. Kato, F. Koike, R. More, M. Murakami, T. Nishikawa, V. Zhakhovskii, K. Gamata, A. Takata, H. Ueda, H. Nishimura, Y. Izawa, N. Miyanaga, and K. Mima, Plasma physics and radiation hydrodynamics in developing an extreme ultraviolet light source for lithography, Phys. Plasmas **15**, 056708 (2008).

[61] I. Fomenkov, D. Brandt, A. Ershov, A. Schafgans, Y. Tao, G. Vaschenko, S. Rokitski, M. Kats, M. Vargas, M. Purvis, R. Rafac, B. La Fontaine, S. De Dea, A. LaForge, J. Stewart, S. Chang, M. Graham, D. Riggs, T. Taylor, M. Abraham, and D. Brown, Light sources for high-volume manufacturing EUV lithography: technology, performance, and power scaling, Adv. Opt. Techn. **6**, 173–186 (2017).

[62] R. A. M. M. B. J. S. D. K. A. B. K. S. E. E. S. W. W. U. R. H. R. Schupp, F. Torretti and O. O. Versolato, Efficient generation of extreme ultraviolet light from Nd:YAG-driven microdroplet-tin plasma, Phys. Rev. Appl. **12**, 014010 (2019).

[63] K. Umstadter, M. Graham, M. Purvis, A. Schafgans, J. Stewart, P. Mayer, and D. Brown, EUV light source for high-NA and low-NA lithography, in *Optical and EUV Nanolithography XXXVI*, Vol. 12494, edited by A. Lio, International Society for Optics and Photonics (SPIE, 2023) p. 124940Z.

[64] C. W. Siders, A. J. Bayramian, A. C. Erlandson, T. C. Galvin, S. Langer, E. F. Sistrunk, and T. M. Spinka, New architectures for PW-scale high peak power lasers scalable to near-MW average powers and their application to EUV generation, in *Source Workshop*, S22 (EUV Litho Inc., 2018).

[65] S. Langer, C. Siders, T. Galvin, H. Scott, and E. Sistrunk, Simulations of EUV sources driven by CO_2 and thulium lasers, in *Source Workshop*, S94 (EUV Litho Inc., 2019).

[66] I. Tamer, B. A. Reagan, T. Galvin, F. Batysta, E. Sistrunk, D. Willard, A. Church, H. Neurath, J. Galbraith, G. Huete, and T. Spinka, 1 GW peak power and 100 J pulsed operation of a diode-pumped Tm:YLF laser, Opt. Express **30**, 46336–46343 (2022).

[67] L. Behnke, R. Schupp, Z. Bouza, M. Bayraktar, Z. Mazzotta, R. Meijer, J. Sheil, S. Witte, W. Ubachs, R. Hoekstra, and O. O. Versolato, Extreme ultraviolet light from a tin plasma driven by a 2-µm-wavelength laser, Opt. Express **29**, 4475–4487 (2021).

[68] R. Schupp, L. Behnke, J. Sheil, Z. Bouza, M. Bayraktar, W. Ubachs, R. Hoekstra, and O. O. Versolato, Characterization of 1- and 2-µm-wavelength laser-produced microdroplet-tin plasma for generating extreme-ultraviolet light, Phys. Rev. Research **3**, 013294 (2021).

[69] R. Schupp, L. Behnke, Z. Bouza, Z. Mazzotta, Y. Mostafa, A. Lassise, L. Poirier, J. Sheil, M. Bayraktar, W. Ubachs, R. Hoekstra, and O. O. Versolato, Characterization of angularly

resolved EUV emission from 2-µm-wavelength laser-driven Sn plasmas using preformed liquid disk targets, J. Phys. D: Appl. Phys. **54**, 365103 (2021).

[70] Y. Mostafa, L. Behnke, D. J. Engels, Z. Bouza, J. Sheil, W. Ubachs, and O. O. Versolato, Production of 13.5 nm light with 5% conversion efficiency from 2 µm laser-driven tin microdroplet plasma, Appl. Phys. Lett. **123**, 234101 (2023).

[71] L. Behnke, E. J. Salumbides, G. Göritz, Y. Mostafa, D. Engels, W. Ubachs, and O. Versolato, High-energy parametric oscillator and amplifier pulsed light source at 2-µm, Opt. Express **31**, 24142–24156 (2023).

[72] D. J. Hemminga, O. O. Versolato, and J. Sheil, Simulations of plasmas driven by laser wavelengths in the 1.064-–10.6 µm range for their characterization as future extreme ultraviolet light sources, Phys. Plasmas **30**, 033301 (2023).

[73] T. Sizyuk and A. Hassanein, Tuning laser wavelength and pulse duration to improve the conversion efficiency and performance of EUV sources for nanolithography, Phys. Plasmas **27**, 103507 (2020).

[74] Y. Yuan, Y. Y. Ma, W. P. Wang, S. J. Chen, Y. Cui, M. Zi, X. H. Yang, G. B. Zhang, and Y. X. Leng, Enhancing the conversion efficiency of extreme ultraviolet light sources using a 2 µm wavelength laser, Plasma Phys. Control. Fusion **64**, 025001 (2021).

[75] Z. Y. Shi, Y. Yuan, W. P. Wang, Y. Y. Ma, X. Y. Sun, N. Lin, and Y. X. Leng, Enhanced extreme ultraviolet conversion efficiency of a 2 µm laser-driven preformed tin-droplet target using short picosecond pre-pulses, Phys. Plasmas **30**, 043107 (2023).

[76] M. Basko, J. Maruhn, and A. Tauschwitz, Development of a 2D radiation-hydrodynamics code RALEF for laser plasma simulations, GSI report **1**, 410 (2010).

[77] M. M. Basko, P. V. Sasorov, M. Murakami, V. G. Novikov, and A. S. Grushin, One-dimensional study of the radiation-dominated implosion of a cylindrical tungsten plasma column, Plasma Phys. Control. Fusion **54**, 055003 (2012).

[78] A. Tauschwitz, M. Basko, A. Frank, V. Novikov, A. Grushin, A. Blazevic, M. Roth, and J. Maruhn, 2D radiation-hydrodynamics modeling of laser-plasma targets for ion stopping measurements, High Energy Density Phys. **9**, 158–166 (2013).

[79] S. Malko, W. Cayzac, V. Ospina-Bohórquez, K. Bhutwala, M. Bailly-Grandvaux, C. McGuffey, R. Fedosejevs, X. Vaisseau, A. Tauschwitz, J. I. Apiñaniz, D. De Luis Blanco, G. Gatti, M. Huault, J. A. Perez Hernandez, S. X. Hu, A. J. White, L. A. Collins, K. Nichols, P. Neumayer, G. Faussurier, J. Vorberger, G. Prestopino, C. Verona, J. J. Santos, D. Batani, F. N. Beg, L. Roso, and L. Volpe, Proton stopping measurements at low velocity in warm dense carbon, Nat. Commun. **13**, 2893 (2022).

[80] D. Kurilovich, M. M. Basko, D. A. Kim, F. Torretti, R. Schupp, J. C. Visschers, J. Scheers, R. Hoekstra, W. Ubachs, and O. O. Versolato, Power-law scaling of plasma pressure on laser-ablated tin microdroplets, Phys. Plasmas **25**, 012709 (2018).

[81] E. Livne and A. Glasner, A finite difference scheme for the heat conduction equation, J. Comp. Phys. **58**, 59–66 (1985).

II

[82] M. M. Basko, J. Maruhn, and A. Tauschwitz, An efficient cell-centered diffusion scheme for quadrilateral grids, J. Comp. Phys. **228**, 2175–2193 (2009).

[83] A. Dedner and P. Vollmöller, An adaptive higher order method for solving the radiation transport equation on unstructured grids, J. Comput. Phys. **178**, 263–289 (2002).

[84] A. F. Nikiforov, V. G. Novikov, and V. B. Uvarov, *Quantum-Statistical Models of Hot Dense Matter: Methods for Computation Opacity and Equation of State (Progress in Mathematical Physics)* (Birkhauser, 2005).

[85] H. A. Scott, J. A. Harte, M. E. Foord, and D. T. Woods, Using tabulated NLTE data for hohlraum simulations, Phys. Plasmas **29**, 082703 (2022).

[86] J. I. Castor, *Radiation hydrodynamics* (Cambridge University Press, 2007).

[87] J. Hernandez-Rueda, B. Liu, D. J. Hemminga, Y. Mostafa, R. A. Meijer, D. Kurilovich, M. Basko, H. Gelderblom, J. Sheil, and O. O. Versolato, Early-time hydrodynamic response of a tin droplet driven by laser-produced plasma, Phys. Rev. Research **4**, 013142 (2022).

[88] M. M. Basko and I. P. Tsygvintsev, A hybrid model of laser energy deposition for multidimensional simulations of plasmas and metals, Comp. Phys. Comm. **214**, 59–70 (2017).

[89] L. Poirier, D. J. Hemminga, A. Lassise, L. Assink, R. Hoekstra, J. Sheil, and O. O. Versolato, Strongly anisotropic ion emission in the expansion of Nd:YAG-laser-produced plasma, Phys. Plasmas **29**, 123102 (2022).

[90] D. D. Hickstein, S. T. Gibson, R. Yurchak, D. D. Das, and M. Ryazanov, A direct comparison of high-speed methods for the numerical Abel transform, Rev. Sci. Instrum. **90**, 065115 (2019).

[91] S. Fujioka, A. Sunahara, K. Nishihara, N. Ohnishi, T. Johzaki, H. Shiraga, K. Shigemori, M. Nakai, T. Ikegawa, M. Murakami, K. Nagai, T. Norimatsu, H. Azechi, and T. Yamanaka, Suppression of the Rayleigh–Taylor instability due to self-radiation in a multiablation target, Phys. Rev. Lett. **92**, 195001 (2004).

[92] R. A. Burdt, S. Yuspeh, K. L. Sequoia, Y. Tao, M. S. Tillack, and F. Najmabadi, Experimental scaling law for mass ablation rate from a Sn plasma generated by a 1064 nm laser, J. Appl. Phys. **106**, 033310 (2009).

[93] F. Dahmani and T. Kerdja, Planar laser-driven ablation model for nonlocalized absorption, Phys. Fluids B **3**, 1232–1240 (1991).

[94] S. J. J. de Lange, D. J. Hemminga, Y. Mostafa, R. A. Meijer, O. O. Versolato, and J. Sheil, Modeling the hundreds-of-nanoseconds-long irradiation of tin droplets with a 2 µm-wavelength laser for future EUV lithography, Plasma Sources Sci. Technol. **33**, 105003 (2024).

[95] C. Li, J. Song, D. Shen, Y. Cao, N. S. Kim, and K. Ueda, Flash-lamp-pumped acousto-optic Q-switched Cr-Tm:YAG laser, Opt. Rev. **7**, 58 (2000).

[96] M. Brandstätter, N. Gambino, and R. S. Abhari, Temporally and spatially resolved ion dynamics of droplet-based laser-produced tin plasmas in lateral expansion direction, J. Appl. Phys. **123**, 043308 (2018).

[97] D. Nakamura, K. Tamaru, Y. Hashimoto, T. Okada, H. Tanaka, and A. Takahashi, Mitigation of fast ions generated from laser-produced Sn plasma for extreme ultraviolet light source by H_2 gas, J. Appl. Phys. **102**, 123310 (2007).

[98] D. Bleiner and T. Lippert, Stopping power of a buffer gas for laser plasma debris mitigation, J. Appl. Phys. **106**, 123301 (2009).

[99] S. S. Harilal, B. O'Shay, and M. S. Tillack, Debris mitigation in a laser-produced tin plume using a magnetic field, J. Appl. Phys. **98**, 036102 (2005).

[100] L. Poirier, A. Lassise, R. Hoekstra, J. Sheil, and O. O. Versolato, Dependence of ion charge-energy emission from Nd:YAG-laser-produced plasma on laser intensity in the $0.4–40\times10^{10}$ W/cm^2 range, Phys. Plasmas **30**, 083505 (2023).

[101] M. Murakami and M. Basko, Self-similar expansion of finite-size non-quasi-neutral plasmas into vacuum: Relation to the problem of ion acceleration, Phys. Plasmas **13**, 012105 (2006).

[102] H. Kawasaki, A. Sunahara, Y. Shimada, T. Ejima, W. Jiang, G. O'Sullivan, M. Nishikino, S. Namba, and T. Higashiguchi, Electron temperature and soft x-ray intensity scaling in laser heavy element plasma interaction, AIP Adv. **10**, 065306 (2020).

[103] I. C. E. Turcu and J. B. Dance, *X-Rays from Laser Plasmas, Generation and Applications* (Wiley, 1999).

[104] G. Karniadakis, A. Beskok, and N. Aluru, *Microflows and Nanoflows: Fundamentals and Simulation* (Springer, 2005).

[105] L. Pitaevskii and E. Lifshitz, *Physical Kinetics*, 10th ed. (Elsevier Science, 2012).

[106] M. Sherlock, P. Michel, D. J. Strozzi, L. Divol, E. Kur, and G. Zimmerman, Inverse bremsstrahlung absorption rate for super-Gaussian electron distribution functions including plasma screening, Phys. Rev. E **109**, 055201 (2024).

II

[107] B. Brewster, S. J. J. de Lange, and J. Sheil, Super-Gaussian integration for the Langdon effect, Submitted for publication.

[108] J. P. Matte, M. Lamoureux, C. Moller, R. Y. Yin, J. Delettrez, J. Virmont, and T. W. Johnston, Non-Maxwellian electron distributions and continuum x-ray emission in inverse bremsstrahlung heated plasmas, Plasma Phys. Control. Fusion **30**, 1665 (1988).

[109] D. Turnbull, A. Colaïtis, A. M. Hansen, A. L. Milder, J. P. Palastro, J. Katz, C. Dorrer, B. E. Kruschwitz, D. J. Strozzi, and D. H. Froula, Impact of the Langdon effect on crossed-beam energy transfer, Nat. Phys. **16**, 181 (2020).

[110] A. L. Milder, H. P. Le, M. Sherlock, P. Franke, J. Katz, S. T. Ivancic, J. L. Shaw, J. P. Palastro, A. M. Hansen, I. A. Begishev, W. Rozmus, and D. H. Froula, Evolution of the electron distribution function in the presence of inverse bremsstrahlung heating and collisional ionization, Phys. Rev. Lett. **124**, 025001 (2020).

[111] A. L. Milder, J. Katz, R. Boni, J. P. Palastro, M. Sherlock, W. Rozmus, and D. H. Froula, Measurements of non-Maxwellian electron distribution functions and their effect on laser heating, Phys. Rev. Lett. **127**, 015001 (2021).

[112] A. L. Milder, J. Katz, R. Boni, J. P. Palastro, M. Sherlock, W. Rozmus, and D. H. Froula, Statistical analysis of non-Maxwellian electron distribution functions measured with angularly resolved Thomson scattering, Phys. Plasmas **28**, 082102 (2021).

[113] M. Lamoureux, C. Möller, and P. Jaeglé, Bremsstrahlung and radiative-recombination emissivity coefficients in non-Maxwellian plasmas, Phys. Rev. A **30**, 429–434 (1984).

[114] P. Alaterre, J.-P. Matte, and M. Lamoureux, Ionization and recombination rates in non-Maxwellian plasmas, Phys. Rev. A **34**, 1578–1581 (1986).

[115] D. Salzmann and Y. T. Lee, An overview of the effects of non-Maxwellian velocity distributions in laser produced plasmas, Journal of Quantitative Spectroscopy and Radiative Transfer **54**, 339–344 (1995).

[116] H. P. Le, M. Sherlock, and H. A. Scott, Influence of atomic kinetics on inverse bremsstrahlung heating and nonlocal thermal transport, Phys. Rev. E **100**, 013202 (2019).

[117] H. P. Le, E. V. Marley, and H. A. Scott, Impact of super-Gaussian electron distributions on plasma K-shell emission, Phys. Rev. E **112**, 025202 (2025).

[118] C. Blancard, P. Cossé, and G. Faussurier, Effects of super-Gaussian electron velocity distribution functions on atomic kinetics and radiative emission of hot under-dense gold plasmas, Phys. Plasmas **32**, 062704 (2025).

[119] P. Mora and H. Yahi, Thermal heat-flux reduction in laser-produced plasmas, Phys. Rev. A **26**, 2259–2261 (1982).

[120] N. R. Shaffer, T. Seo, S. X. Hu, and V. N. Goncharov, The Langdon effect in laser plasmas: Absorption and conduction, Phys. Plasmas **32**, 062703 (2025).

[121] D. Turnbull, J. Katz, M. Sherlock, L. Divol, N. R. Shaffer, D. J. Strozzi, A. Colaïtis, D. H. Edgell, R. K. Follett, K. R. McMillen, P. Michel, A. L. Milder, and D. H. Froula, Inverse bremsstrahlung absorption, Phys. Rev. Lett. **130**, 145103 (2023).

[122] D. Turnbull, J. Katz, M. Sherlock, A. L. Milder, M. S. Cho, L. Divol, N. R. Shaffer, D. J. Strozzi, P. Michel, and D. H. Froula, Reconciling calculations and measurements of inverse bremsstrahlung absorption, Phys. Plasmas **31**, 063304 (2024).

[123] D. Turnbull, R. K. Follett, M. Sherlock, D. J. Strozzi, J. Katz, D. Cao, N. R. Shaffer, K. Aytekin, D. H. Edgell, L. Stanton, and D. H. Froula, Influence of plasma screening on high-density inverse bremsstrahlung absorption, Phys. Rev. E **111**, 065206 (2025).

[124] J. Gonzalez and J. Sheil, Langdon effect in the realm of extreme ultraviolet source plasmas, Phys. Rev. E **111**, L023201 (2025).

[125] D. Kilbane and G. O'Sullivan, Ground-state configurations and unresolved transition arrays in extreme ultraviolet spectra of lanthanide ions, Phys. Rev. A **82**, 062504 (2010).

[126] B. Li, P. Dunne, T. Higashiguchi, T. Otsuka, N. Yugami, W. Jiang, A. Endo, and G. O'Sullivan, Gd plasma source modeling at 6.7 nm for future lithography, Appl. Phys. Lett. **99**, 231502 (2011).

[127] D. O. Gericke, M. S. Murillo, and M. Schlanges, Dense plasma temperature equilibration in the binary collision approximation, Phys. Rev. E **65**, 036418 (2002).

[128] G. Bekefi, *Radiation Processes in Plasmas*, 1st ed. (Wiley, 1966).

[129] W. Shang, J. Yang, W. Zhang, Z. Li, B. Deng, Y. Dong, T. Zhu, C. Huang, X. Zhan, Y. Mei, L. Guo, R. Yu, S. Li, S. Jiang, S. Liu, F. Wang, Y. Ding, B. Zhang, and R. Betti, Experimental demonstration of laser to x-ray conversion enhancements with low density gold targets, Appl. Phys. Lett. **108**, 064102 (2016).

[130] M. M. Marinak, G. B. Zimmerman, T. Chapman, G. D. Kerbel, M. V. Patel, J. M. Koning, S. M. Sepke, B. Chang, C. R. Schroeder, J. A. Harte, D. S. BAiley, L. A. Taylor, S. H. Lnager, M. A. Belyaev, D. S. Clark, J. Gaffney, B. A. Hammel, D. E. Hinkel, A. L. Kritcher, J. L. Milovich, H. F. Robey, and C. R. Weber, How numerical simulations helped to achieve breakeven on the NIF, Phys. Plasmas **31**, 070501 (2024).

[131] R. Abu-Shawareb, Acree, P. Adams, B. Addis, R. Aden, P. Adrian, B. B. Afeyan, M. Aggleton, *et al.*, Achievement of target gain larger than unity in an inertial fusion experiment, Phys. Rev. Lett. **132**, 065102 (2024).

[132] D. J. Strozzi, D. S. Bailey, P. Michel, L. Divol, S. M. Sepke, G. D. Kerbel, C. A. Thomas, J. E. Ralph, J. D. Moody, and M. B. Schneider, Interplay of laser-plasma interactions and inertial fusion hydrodynamics, Phys. Rev. Lett. **118**, 025002 (2017).

[133] H. Scott, S. Langer, and Y. Frank, Radiation-hydrodynamics modeling of LPP EUV sources, in *Photon Sources for Lithography and Metrology*, edited by V. Bakshi (SPIE Press, Washington, 2023) pp. 71–110.

[134] O. O. Versolato, J. Sheil, S. Witte, W. Ubachs, and R. Hoekstra, Microdroplet-tin plasma sources of EUV radiation driven by solid-state-lasers (topical review), J. Opt. **24**, 054014 (2022).

[135] T. Soramoto, A. Ogiwara, H. Morita, W. Jiang, K. Sakaue, T. Ejima, G. O'Sullivan, S. Namba, and T. Higashiguchi, Laser-produced plasma water-window x-ray source by continuous liquid bismuth jet, Opt. Lett. **49**, 5791–5794 (2024).

[136] H. Chen, D. T. Woods, W. A. Farmer, N. A. Aybar, D. A. Liedahl, S. A. MacLaren, M. B. Schneider, H. A. Scott, D. E. Hinkel, O. L. Landen, J. D. Moody, M. D. Rosen, J. S. Ross, S. Rogers, N. Roskopf, G. F. Swadling, and S. Vonhof, Understanding the deficiency in inertial confinement fusion hohlraum x-ray flux predictions using experiments at the National Ignition Facility, Phys. Rev. E **110**, L013201 (2024).

[137] H. Chen *et al.*, Key advancements toward eliminating the "drive deficit" in ICF hohlraum simulations, Phys. Plasmas **32**, 042704 (2025).

[138] E. T. Whittaker and G. N. Watson, *A Course of Modern Analysis*, 4th ed. (Cambridge University Press, Cambridge, 1996).

[139] M. R. Spiegel, *Mathematical Handbook of Formulas and Tables* (McGraw-Hill, New York, 1968) section 16.8: relationships among gamma functions.

[140] P. J. Davis, Leonhard Euler's integral: A historical profile of the gamma function, The American Mathematical Monthly **66**, 849–869 (1959).

II

[141] H.-K. Chung, M. Chen, W. Morgan, Y. Ralchenko, and R. Lee, FLYCHK: Generalized population kinetics and spectral model for rapid spectroscopic analysis for all elements, High Energy Dens. Phys. **1**, 3–12 (2005).

[142] H. Bateman and A. Erdélyi, *Higher Transcendental Functions*, Vol. 1 (McGraw-Hill, New York, 1953) see Section 5.3, "Definition of the G-Function", p. 206.

[143] R. A. Askey and R. Roy, Gamma function, in *NIST Handbook of Mathematical Functions*, edited by F. W. J. Olver, D. M. Lozier, R. F. Boisvert, and C. W. Clark (Cambridge University Press, Cambridge, 2010) pp. 135–147, see the section on series expansions.

[144] H. L. França, H. K. Schubert, O. Versolato, and M. Jalaal, Laser-induced droplet deformation: curvature inversion explained from instantaneous pressure impulse, J. Fluid Mech. **1020**, A21 (2025).

[145] J.-C. Pain and D. Benredjem, Simple electron-impact excitation cross-sections including plasma density effects, High Energy Density Phys. **38**, 100923 (2021)

II

Acknowledgments

I have now reached the end. Not just the end of this thesis, the culmination of four years of research, but also the end of my time as a student of physics. The irreversible arrow of time has flown by too fast.

Let me start at the beginning, with the two lads whom I have known since middle school, **Karel** and **Bart**. We joined the UvA physics bachelor together, attending the lectures and solving problems as a group. When I think back on it, we were messing around far too much, but that did not stop us from getting the work done. It was a strange but mostly carefree time, and I'm glad I experienced it with you. Though we briefly parted for the master, once I moved to Amsterdam for my PhD, we regularly saw each other for fitness sessions and the occasional movie night. Please excuse all my distracting, semi-incoherent ramblings on physics, history, and whatever else I happened to have read up on in that particular week. **Jeroen**, **Jonas**, and the aforementioned Karel, through these years we participated in the annual Top 2000 Quiz, the "training" for which I was putting more effort into than is normal. I hope we'll be able to keep up this tradition well into the future.

During the bachelor and into the master, I also became friends with **Ferran**, **Djel**, **Jasper**, **Hoang**, and **Jelle**, and we formed a study group (in a very loose sense of the word) called *The Grand Canonical Ensemble*. Within the first weeks we found out that the master was significantly more challenging than the bachelor, and it wasn't uncommon that we were arguing into the evening about homework exercises, spurred on by a single remaining molecule of dopamine. At difficult times like those, I may well have given up prematurely, but you kept me going, and in the end we managed to pull through together. I'm happy that we still regularly chat, and that from time to time we come together for drinks, laughing at the terror that was Advanced Quantum Field Theory.

Friends I should not neglect to mention: **Michael**, **Jochem**, **Niels**, and **Helena**. I've known you all for so long. Even if we don't see each other for a while, when we're together it's as if no time has passed.

Now for all the people whom I've met at ARCNL. **Oscar**, it is thanks to you that I found my place at ARCNL. You are a calm and gentle leader, and that was something I could deeply appreciate as I came out of the struggles of my master project and the pandemic. The other senior department members, **Wim Ubachs** and **Ronnie**, were also always easy to chat with. In my time at ARCNL there have been three directors, starting with **Joost Frenken** and ending with **Marcelo Ackermann**, but I knew **Wim van der Zande** best. Wim, you are guaranteed to be optimistic and down-to-earth, and running ideas by you was useful and interesting. Thank you for lending me your book on history of atomic theory. Also thanks

to **Marjan** for having time for discussions about the institute and the like.

Diko, you were my closest colleague in the early months. Tinkering with `RALEF` meshes was solitary (and often frustrating) work, but I could count on you to help me out. It was an honour being one of your paranymphs. **Jorge**, as the first postdoc of the group, you helped me understand some tricky theory. Nevertheless, while I tried so hard and got so far, it doesn't even matter. **Surabhi**, you made our office a lot more lively. I really enjoyed the Indian sweets you brought from time to time. **Randy**, you are an exemplary physicist to me, if for no other reason than that you once gave a presentation called *What Randy Knows*. No joke, being able to phrase what you are confident in, and what is still unclear, is a vital skill. **Mikheil**, soft-spoken but hard-working, I'm glad you were open to conversation, usually when everyone else was having lunch, or on Friday into the evening. Good luck with your sci-fi writing. **Lucas**, I hope I didn't annoy you too much with my poor attempts at speaking French; unfortunately I won't be studying in Paris, but I will go there some other time. **Hermann Karl**, we've made a lot of jokes together, so when you finished, and I became the most senior PhD student, I was sad to see you go. Being one of your paranymphs was a highlight. **Dion**, you started before me as a master student, and somehow you finished your PhD before me. People are rarely as skilled and productive as you are, and I am sure you will go far. **Hugo**, I wish we had talked more. You're a kind, approachable person, and you could still teach me a lot more about fluid dynamics. **Martijn**, same goes for you, I would have liked to have had more time to learn about atomic physics from you. **Bas**, I did not expect to find another fan of Streetlight Manifesto anywhere, let alone at ARCNL. Your dedication to playing music, dancing, and learning languages is inspiring. **Mats**, I don't think I've ever seen you without a smile on your face. Enjoy your beer, and maybe one day you'll add cigars to the mix. **Ryan**, with whom I've had a rare opportunity to talk about one of my oldest obsessions (Pokémon).

Special thanks go out to my paranymphs. **Bowie**, the easy-going socialite who is skilled with the most modern research tools. Despite being stationed in another office, I'm glad we finally got to work together on a paper. **Felix**, whenever Theoryland connected to Experimentland, you were there to help me out, to make sure our work was actually real. Thanks to your dry sense of humour, I found you very easy to chat with. And you have a nice shirt.

Kevin, you joined us as an exchange student in 2023. With your technical skill and casual wit you quickly became a welcome part of the group, as well as a reliable gym buddy. The next year I met **Éanna**, **Kirsten**, and others from University College Dublin at the Joint ICTP–IAEA School in Trieste. Finally last year, I visited Dublin myself. Thank you, **David**, for showing me around the city and campus. It was great meeting you all (again), you're an amazing group.

And of course there were many others who, for lack of a more personalized message, definitely deserve a mention: **Adam**, **Zoi**, **Lars**, **Yahia**, **Xyoisan**, **Hugo**, **Someshwar**, **Jerry**, **Laurens**, **Edcel**, **Matthias**, **Esther**, **Dennis**, **Luc**, **Klaas**, **Subam**, **Emiel**, **Lennart**, **Fleur**, **Mart**, and **Thije**. And the folks from the Plasma Theory & Modeling group specifically: **Sander**, **Mardou**, **Zitao**, **Khoi**, **Stéphanie**, **Sameh**, **Jop**, **Koyo**, and **Ylvie**. If I forgot to credit anyone, that is entirely my own mistake.

I'm indebted to **Attila** for making the awesome cover art of this thesis. Your drawings are amazing and I'm lucky you were willing to help out and give my work the finishing touch. My thanks also extend to: **Till**, **Whiskey**, **Clevers**, **Hopple**, **Rasmus**, **apanx**, **Star Berst**,

III

Reponkers, **Pirk**, **Dranon**, **Wolvan**, **Miku**, **Phottos**, **Norlf**, **Snowman**, **Shoob**, **Prince from Wish™**, **Nitram**, **Kere**, **Zaul**, **Novi**, **Prot07ype**, the French, Irish, and British **ponkfriends**, and all the other normal persons who will remain Anonymous. When I signed up for the convention in Ludwigsburg in my first PhD year, I did not know that it would be the start of such an incredible group of friends. You have made the last four years unforgettable, and since the ride never ends, I will see you at the con. /)

Voor mijn familie schakel ik even over naar het Nederlands. Want hoewel ik voor mijn studie naar Amsterdam was verhuisd, kwam ik in het weekend nog geregeld thuis naar Hoogkarspel. **Mam** en **Pap**, bedankt voor alles wat jullie voor mij hebben betekend: de gastvrijheid wanneer ik langskwam, jullie interesse in mijn onderzoek ("hoe moet ik dit nou weer uitleggen?"), en alle andere steun en wijsheid die ik van jullie gekregen heb. Het is niet in enkele zinnen te bevatten hoe dankbaar ik daarvoor ben. **Annika** en **Ferri**, aangezien jullie nu ook uit huis wonen, zie ik jullie een stuk minder. En dat maakt het thuis ook weer stiller. Zusje en broertje, wat zijn jullie allebei goed bezig, en wat ben ik trots op jullie. Ook wil ik mijn lieve oma's nog noemen: **Oma Tiny**, die ons helaas twee jaar terug verlaten heeft, en **Oma Anneke**, bij wie ik graag nog even op bezoek kom.

Lastly, **John**. There is no other physicist like you. Your critical look, tireless diligence, and bold creativity are every part of the making of a scientist that I look up to. You lead a team of PhD students and postdocs, rise through the academic ranks, casually open up new research avenues, and still have time to watch *The Lord of the Rings* and *Oppenheimer* on repeat. You possess the type of controlled craziness that I resonate with, and where Dion speaks of talking to you as the 'John-trap', I'm afraid you've been more often trapped by me instead. Regardless, in working together with you, I have become a much better writer and presenter. I may have also become less disorganized. In all these things, I could not have had a better supervisor.

Hardly a week passed wherein I did not learn some exciting new physics, whether that was some aspect of plasmas directly applicable to my research, a tangentially related theory I delved into more deeply than necessary, or something entirely unrelated that I could not resist looking at until it made sense, which in the end it often did. I even understand spin now.* Regardless of what the future has in store for me, I can always look back upon my time at ARCNL, happy that I have had the opportunity to learn about physics to my heart's content, and that is the best thing I could have asked for in a PhD. So thank you.

III

*Mostly.

Go home, Cynthia.